Motion dynamics of Exchange-Bias capped Janus particles

Influence of the magnetic properties and behavior in a 2D magnetic field landscape

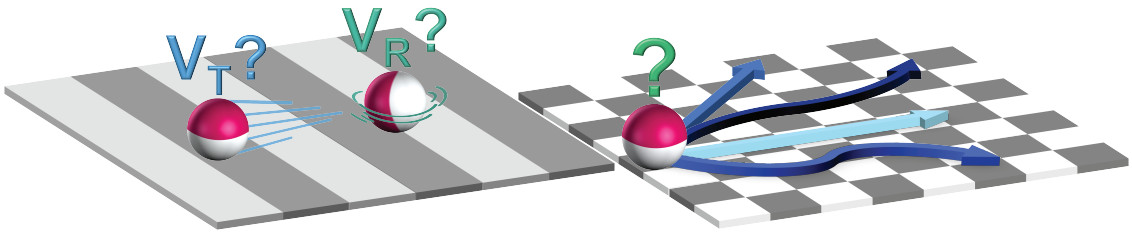

Master Thesis

Presented at the Institute of Physics in the Department of Mathematics and Natural Sciences of the
University of Kassel

Submitted by

B.Sc. Claudia Itzel Jauregui Caballero

First examiner:

Prof. Dr. Arno Ehresmann

Second examiner:

Prof. Dr. Thomas Giesen

Supervised by

Dr. Rico Huhnstock

Dr. Meike Reginka

21st February 2023

Contents

1 Introduction 1

2 Theoretical Background 5

2.1 Magnetic Moment . . . 5
2.2 Magnetic Interactions . . . 6
2.2.1 Spin-Orbit Coupling . . . 7
2.2.2 Dipolar Interaction . . . 8
2.2.3 Exchange Interaction . . . 8
2.3 Magnetic Anisotropies . . . 10
2.3.1 Shape Anisotropy . . . 10
2.3.2 Magnetocrystalline Anisotropy . . . 11
2.3.3 Surface and Interface Anisotropies . . . 11
2.3.4 Unidirectional Anisotropy - Exchange-Bias . . . 12
2.4 Magnetically Capped Particles . . . 16
2.4.1 Ferromagnetic Caps . . . 17
2.4.2 Exchange-Bias Caps . . . 19
2.5 Directed Transport of Magnetic Particles . . . 20
2.5.1 Magnetically Charged Domain Walls . . . 21
2.5.2 Acting Forces . . . 23
2.5.3 Transport Mechanism . . . 27
2.5.4 Janus Particles in Dynamically Transformed Magnetic Field Landscapes . . . 30

3 Experimental Methods 35

3.1 Fabrication of Exchange-Bias Capped Janus Particles . . . 35
3.1.1 Self-Assembly of Template Particles . . . 35
3.1.2 Thin Film Sputter Deposition on Assembled Particles . . . 37

3.2 Kerr Magnetometry . . . 40
3.2.1 Magneto-optic Kerr Effect . . . 40
3.2.2 Kerr Microscopy . . . 43
3.3 Particle Transport Setup . . . 45
3.4 Particle Tracking . . . 49

4 1D Transport: Influence of the Ferromagnetic Layer Thickness 55
4.1 Evaluation Process . . . 57
4.1.1 Transport Step Classification . . . 59
4.1.2 Translational Velocity Determination . . . 63
4.1.3 Rotational Velocity Determination . . . 65
4.2 Influence of t_F on the Motion Patterns of Individual JPs and Agglomerates . . . 68
4.3 Influence of the Magnetic Cap Composition on the Translational and Rotational Velocities . . . 74

5 2D Transport: Correlation of JP Trajectories and Domain Pattern 79
5.1 Substrate Characterization . . . 81
5.1.1 Reference Point Identification . . . 81
5.1.2 Kerr Microscopy Imaging . . . 83
5.1.3 Magnetic Force Microscopy Analysis . . . 87
5.2 Trajectory mapping . . . 89
5.2.1 Image Processing . . . 90
5.2.2 Translational Motion . . . 93
5.2.3 Angular Motion . . . 96
5.2.4 Transition Field Strength . . . 98

6 Summary and Outlook 103

A Appendix 107
A.1 Particle Self-Assembly Parameters . . . 107
A.2 1D Sample Stripe Size Determination . . . 108
A.3 Alternative Approach for the Rotational Step Size Determination 109
A.4 Scaling Factor Determination . . . 111

Bibliography 113

List of Figures

2.1 Modification of EB by Helium ion bombardment. 15
2.2 Phase diagrams of possible magnetic textures within permalloy spherical half shells. 18
2.3 Micromagnetic simulations of magnetization distributions within hardmagnetic hemispherical caps. 20
2.4 Domain walls representation. 22
2.5 Relevant forces acting on a magnetic particle in a microfluidic particle transport system. 24
2.6 Schematic representation of the magnetic particle transport mechanism. 28
2.7 Correlation of EB-JPs lateral position and spatial orientation with respect to $U_{p,z}(x)$ and the corresponding $H_{ex,eff}$. 31

3.1 Depiction of the particle self-assembly procedure. 36
3.2 Schematic representation of the sputter deposition system and the capping layer on top of the particles. 38
3.3 MOKE geometries. 42
3.4 MOKE microscope. 44
3.5 Particle transport experimental setup and microfluidic chamber depiction. 46
3.6 Video image processing. 50
3.7 Particle tracking modes used in the Video Spot Tracker program. 51

4.1 Example of particle transport tracking data. 58
4.2 Particle transport step classification. 60
4.3 Transport step evaluation for translational velocities. 64
4.4 Transport step evaluation for rotational velocities. 66
4.5 Fitting of rotational data. 67

4.6 Microscope snapshots of EB-JP movement for different t_F. 69
4.7 Microscope snapshots of EB-JP agglomerates movement for different t_F. 72
4.8 EB-JPs mean steady-state translational and rotational velocities as a function of their cap thickness t_F. 76

5.1 2D transport substrate reference point identification. 82
5.2 Magnetic domain mapping of the 2D transport substrate via Kerr microscopy. 85
5.3 MFM characterization of 2D transport substrate. 88
5.4 Image processing to determine 2D EB-JP transport trajectories. . . 91
5.5 Qualitative analysis of EB-JP translational motion above 2D pattern. 94
5.6 Qualitative analysis of EB-JPs angular motion above 2D pattern. . 97
5.7 Transition field for the 2D movement of EB-JPs. 99

A.1 Stripe pattern of the 1D transport sample. 108
A.2 Derivative approach for the rotational step size determination. . . 110
A.3 Edge detection and image subtraction of reference point for 2D transport substrate. 112

Terms and Abbreviations

1D	one-dimensional	**IB_1**	first ion bombardment procedure
2D	two-dimensional	**IB_2**	second ion bombardment procedure
AF	antiferromagnet(ic)	**IB_1+IB_2**	double ion bombarded
DW	domain wall	**IBMP**	ion bombardment induced magnetic patterning
EB	Exchange-Bias	**JP**	Janus particle
EB_0	original magnetization direction	**LOC**	Lab-on-a-chip
EB-JP	Exchange-Bias capped Janus particles	**MFL**	magnetic field landscape
F	ferromagnet(ic)	**MFM**	magnetic force microscopy
fps	frames per second	**MOKE**	magneto-optical Kerr effect
H_{eff}	effective magnetic field	**PMMA**	Poly(methylmethacrylate)
hh	head-to-head	t_{F}	ferromagnetic thickness
hs	head-to-side	**ts**	tail-to-side
IB	ion bombardment	**tt**	tail-to-tail

1 Introduction

Over the last decades, micro total analysis systems (μTAS) and Lab-on-a-chip (LOC) devices have been investigated to potentially tackle the rising need for cheap, fast and reliable point-of-care diagnostics [MGW90, Kni02, CLS12, LMS17]. Some of the reasons for the need to develop these systems include the demographic development towards an "older" society, support developing countries with scarce access to sophisticated medical equipment, and early detection of life-threatening diseases [YAL13]. However, these systems have to overcome the challenge of efficiently isolating and detecting disease-marker entities, e.g., viruses and proteins, within a portable LOC device. Nevertheless, a promising solution to address this challenge is the implementation of magnetic particles with appropriate surface receptors within these LOC devices [PCJ03, Gij04, Pam06, MVP19]. To implement this type of particles, several key functionalities need to be addressed: The interaction of the magnetic particles with the analyte (specific binding), isolation from a screened sample and reproducible detection of the analyte binding events. Related research has been focused so far on superparamagnetic particles due to their high flexibility in surface functionalization and magnetic content [HKB15, HANL15, LTK17, RHE21, RLG21, HRS22]. Within these studies, different systems to guide superparamagnetic particles on top of a chip surface within a microfluidic environment were investigated. One simple way to transport magnetic particles is via magnetophoresis, which consists of applying a magnetic field gradient to the system, initiating movement of the exposed magnetic particles [YES07]. Another way to induce particle transport is to combine magnetic field landscapes (MFL) in the micron-range with the application of time-varying homogeneous magnetic fields. This method leads to a more controllable one-dimensional (1D) and two-dimensional (2D) particle transport, which is additionally accompanied with larger motion speeds [TSJ09, ELW11, EKH15, HKB15, KBS20]. Here, a difference can be made between MFL generated by stray fields

emerging from micron-sized magnetic elements on the substrate [TSJ09, KBS20] or by stray fields emerging from domain walls (DWs) in magnetically patterned thin films [ELW11, EKH15, HKB15]. However, in general, it is desired to increase the probability of interaction between the magnetic particle surface and the analyte to improve the applicability of the particles in these systems. This increase in the probability of interaction can be achieved by inducing controlled particle rotations in addition to translational motions. Unfortunately, superparamagnetic particles typically do not exhibit this additional degree of freedom in their motion control due to their characteristic magnetic properties. Nevertheless, there are magnetic particles that can be rotated [HRT21]. These magnetic particles are asymmetrical structured, so-called Janus particles (JPs), which are the subject of the investigations presented in this thesis. Magnetic JPs are typically fabricated by means of a deposition technique on top of an array of template particles, with the preferred method to perform the deposition process being sputter deposition [Ses12], due to its capacity of depositing thin film systems. This JPs fabrication method produces particles with an attached hollow hemispheric cap. Following this fabrication method, magnetic JPs have been produced and investigated for different deposited thin film systems, where not only different materials have been used to create the caps but also different thicknesses, and even post processing methods to alter the magnetic properties of the caps after their creation [AHG05, SKS12, SKR16, TRH21, Reg22]. These studies have established the existence of different magnetization states/textures that can be present in caps according to their size and the magnetic system used to create them. Of the different possible magnetization states, three seem to be the energetically preferred ones: out-of-plane, onion and vortex [SKS12, SKR16]. Additionally, studies on JPs capped with an Exchange-Bias system (EB-JPs), as the particles used in this work, showed that a pinning of an onion texture can be accomplished by introducing a unidirectional anisotropy into the cap by means of Exchange interaction [TRH21]. JPs whose caps exhibit an onion magnetization texture at remanence posses a fixed and larger magnetic moment, which can be then exploited to induce the rotation of JPs. Experiments studying the rotational dynamics of EB-JPs have shown that the rotation of these JPs can be addressed via an externally applied magnetic field [HRT21].

Within this thesis, based on studies of the known 1D transport of EB-JPs over a prototypical parallel stripe domain pattern [HRT21], two open research questions

were intended to be answered:

1. How do the magnetic properties of JP caps influence the motion dynamics, in particular the qualitative behavior and motion speed, of the particles?

   Consequently, considering a systematic study on the influence of the ferromagnetic layer thickness t_F, which so far has not yet been performed for EB caps in the micrometer range: How does the remanent magnetization texture of the cap, which is known to be dependent on t_F, influence the motion dynamics?

   Furthermore, can the magnetic state of the caps be identified by simply observing the motion behavior of the particles in a microfluidic transport experiment?

2. Can EB-JPs be transported above more complex domain patterns, e.g., a checkerboard-like pattern, where the particles are thus induced to perform 2D transport?

   A checkerboard-like pattern has proven to be applicable for superparamagnetic beads to induce their 2D transport [Deu16]. Here, however, no relation between particle position during transport experiment and the position of domains and domain walls in the underlying substrate was established. Another task was therefore the development of a systematic experimental routine for drawing this connection, exemplified for the investigated EB-JPs.

Prior to the discussion of these experiments, the theoretical background and the utilized experimental methods will be introduced.

2 Theoretical Background

To set the experimental results obtained in this thesis into theoretical context, the relevant fundamentals will be presented in the following. Starting from the origin of magnetism (Section 2.1) and the fundamental magnetic interactions (Section 2.2), the focus will shift to the magnetic anisotropies arising from such interactions (Section 2.3). Afterward, the concept of magnetic Janus particles and their transport-relevant properties will be introduced in Section 2.4. Finally, the concept of particle transport and the mechanism used in this project will be presented in Section 2.5, where a description of the origin of the required magnetic stray field landscape, the relevant forces acting on magnetic particles, as well as an introduction into a recent study on the motion dynamics of magnetic Janus particles will be included.

2.1 Magnetic Moment

The magnetic moment $\vec{\mu}$ is the principal quantity that gives rise to the phenomena of magnetism. Although matter is composed at the atomic scale of electrons, protons, and neutrons, its magnetic properties are mainly determined by the magnetic moments of its electrons in partly filled electron shells and their different interactions. This is because the magnitude of the particle magnetic moment is inversely proportional to the particle mass, leading to negligible values three orders of magnitude smaller for $\vec{\mu}$ of protons and neutrons [Coe10, Ste12]. Each of the electrons has an orbital angular momentum $\vec{l}$ related to its motion around the nucleus and a spin angular momentum $\vec{s}$. Then, the total orbital angular momentum $\vec{L}$ and the total spin angular momentum $\vec{S}$ for an atom is conformed by the sum of the $\vec{l}$ and $\vec{s}$ of the individual electrons, respectively [Ste12]. This leads to the magnetic moments of the atom $\vec{\mu}_L$ and $\vec{\mu}_S$ associated with its electrons' orbital and spin angular momenta, respectively. This contributions to the total

magnetic moment of the atom $\vec{\mu}$ can be expressed in terms of the Bohr magneton μ_B as [Ste12, Huh22]:

$$\vec{\mu}_L = -\mu_B \cdot \vec{L}, \tag{2.1}$$

$$\vec{\mu}_S = -2 \cdot \mu_B \cdot \vec{S}, \tag{2.2}$$

where μ_B is defined by the electron charge e, the reduced Planck constant $\hbar$, and the electron mass m_e as

$$\mu_B = \frac{|e| \cdot \hbar}{2 \cdot m_e}. \tag{2.3}$$

The Bohr magneton is derived from the atomic model presented by Niels Bohr in 1913 and represents the magnetic moment of the electron in the first Bohr orbital, i.e., the orbital of lowest energy. This constant is fundamental and is used as a natural unit of the magnetic moment [CG08]. Consequently, $\vec{\mu}$ is obtained from the vector sum of Eq. 2.1 and 2.2 [Ste12, Huh22]

$$\vec{\mu} = -\mu_B \cdot (\vec{L} + 2 \cdot \vec{S}), \tag{2.4}$$

which takes into account the contributions from all electrons. Therefore, if the magnetic moments of the individual electrons are overall oriented in opposite directions, the atom does not have a permanent magnetic moment. If this condition extends to the entire material, it is called diamagnetic. However, if the magnetic moments of the electrons do not entirely cancel each other, the atom has a net magnetic moment. Hence the need for the electron shells to be partially filled. The materials composed of this type of atom are denominated paramagnetic, ferromagnetic, antiferromagnetic, or ferrimagnetic [CG08, Huh22]. The specific classification of the materials into the latter mentioned magnetic categories depend on the interactions of the atomic moments, interactions defined by quantum mechanical laws [Coe10].

2.2 Magnetic Interactions

In the following sections, the main interactions responsible for the macroscopic magnetic properties of materials are summarized. These interactions describe the relationship between the electron's spin and its movement around the nucleus as in the "spin-orbit coupling" (Section 2.2.1) and between the magnetic moments of multiple electrons as in the "dipolar interaction" (Section 2.2.2) and "exchange interaction" (Section 2.2.3).

2.2.1 Spin-Orbit Coupling

In the previous section, it was already mentioned that the magnetic moment $\vec{\mu}$ of an atom consists of the orbital $\vec{l}$ and spin $\vec{s}$ angular momenta of the individual electrons. Moreover, the atom has a total electronic angular momentum $\vec{J}$, which is also determined by $\vec{l}$ and $\vec{s}$ of its electrons. For this, it is necessary to consider how $\vec{l}$ and $\vec{s}$ are combined. This combination is determined by a relativistic interaction known as spin-orbit coupling. This coupling originates, in a simplified classical picture, from the electron's motion around the nucleus, which, when viewed from the electron's perspective, appears as the nucleus rotating around the electron. This "motion of the nucleus" generates a magnetic field

$$\vec{B}_l = \frac{Z \cdot e \cdot \mu_0}{4 \cdot \pi \cdot r^3 \cdot m_e} \cdot \vec{l}, \tag{2.5}$$

located at the electron and aligned parallel to $\vec{l}$ [HWB05]. Here, Z is the nuclear charge, μ_0 is the permeability constant, and r is the distance between the electron and the nucleus. This magnetic field induces a parallel or antiparallel alignment of the $\vec{\mu}$ of the electron and its coupled $\vec{s}$. Since the electron's $\vec{\mu}$ has an opposite direction to the $\vec{s}$, the interaction energy between the spin and the orbital field will depend on the alignment of the spin to $\vec{l}$. Then, the interaction energy from the spin-orbit coupling effect is given by

$$E_{l,s} = -\vec{\mu}_s \cdot \vec{B}_l = \frac{Z \cdot e^2 \cdot \mu_0}{8 \cdot \pi \cdot r^3 \cdot m_e^2} \cdot (\vec{s} \cdot \vec{l}), \tag{2.6}$$

where, for $\vec{s} \uparrow\uparrow \vec{l}$ this energy is highest and lowest for $\vec{s} \uparrow\downarrow \vec{l}$ [TL12, HWB05]. It can be noted from Eq. 2.6 through Z that the spin-orbit interaction is weak for light atoms and becomes more relevant for heavy elements, in particular for the electrons close to the nuclei [Coe10]. Therefore, two limiting cases can be distinguished for the coupling between the $\vec{s}$ and the $\vec{l}$ of the electrons to obtain $\vec{J}$ [HWB05].

In the first case, the *LS* or Russell-Saunders coupling, is used to describe lighter atoms. Here, the spin-orbit interaction $(\vec{s}_i \cdot \vec{l}_i)$ of each individual electron i is weaker than the coupling between different electrons $[(\vec{s}_i \cdot \vec{s}_j)$ or $(\vec{l}_i \cdot \vec{l}_j)]$ [HWB05]. Hence, the total orbital $\vec{L}$ and spin $\vec{S}$ angular momenta are obtained from a vectorial sum before combining to form $\vec{J}$ as:

$$\vec{L} = \sum_i \vec{l}_i, \qquad \vec{S} = \sum_i \vec{s}_i, \qquad \vec{J} = \vec{L} + \vec{S}. \tag{2.7}$$

On the contrary, as mentioned above, the spin-orbit coupling has a stronger effect on the electrons of heavy elements. Whereby, the $\vec{l}_i$ and $\vec{s}_i$ of the electrons first couple to each other to form individual $\vec{j}_i$, before combining to $\vec{J}$; known as jj-coupling [HWB05]:

$$\vec{j}_i = \vec{l}_i + \vec{s}_i, \qquad \vec{J} = \sum_i \vec{j}_i. \tag{2.8}$$

2.2.2 Dipolar Interaction

In a solid material, each individual magnetic dipole with a magnetic moment $\vec{\mu}$ generates a magnetic field perceived by the other dipoles. This induces a magnetostatic interaction between all pairs of magnetic dipoles $\vec{\mu}_i$ and $\vec{\mu}_j$ within the solid, separated by a distance r_{ij}, shown by [Geto8, BSB05]

$$E_{dip} = \frac{\mu_0}{4 \cdot \pi \cdot r_{ij}^3} \cdot \left(\vec{\mu}_i \cdot \vec{\mu}_j - \frac{3 \cdot (\vec{\mu}_i \cdot \vec{r}_{ij}) \cdot (\vec{\mu}_j \cdot \vec{r}_{ij})}{r_{ij}^2} \right). \tag{2.9}$$

Considering two parallel aligned dipoles with $\vec{\mu}_1 = \vec{\mu}_2 = \vec{\mu}_B$ separated by a distance $r_{ij} = 2$ Å, the dipolar interaction energy results in $E_{dip} = 2.1 \times 10^{-24}$ J, for $\vec{\mu} \perp \vec{r}_{12}$ [Geto8]. This energy E_{dip} can be transformed to a temperature T taking $E = k_B \cdot T$, where k_B is the Boltzmann constant, leading to a corresponding temperature below 1 K [Geto8]. Hence, the dipolar interaction cannot set the order of the atomic magnetic moments, which is characteristic for ferromagnetic materials, since temperatures higher than 1 K would imply a disorder of the atomic magnetic moments and a loss of the magnetic properties. However, the dipolar interaction strongly influences shape anisotropy (cf. Section 2.3.1) and magnetic domain formation due to its long-range character [BSB05].

2.2.3 Exchange Interaction

It is still necessary to explain what induces the magnetic ordering of atomic magnetic moments. This fundamental property of magnetic materials originates in the exchange interaction, which considers the electrostatic Coulomb repulsion and the Pauli principle [Coe10]. The latter principle has to be taken into account due to the fermionic character of electrons, which excludes the possibility of electrons sharing a quantum state, described by the same set of quantum numbers [Coe10].

To explain this interaction, a system consisting of only two electrons at positions r_1 and r_2 is first assumed [Geto8]. The total wave function of the two electrons $\psi(\vec{r}_1, \vec{s}_1, \vec{r}_2, \vec{s}_2)$ can be represented by the product of the spatial $\varphi(\vec{r}_1, \vec{r}_2)$ and the spin $\chi(\vec{s}_1, \vec{s}_2)$ wave functions. The Pauli principle also establishes that the total wave function must be antisymmetric, i.e., $\psi(\vec{r}_1, \vec{s}_1, \vec{r}_2, \vec{s}_2) = -\psi(\vec{r}_2, \vec{s}_2, \vec{r}_1, \vec{s}_1)$, to keep the electron density $|\psi(\vec{r}_1, \vec{s}_1, \vec{r}_2, \vec{s}_2)|^2$ unchanged under the exchange of electrons. This antisymmetry condition can then be fulfilled by $\varphi(\vec{r}_1, \vec{r}_2)$ being symmetric and $\chi(\vec{s}_1, \vec{s}_2)$ antisymmetric, or vice versa [Geto8, BSBo5]. For $\chi(\vec{s}_1, \vec{s}_2)$ to be antisymmetric, the spins of the electrons have to be aligned as $\vec{s}_1 \uparrow\downarrow \vec{s}_2$, leading to a total spin $S = 0$ and to a state called singlet. However, if $\chi(\vec{s}_1, \vec{s}_2)$ is symmetric, the spins align parallel to each other as $\vec{s}_1 \uparrow\uparrow \vec{s}_2$ forming a triplet state with $S = 1$. These singlet and triplet states have corresponding energies E_S and E_T, from which the exchange energy can be obtained as $E_{Ex} = E_S - E_T$, representing the energy cost of exchanging electrons from a singlet to a triplet state. Taking this energy E_{Ex} and the Heisenberg model, an effective Hamiltonian that describes the spin interaction in this two-electron system can be written as [Geto8]:

$$\hat{H} = \frac{1}{4} \cdot (E_S + 3 \cdot E_T) - (E_S - E_T) \cdot \vec{s}_1 \cdot \vec{s}_2. \tag{2.10}$$

Ignoring the first term, which is constant, one can reduce the Hamiltonian to the second term, which is the spin configuration-dependent part. Additionally, by defining the exchange constant $J_{Ex} = (E_S - E_T)/2$, it follows [Geto8]

$$\hat{H} = -2 \cdot J_{Ex} \cdot \vec{s}_1 \cdot \vec{s}_2. \tag{2.11}$$

From J_{Ex}, it is possible to deduce how the spins are aligned. If J_{Ex} is positive ($E_S > E_T$), a triplet state is energetically preferred, i.e., ferromagnetic coupling. Whereas, if J_{Ex} is negative ($E_T > E_S$), the spins align as in a singlet state, i.e., antiferromagnetic coupling [Geto8]. Here, two opposing effects take place. The first one is the Coulomb interaction which repeals the electrons, contributing positively to J_{Ex}. The second one is the attractive interaction between the nucleus and the electron, which has a negative contribution. Hence, J_{Ex} depends on the interatomic distance of neighboring atoms and the radius of the partially filled electron shell, represented in the Bethe-Slater curve [BSBo5].

The Hamiltonian can be extended to a many-particle system. However, it is necessary to consider that the exchange interaction is limited to nearest neighbor

spins due to the characteristic short range of this effect. This assumption leads to

$$\hat{H} = -\sum_{ij} J_{ij} \cdot \vec{S}_i \cdot \vec{S}_j, \tag{2.12}$$

with $J_{ij} = J_{\mathrm{Ex}}$ for neighboring spins and $J_{ij} = 0$ otherwise [Geto8].

2.3 Magnetic Anisotropies

Magnetic materials have a fundamental characteristic called magnetic anisotropy. This property arises from the directional dependence of the magnetization $\vec{M}$ of the material, where $\vec{M}$ "prefers" to align along certain directions due to minimization of the system's free energy [BSB05]. These directions are called easy axes and are determined by different properties in the material, such as shape, composition, and crystalline structure. However, $\vec{M}$ can be forced to align along other directions, including the most energetically inconvenient ones, named hard axes. The latter is done by introducing new energy, the anisotropy energy, into the system as, e.g., by subjecting the system to an external magnetic field $\vec{H}$ [BSB05].

2.3.1 Shape Anisotropy

The term shape anisotropy is used to describe the preference of certain magnetization directions within a sample as a result of its shape. The only exception is a spherical geometry for which the energy required to induce a magnetization axis is equal for all directions [Geto8]. This effect originates from the long-range character of the dipolar interaction (cf. Section 2.2.2) and the symmetry breaking at the sample's surface. The symmetry break leads to uncompensated magnetic moments at the surface, i.e., a magnetization discontinuity. These uncompensated moments create surface magnetic charges, which give rise to magnetic stray fields $\vec{H}_{\mathrm{s}}$ outside the sample and a demagnetizing field $\vec{H}_{\mathrm{dem}}$ inside it [BSB05, Geto8]. The stray field has an energy E_{s} connected to it given by [Geto8]

$$E_{\mathrm{s}} = -\frac{1}{2} \int_V \mu_0 \cdot \vec{M} \cdot \vec{H}_{\mathrm{dem}} \mathrm{d}V. \tag{2.13}$$

The direction of the stray field is dictated by the configuration in which the system's free energy is minimized. For thin film systems, Eq. 2.13 results in the

stray field energy density [Geto8]

$$\varepsilon_s = \frac{1}{2} \cdot \mu_0 \cdot M^2 \cdot \cos^2\theta \tag{2.14}$$

where θ represents the angle between the sample's magnetization $\vec{M}$ and the normal $\hat{n}$ to the sample's surface. From Eq. 2.14, it becomes clear that for a thin film, the magnetization is oriented within the sample's plane, in particular at an angle $\theta = 90$ deg from $\hat{n}$ [Geto8, BSBo5].

2.3.2 Magnetocrystalline Anisotropy

Magnetocrystalline anisotropy refers to a preferential orientation of the magnetization of a material along distinct spatial axes determined by its crystal lattice [Geto8]. This anisotropy does not originate in the exchange interaction, since this interaction is not influenced by the spatial orientation of electron spins, but in the spin-orbit interaction that couples the magnetic moments to the crystal lattice [BSBo5]. Since the electronic orbitals are closely related to the crystallographic axes, a rotation of the spins, interacting with each other via the exchange interaction, out of the easy direction leads to a torque on the orbital angular momenta. In the case of elements with partially filled shells and thus, anisotropic electron density distributions, this rotation causes a change in the overlap of the wave functions between neighboring atoms and thereby an energy-dependent rotation of the orbital momenta [BSBo5]. Hence, the energetically most favorable orientation of the magnetic moments, in the absence of an external magnetic field, is determined by the crystal structure of the magnetic material [Geto8]. This is represented by the magnetocrystalline anisotropy energy, which is related to the magnetocrystalline anisotropy constant of the material, and describes the magnetization energy required to rotate the magnetization vector away from the easy axis [HS98].

2.3.3 Surface and Interface Anisotropies

For the previous descriptions of magnetic anisotropies, the interfaces and surfaces of the system were neglected. However, when considering a low-dimensional solid-state system, such as thin films, the contribution of symmetry breaking at the surface/interface compared to the volume must be taken into account, due to

the higher surface-to-volume ratio. This introduces the effective anisotropy constant K_{eff}, consisting of the volume- and surface-dependent anisotropy constants K_{V} and K_{S}, respectively, and the thickness of the thin film d, shown by [Geto8]:

$$K_{\text{eff}} = K_{\text{V}} + 2 \cdot \frac{K_{\text{S}}}{d}. \tag{2.15}$$

Here, the factor 2 is included to consider both interfaces of the thin film system and K_{V} is negative due to the shape anisotropy [Geto8]. As d determines the surface-to-volume ratio, the contribution of K_{S} to K_{eff} scales inversely with d. Therefore, there is a critical thickness d_{C} that dictates which anisotropy (K_{V} or K_{S}) predominates. For $d > d_{\text{C}}$, K_{V} dominates, giving rise to an in-plane magnetization, whereas for $d < d_{\text{C}}$, K_{S} prevails and an out-of-plane magnetization is preferred. An example value for d_{C} is 12 Å for a Cobalt thin film [Geto8].

2.3.4 Unidirectional Anisotropy - Exchange-Bias

Exchange-Bias (EB) is a unidirectional anisotropy that can be induced in thin film systems where a ferromagnetic (F) and an antiferromagnetic (AF) layer share the same interface. This effect, also known as the exchange shift, originates from the exchange interaction of magnetic moments at the F/AF interface, and was first reported by Meiklejohn and Bean in 1956 by investigating the remagnetization of ferromagnetic cobalt particles with an antiferromagnetic cobalt oxide shell [MB56, MB57]. Phenomenologically, this interface effect leads to a horizontal shift of the magnetization curve along the applied external field axis, defined as the Exchange-Bias field H_{EB}, as well as an increase of the coercive field H_{C} in the F layer [MB56, MB57]. This shift originates from the pinning of the ferromagnetic interface moments by the uncompensated AF, which feel an additional torque due to the exchange coupling to antiferromagnetic moments when an external magnetic field is used to remagnetize the system. If the induced H_{EB} is larger than the induced H_{C} and the ferromagnetic magnetization curve, typically referred to as the hysteresis curve, is rectangular in shape, only one macroscopic magnetization state exists for the ferromagnetic layer in remanent magnetization, i.e., in the absence of an external magnetic field. This unique property of EB thin film systems has led to their exploitation for the fabrication of magnetic memories and sensors [NS99]. With the coercive fields H_{C1} and H_{C2} corresponding to the intersection points of the shifted hysteresis curve with the applied magnetic

field axis, the values for H_{EB} and H_C are mathematically expressed by:

$$H_{EB} = \frac{H_{C1} + H_{C2}}{2}, \tag{2.16}$$

$$H_C = \frac{|H_{C1} - H_{C2}|}{2}. \tag{2.17}$$

The EB effect can be initialized, on the one hand, by applying an external magnetic field during the fabrication of the thin film system and, on the other hand, by a field cooling procedure [MB56, MB57, NS99]. For the field cooling procedure, the thin film system is heated to a temperature T above the Néel temperature T_N of the AF, but below the Curie temperature T_C of the F, with $T_N < T_C$. Simultaneously, an external magnetic field is applied, which is strong enough to saturate the F. From $T > T_N$, the AF enters a paramagnetic state, while the F retains its ferromagnetic properties. Subsequently, the system is cooled in the external magnetic field to a temperature $T < T_N$, where a reorientation mediated by the exchange interaction of the AF magnetic moments at the interface to the F moments aligned by the external magnetic field takes place. Thus, the remaining AF moments align with respect to the ones at the interface. Here, in contrast to a uniaxial anisotropy, the F has only one energetically preferred magnetization state along a distinct spatial axis, hence, it results in a unidirectional anisotropy [NS99, Geto8]. This effect can theoretically be described in a simplified picture, considering the F and AF in single-domain states and the uncompensated AF spins as an effective interfacial magnetic moment, aligned along the easy axis of the AF due to a higher magnetic anisotropy in the AF [Mei62]. In this model, the energy per unit area of an EB system $E_{EB,F}$, which describes the magnetization state of F under coherent rotation of the magnetization in F and AF, can be written as [NS99]:

$$\begin{aligned} E_{EB,F} = &-H \cdot M_F \cdot t_F \cdot \cos(\theta - \beta) + K_F \cdot t_F \cdot \sin^2(\beta) \\ &+K_{AF} \cdot t_{AF} \cdot \sin^2(\alpha) - J_{F/AF} \cdot \cos(\beta - \alpha), \end{aligned} \tag{2.18}$$

where H is the applied field, M_F and t_F the saturation magnetization and thickness of the F layer, respectively, t_{AF} the thickness of the AF layer, K_F and K_{AF} the anisotropy constants of F and AF, respectively, and $J_{F/AF}$ the exchange constant for the interaction of the interface magnetic moments. The angles β, α and θ denote the angle between the F magnetization and the F anisotropy axis, the angle between the AF magnetization and the AF anisotropy axis, and the angle between

the applied magnetic field and the F anisotropy axis, respectively [NS99]. Here, the F and AF anisotropy axes are commonly assumed to be collinear to each other. Equation 2.18 accounts for four different effects: The effect of the applied magnetic field in the F layer (first term), the effect of the F anisotropy (second term), the influence of the AF anisotropy (third term), and the influence of the exchange coupling at the interface [NS99]. Here it is further assumed that the coupling at the interface between the F and AF moments is ferromagnetic in character. Furthermore, domain nucleation and domain wall movement are neglected [NS99]. By minimizing the energy with respect to α and β in Eq. 2.18, an expression for H_{EB} can be derived, resulting in [NS99]:

$$H_{\mathrm{EB}} = \frac{J_{\mathrm{F/AF}}}{M_{\mathrm{F}} \cdot t_{\mathrm{F}}}. \tag{2.19}$$

This minimization leads to an important observation, that H_{EB} is inversely proportional to t_{F}, restating the EB as an interface effect. Moreover, $K_{\mathrm{AF}} \cdot t_{\mathrm{AF}} \geqslant J_{\mathrm{F/AF}}$ is required for the observation of a unidirectional anisotropy. However, if $J_{\mathrm{F/AF}} > K_{\mathrm{AF}} \cdot t_{\mathrm{AF}}$, it is energetically preferred for the system to rotate the AF and F moments simultaneously, hence, no H_{EB} should be observed, only an increase in H_{C} [NS99]. Although this simplified model establishes a baseline for determining H_{EB}, it predicts values for H_{EB} that are orders of magnitude larger than the experimental results, due to the strong dependency on the value for $J_{\mathrm{F/AF}}$, which is experimentally difficult to determine [NS99]. Therefore, a manifold of more complex models have been developed since the discovery of this effect, taking into account the structural composition of the system. For more detailed information on polycrystalline models, the reader is encouraged to refer to the work presented by Merkel in [Mer22].

Modification of EB by Helium Ion Bombardment

Another possibility of initializing the EB effect is in the form of local energy input into the material system in the presence of an external magnetic field. This can be achieved in different ways, e.g., with a heated scanning probe microscope tip [APP16], with a laser [KCJ04] or by means of ion bombardment (IB) (cf. Fig.2.1 (a)) [CBF98]. However, IB stands out from other techniques because of its ability to rapidly process larger sample areas and has proven to be suitable to produce micromagnetic domain patterns used for magnetic particle

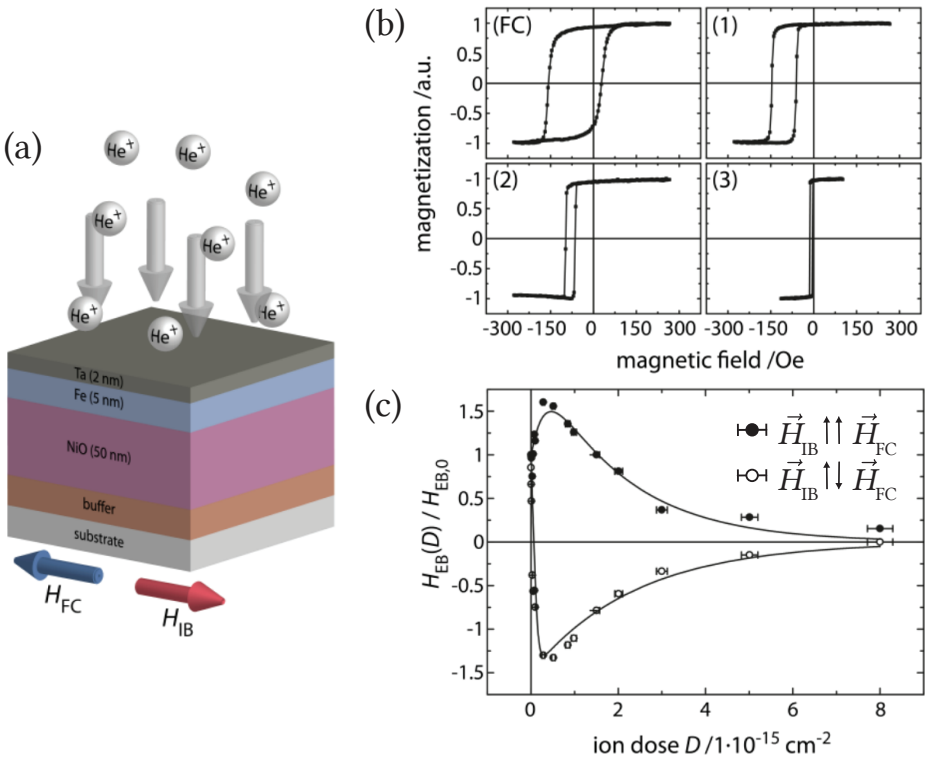

Figure 2.1: Modification of EB by low-energy (10 − 30 keV) Helium ion bombardment. (a) Exemplary EB layer system, where the EB bilayer system (NiO, Fe) is embedded between a buffer and capping layer (Ta). He^+-IB is indicated by gray arrows, blue and red arrows indicate the directions of the fields applied during EB initialization by field cooling (H_{FC}) and of the field applied during ion bombardment (H_{IB}), respectively. (b) Measured hysteresis loop of the EB layer system after field cooling (FC). (1)–(3) Measured loops of the same layer system after IB by 3×10^{14}, 1×10^{15} and 8×10^{15} 10 keV He^+-ions/cm^2, respectively. At an ion dose of around 1×10^{16} ions/cm^2 the loop returns to a loop characteristic for the pure ferromagnetic layer. (c) Typical dependence of the ratio between $H_{EB}(D)$, the EB field after bombardment, and $H_{EB,0}$ (field after layer deposition and field cooling) as a function of the applied ion dose D. Filled circles indicate values when H_{IB} is parallel to H_{FC}, open circles when H_{IB} is antiparallel to H_{FC}. Modified from [EKH15].

transport [ELW11, EKH15, HKB15]. Here, bombardment with light ions, in particular Helium ions, with kinetic energies in the keV range acts like local field cooling, i.e., the EB effect can not only be initialized but also subsequently modified [MLF00, MMJ01, EJE05, EES05]. The energy from the ions is transferred into the layer system through hyperthermal heating and by nuclear impact processes.

An EB layer system may show an increase, decrease or even disappearance of the EB effect as a function of ion dose D (cf. Fig.2.1 (b)). However, the dose range that establishes the effect of IB on the EB system depends on the material as well as its layer thickness. Nevertheless, in general, very high ion doses (number of ions introduced per area) can lead to the suppression of the EB effect, which is attributed to an induced intermixing at the F/AF interface by impinging He ions, effectively destroying the exchange coupling [MLF00, Ehr04]. A typical ion dose dependency for the measured H_{EB} of a bombarded system, normalized to H_{EB} measured for the untreated sample, is shown in Fig.2.1 (c). Additionally, IB can be used to locally set H_{EB} along another direction defined by the applied external magnetic field, e.g., antiparallel to the magnetic field direction applied during an initial field cooling (cf. Fig.2.1 (c)), leading to the possibility of creating different magnetic textures in a sample.

This can be exploited to artificially create magnetic stray field landscapes (MFL) used for particle transport (cf. Section 2.5.1). This technique to create magnetic texturing is defined as ion bombardment induced magnetic pattern (IBMP), and can be used with a focused helium ion beam to directly write magnetic structures on the sample or in combination with a photolithography process performed prior to IB. During the photolithography process a resist structure is created on top of the sample, which can act as a mask for the helium ions in the IB process, preventing them from penetrating the EB layer system underneath. Afterward, the resist mask can be chemically removed, resulting in a magnetically textured but still topographically flat substrate. The magnetic pattern thus created is formed by stable magnetic domains with defined borders, so-called domain walls. This allows to engineer patterns leading to samples with tailored MFLs.

2.4 Magnetically Capped Particles

Janus particles (JPs) are characterized by having two or more distinct physical or chemical properties on their surfaces, resulting in anisotropic characteristics. These types of particles are named after the two-faced Roman god Janus and were first introduced as particles possessing one hydrophobic and one hydrophilic side [CFR89], however, this term is nowadays employed to refer to any type of two-sided particle. Based on this basic concept, magnetic JPs are typically characterized by having a magnetic and a non-magnetic side. These magnetic particles

can be easily fabricated by depositing a thin magnetic film on a self-assembled array of non-magnetic particles [AHG05]. This method results in the formation of a thin hemispherical shell, in this work usually referred to as a cap, covering half of the original template particle. In this thesis, investigations on the transport of magnetic particles, in particularly, Exchange-Bias capped Janus particles (EB-JPs), are presented. Therefore, given the relevance in the context of this work, a brief introduction on recent research on the magnetic properties of purely ferromagnetic and EB hemispherical shells/caps is presented in the following.

2.4.1 Ferromagnetic Caps

JPs' caps can exhibit magnetic properties resembling ferromagnetic behavior, e.g., a permanent magnetic moment, i.e., a non-zero magnetization in remanence. These properties are strongly influenced by the size of the template particle and the material and thickness of the deposited thin film [SKS12, SKR16, Reg22]. For the applications within this work, the permanent magnetic moment of JPs' caps is of paramount importance, as it drives the dynamics of JPs' motion in microfluidic transport experiments. The effective magnetic moment of the cap is determined by the orientation of its atomic moments, resulting in a characteristic magnetic state or magnetization texture. Therefore, the magnetic state of the caps at remanence is the focal interest, as the magnetic fields applied during transport experiments are assumed to be weak enough to not significantly influence the magnetic texture of the JP caps. Investigations have shown that JPs' caps can be tailored to exhibit different magnetic textures [SFK16]. These investigations were initiated by Albrecht et al. who covered hexagonally packed polymeric particles with $[Co/Pd]^n$ multilayers, resulting in JP caps that showed an orientation of magnetic moments perpendicular to the cap surface (out-of-plane state) [AHG05]. During the last decade, Streubel et al. have carried out numerous investigations on magnetism in curved geometries [SFK16], e.g., studies on soft-magnetic JPs, where the equilibrium magnetic states in individual hemispherical NiFe (permalloy) caps were determined [SKS12]. To this end, they experimentally analyzed caps with a film thickness of the permalloy of 20 nm and a diameter ranging from 50 nm to 800 nm by means of x-ray magnetic circular dichroism photoelectron emission microscopy (XMCD-PEEM) in order to visualize the caps' magnetic textures. From this analysis, caps exhibiting curled alignment of mag-

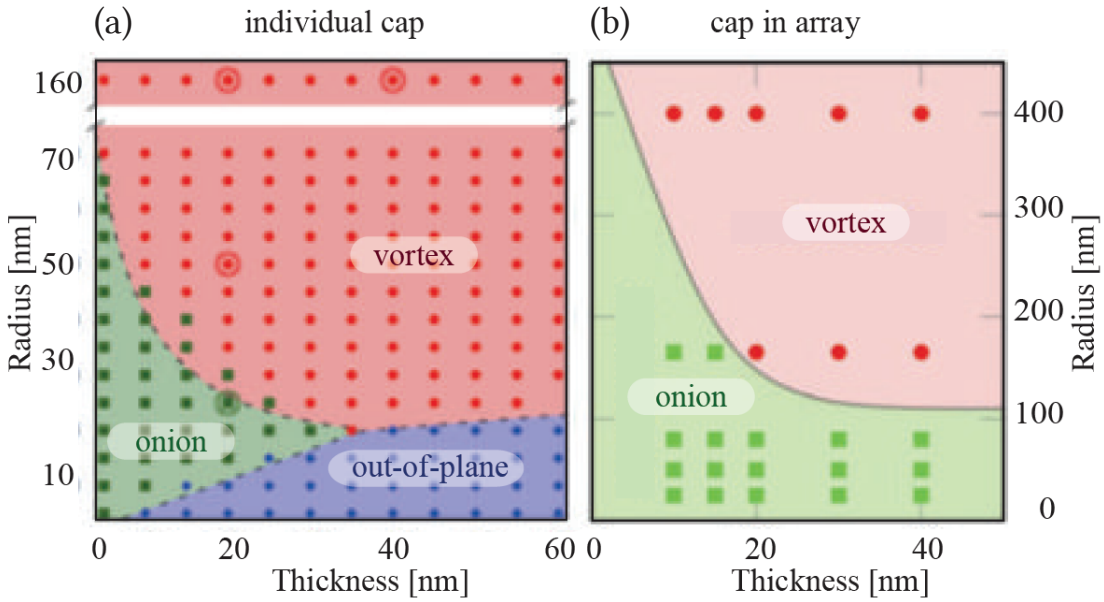

Figure 2.2: Phase diagrams of possible magnetic textures within permalloy spherical half shells for (a) individual caps and (b) caps assembled in arrays, as a function of cap thickness and radius. Data points for individual caps were obtained from simulation (single circles) and experimental results (double circles). Here, the dashed line indicates the simulated phase transition for individual planar discs. Data points for caps in arrays were obtained from PEEM experiments. Note the different scale of the coordinate axes for (a) and (b). Taken from [Reg18]. Adapted from [SKS12, SKR16].

netic moments (vortex state) or uniform surface tangential alignment of magnetic moments in a defined direction (onion state) were visualized. Additionally, they modeled the caps as extruded hemispheres to theoretically construct a phase diagram of equilibrium magnetic states as a function of particle size and cap thickness (cf. Fig. 2.2 (a)) [SKS12]. Besides studies on individual caps, Streubel et al. also investigated the magnetic states of JP caps arranged in closely-packed arrays for the same range of Py film thickness and cap diameter as before [SKR16]. The resulting phase diagram is shown in Fig. 2.2 (b). From these studies it was demonstrated that the phase for the onion state is extended towards larger cap diameters in particle arrays, due to magnetostatic interaction acting during vortex nucleation in the transition from saturation to remanence [SKR16]. In general, analyses on magnetic JPs' caps have shown that when a thin film is deposited on a template particle, the caps cannot be perceived simply as hollow

hemispheres with constant thickness, since the deposition process is not homogeneous when comparing the top and the sides of the particles. This results in a thickness gradient in the cap from the top of the particle (nominal thickness) towards its edge (reduced thickness), which could affect the exhibited cap magnetization state [AHG05, SFK16, Reg22].

From the phase diagrams shown in Fig. 2.2, it can be assumed that the most likely stable magnetization state for individual JPs with softmagnetic permalloy caps in the micrometer size range is a vortex state. In the context of microfluidic particle transport, this means that these particles would move comparably slowly due to the rather small macroscopic magnetic moment formed by the vortex core within their caps. However, the magnetic vortex state of micron-sized JP caps can be switched to an onion state by introducing additional magnetic anisotropies into the system [TRH21, Reg22].

2.4.2 Exchange-Bias Caps

Combining the principles for fabricating ferromagnetic caps exhibiting tailored magnetization states (see previous section) and for inducing a unidirectional anisotropy in thin film systems (cf. Section 2.3.4), micron-sized JPs with stabilized magnetic Onion states can be produced [TRH21, Reg22]. This was found by Tomita et al. by investigating the influence of an EB system on the magnetic state of 1 µm sized JPs assembled in a closely-packed array [TRH21]. They compared via micromagnetic simulations the magnetization state in remanence of two JPs, one silica particle capped with an EB layer system of Cu(5 nm)/$Ir_{17}Mn_{83}$(30 nm)/$Co_{70}Fe_{30}$(10 nm)/Si(10 nm), and another one capped with a layer system without the EB contribution, i.e., without the AF. Figure 2.3 shows the results of micromagnetic simulations for the magnetization distribution within both hemispherical caps. It was observed that by introducing a unidirectional anisotropy to the cap, provided by the exchange interaction at the interface between F and AF, the JP cap reaches an onion state (cf. Fig. 2.3 (a)), whereas the JP cap without this additional anisotropy exhibits a vortex state (cf. Fig. 2.3 (b)). The orientation of magnetic moments for the onion state leads to an effectively larger magnetic moment of the corresponding JP caps compared to those in a vortex state. Thus, JPs with caps exhibiting an onion state at remanence are expected to move faster when their microfluidic transport is induced.

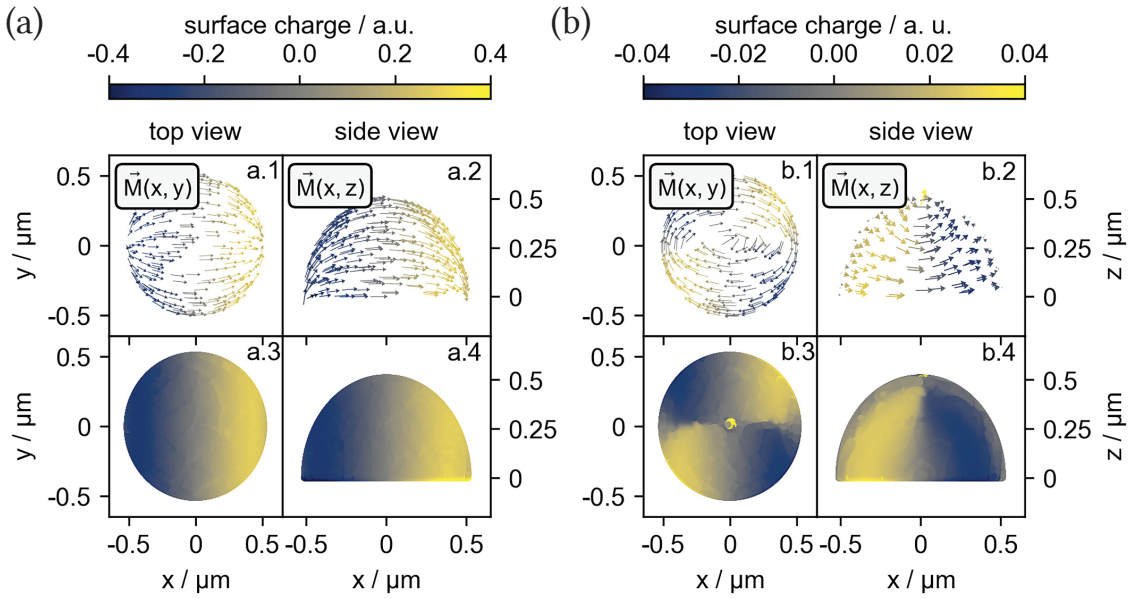

Figure 2.3: Micromagnetic simulations of magnetization distributions within hemispherical caps of 1 µm diameter. (a) Caps consisting of an EB thin film system. (b) Ferromagnetic cap without EB. (a/b.1) and (a/b.2) Projection of the spatial magnetization distribution form the top view and side view, respectively. Similarly, (a/b.3) and (a/b.4) are top and side views of the simulated surface charge distribution. Taken from [TRH21].

Within this project, magnetic JPs were produced by depositing an EB thin film system on top of 3 µm sized template particles. To trigger the formation of different magnetization states within the resulting EB caps, the thickness of the ferromagnetic layer (t_F) was varied between 5 nm and 100 nm. This range of thicknesses is expected to be large enough to result in different cap magnetization textures ranging from onion states to vortex states, as with increasing t_F the EB, as an interface-related effect, looses its unidirectional pinning character [Reg22]. Possibly, a multidomain state can also form, which has been shown to be the the preferred state of disks with a diameter of 3 µm [SAKS09].

2.5 Directed Transport of Magnetic Particles

The investigations presented in this thesis are centered around the controlled transport of magnetic particles, therefore, it is fundamental to introduce the transport concept used to perform the experiments. The concept is based on the gener-

ation of a time-varying potential energy landscape above a topographically planar EB thin film system by means of temporally alternating external magnetic field pulses [HKB15]. The potential energy landscape determines the positions of magnetic particles above the substrate and is generated from the superposition of the external magnetic field pulses with the magnetic stray field landscape (MFL) originating from the thin film substrate.. The MFL is composed of stray fields emerging from transition regions between individual domains within the magnetically structured EB thin film system. In the following, magnetic domain walls with tailored distributions of magnetic charges as the origins of the utilized stray fields will be introduced, followed by the forces acting on the magnetic particles while being transported. Afterward, the physical transport mechanism will be explained. Finally, the state of the art on EB-JPs transport above magnetically patterned substrates will be presented.

2.5.1 Magnetically Charged Domain Walls

The magnetic stray fields emerging from a magnetically patterned domain substrate originate from the accumulation of uncompensated magnetic partial charges at the boundaries of two domains, i.e., areas with uniform magnetization direction [HS98]. These magnetic partial charges can be positive or negative depending on the specific magnetization configuration and act as sources and sinks of domain magnetization. The transition region between two adjacent domains is called a domain wall (DW). It is within this DW volume where a rotation of the magnetization vector takes place, starting from the orientation corresponding to one domain and ending up aligned with the orientation of the adjacent domain. To explain this DW formation, the simplest scenario is to consider two adjacent domains with in-plane antiparallel magnetization separated by a DW. Depending on the rotational axis of the magnetization, vector two types of DWs can be defined: A Bloch wall and a Néel wall. In a Bloch wall, the magnetization vector rotates in a plane parallel to the DW plane, resulting in the formation of magnetic partial charges at the opposite interfaces of the magnetic film (cf. Fig. 2.4 (a)). In contrast, in a Néel wall the magnetization vector rotates in a plane perpendicular to the DW plane, resulting in magnetic partial charges within the DW volume [HS98, Geto8]. The formation of one or the other DW is strongly determined by the thickness of the film d_F. Therefore, Néel walls are preferentially formed in

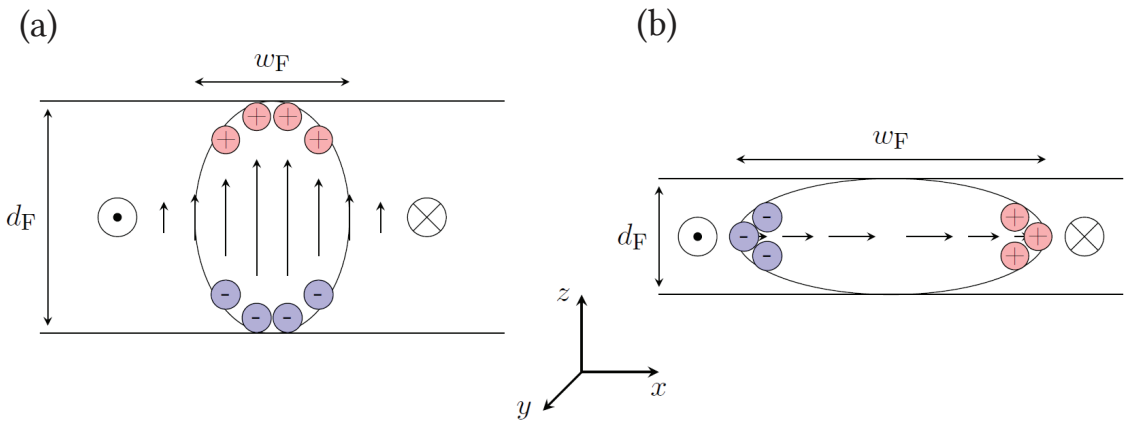

Figure 2.4: Representation of domain walls formed in thin ferromagnetic films of thickness d_F between two domains with in-plane antiparallel magnetization directions (indicated by arrow ends). Depending on the orientation of the spin rotation plane, a Bloch wall (a) and a Néel wall (b) with different domain wall widths w_F and distributions of magnetic partial charges can be identified. Taken from [Hol15]. Adapted from [HS98].

thin films, where the thickness becomes comparable to the DW width w_F [HS98]. In a system with in-plane magnetization $\vec{M}$, a distinction can be made between surface charges ($\sigma_S = \vec{M} \cdot \vec{n}_S$) and volume charges ($\rho_V = -\vec{\nabla} \cdot \vec{M}$), where $\vec{n}_S$ is the surface normal vector [HZK13]. From these surface and volume charge densities, the stray field $\vec{H}(\vec{r})$ emerging from a magnetic film is given by [RMG90]:

$$\vec{H}(\vec{r}) = \int_V \rho_V(\vec{r}') \frac{\vec{R}}{\left|\vec{R}\right|^3} \mathrm{d}V' + \int_S \sigma_S(\vec{r}') \frac{\vec{R}}{\left|\vec{R}\right|^3} \mathrm{d}S' , \tag{2.20}$$

where V is the volume of the film, S its surface area and $\vec{R} = \vec{r} - \vec{r}'$ refers to specific positions within the film. Hence, in Néel walls, the generated stray fields above the surface of the film can be adjusted by inducing a defined spatial distribution of the magnetic volume charges, e.g., by creating charged DWs. Charged DWs are characterized by having an uneven distribution of negative and positive charges, leading to a non-zero net charge (ρ_{net}). In Néel walls, ρ_{net} is given by [HZK13, Hol15]:

$$\rho_{net} = \vec{n}_W \cdot \vec{\Lambda} = \vec{n}_W \left(\vec{M}_1 - \vec{M}_2 \right), \tag{2.21}$$

where $\vec{n}_W$ is the DW normal vector and $\vec{\Lambda}$ is the vector difference between magnetization $\vec{M}_1$ and $\vec{M}_2$ corresponding to the domains divided by the DW. Hence, ρ_{net}

is maximized for DWs with adjacent domains with opposite in-plane magnetization orientation. This domain magnetization configuration is typically referred to as head-to-head or tail-to-tail DW, and can be imprinted into an EB thin film system via IBMP (cf. Section 2.3.4) [HZK13]. A substrate patterned with such a repeating domain configuration leads to a formation of a micro-scaled periodic MFL above the substrate, which can be used for directed microfluidic transport of magnetic particles [HKB15].

2.5.2 Acting Forces

In the microfluidic particle transport system used in this project, different forces dictate the motion dynamics of magnetic particles (cf. Fig. 2.5). However, the directed transport of the magnetic particles is achieved primarily from the interaction of the particles with the MFL generated above the EB patterned substrate. Taking the case where the particles are transported above an EB system with a hh/tt domain magnetization configuration, a defined distribution of the magnetic partial charges at the DWs can be assumed. This magnetic charge distribution leads to an inhomogeneous magnetic stray field landscape (along the x- and z-axes). Hence, the magnetic particles are attracted to the DWs where the stray field density is at maximum. The distribution of the magnetic stray field $\vec{H}_{\mathrm{MFL}}(x,z)$ over one DW transition along the x-axis can be calculated for the x- and z-components according to the analytic model from Rugar et al. [RMG90]:

$$H_{\mathrm{x}}(x,z) = 4M_{\mathrm{r}}\left[\tan^{-1}\left(\frac{x\,(t_{\mathrm{F}}+z)}{x^2+a^2+a\,(t_{\mathrm{F}}+z)}\right)-\tan^{-1}\left(\frac{x\,z}{x^2+a^2+a\,z}\right)\right], \tag{2.22}$$

$$H_{\mathrm{z}}(x,z) = 2M_{\mathrm{r}}\,\log\left(\frac{x^2+(t_{\mathrm{F}}+z+a)^2}{x^2+(z+a)^2}\right), \tag{2.23}$$

where M_{r} is the remanent magnetization of the F layer, t_{F} the thickness of the F, z the distance and a the domain transition parameter. Assuming that the patterned substrate has n identical domain transitions, the distribution of the magnetic stray field for the total MFL can be written by superposing the stray fields generated from individual DWs. Considering that hh- and tt-DWs have different polarity and are separated by the domain width w, with the periodicity of the pattern situated along the x-axis, $\vec{H}_{\mathrm{MFL}}$ can be written as [RMG90, Hol15]:

$$\vec{H}_{\mathrm{MFL}}(x,z) = \sum_{n}(-1)^n\,\vec{H}(x-nw,z)\,. \tag{2.24}$$

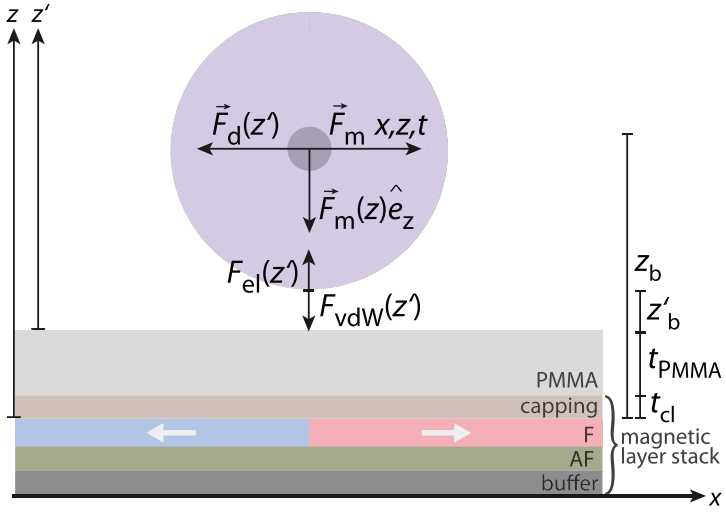

Figure 2.5: Schematic representation of the relevant forces acting on a magnetic particle within the microfluidic particle transport system. Along the vertical axis, the electrostatic ($F_{el}(z')$), van der Waals ($F_{vdW}(z')$), and magnetic force ($\vec{F}_m(z)\hat{e}_z$) are indicated. The drag ($\vec{F}_d(z')$) and time-dependent magnetic force ($\vec{F}_m(x,z,t)$) determine the lateral particle velocity. The thin film system consists of a buffer layer, an EB bilayer and a capping layer of thickness t_{cl} and is covered with a PMMA spacer of thickness t_{PMMA}. Here, $z = z' + t_{cl} + t_{PMMA}$. Modified from [RHE21].

The potential energy of the magnetic particle can be calculated from the scalar product between its time-dependent magnetic moment $\vec{m}_p(x,y,z,t)$ and the effective magnetic field $\vec{H}_{eff}$ [HKB15]:

$$U_p(x,y,z,t) = -\mu_0\, \vec{m}_p(x,y,z,t) \cdot \vec{H}_{eff}(x,y,z,t)\,. \tag{2.25}$$

Here, $\vec{H}_{eff}$ is obtained from the superposition of the time-dependent externally applied magnetic field $\vec{H}_{ex}(x,z,t)$ and the static MFL $\vec{H}_{MFL}(x,z)$:

$$\vec{H}_{eff}(x,z,t) = \vec{H}_{ex}(x,z,t) + \vec{H}_{MFL}(x,z)\,, \tag{2.26}$$

where, $\vec{H}_{ex}(x,z)$ is assumed to be in a range where it does not affect the remanent magnetic state of the substrate. Considering that the magnetic force exerted on the magnetic particles $\vec{F}_m$ is proportional to the applied field gradient [Huh22]:

$$\vec{F}_{mag} = \mu_0 \left(\vec{m} \cdot \vec{\nabla}\right) \cdot \vec{H}\,, \tag{2.27}$$

and taking Eq. 2.25, $\vec{F}_\mathrm{m}$ can be written as [Hol15]:

$$\vec{F}_\mathrm{m} = -\vec{\nabla} U(x, y, z, t) = \mu_0 \left(\vec{m}_\mathrm{p}(x, z, t) \cdot \vec{\nabla}\right) \cdot \vec{H}_\mathrm{eff}(x, z, t)\,. \tag{2.28}$$

Thus, the magnetic force $\vec{F}_\mathrm{m}$ acting on the particles has the contribution of both, $\vec{H}_\mathrm{ex}$ and $\vec{H}_\mathrm{MFL}$, which leads to the particles being located above the DWs. $\vec{F}_\mathrm{m}$, in particular its z-component $\vec{F}_\mathrm{m}(z) \cdot \hat{e}_z$, is the main force attracting the magnetic particles towards the substrate, however, the particles do not physically touch the substrate due to other forces balancing their z-position, i.e., their steady-state distance from the substrate. To get a numerical expression of $\vec{F}_\mathrm{m}$, it is necessary to know $\vec{m}_\mathrm{p}$, which depends on the type of magnetic particle. In the case of magnetic JPs with remanent magnetization within their caps, such as those used in this project (cf. Section 2.4), a fixed magnetic moment can be assumed under the condition that $\vec{H}_\mathrm{ex}$ does not change the remanent state of the particles. It has been shown that this is true for the EB capped JP [HRT21]. However, for other magnetic particles, e.g., superparamagnetic beads, their magnetic moment is determined by $\vec{H}_\mathrm{eff}$ [Hol15, Huh22]. In addition to this, $\vec{H}_\mathrm{eff}$ also exerts a torque $\vec{\tau} = \vec{m} \times \vec{H}_\mathrm{eff}$ on the magnetic particles, however, this only holds true for particles where $\vec{m}$ is not aligned to an external magnetic field via remagnetization or spin flip.

Another primary force acting on the particles that needs to be considered is the drag force $\vec{F}_\mathrm{d}$. This force originates from the friction that the surrounding liquid exerts on the particles upon movement and can be approximated for the here considered system by Stokes' law under the condition of laminar flow and at small Reynolds numbers [WSFX05]:

$$\vec{F}_\mathrm{d}(x, z) = -6\pi\, r_\mathrm{p}\, \eta\, \vec{v}_\mathrm{p}(x, z)\, f(z)\,. \tag{2.29}$$

Here, r_p is the hydrodynamic radius of the particle, η is the viscosity of the surrounding fluid, and $f(z)$ is the z-distance dependent drag force coefficient. Hence, a equilibrium of this force and $\vec{F}_\mathrm{m}$ leads to a steady-state velocity for the particle [HKB15]:

$$\vec{v}_\mathrm{p}(x, z) = \frac{\mu_0 \left(\vec{m}_\mathrm{p}(x, z) \cdot \vec{\nabla}\right) \cdot \vec{H}_\mathrm{eff}(x, z)}{6\pi\, r_\mathrm{p}\, \eta\, f(z)}\,. \tag{2.30}$$

Here, the usually very short acceleration time of the particle can be neglected, for which reason $\vec{v}_\mathrm{p}$ describes the velocity of a particle in a time-constant $\vec{H}_\mathrm{eff}$.

In addition to the aforementioned forces, the gravitational force F_g and the buoyancy force F_b also have to be taken into account for objects in a liquid

medium. These forces act on the particle in opposite directions. Therefore, whether the particle floats closer to the liquid surface or to the substrate surface depends on the relationship between these two forces. These forces are given by $F_g = V_p \rho_p g$ and $F_b = V_p \rho_l g$, with V_p and ρ_p the volume and density of the particle, ρ_l the density of the liquid and g the gravitational constant. Hence, the critical condition for sinking or ascending of a particle is the ratio between ρ_p and ρ_l, i.e., for $\rho_p > \rho_l$ the particle sediments and for $\rho_p < \rho_l$ buoyancy occurs.

DLVO Forces

The DLVO forces, named after Derjaguin, Landau, Verwey and Overbeek [WSFX05], incorporate the electrostatic force $\vec{F}_{el}$ and the electrodynamic van der Waals force $\vec{F}_{vdW}$. They can be described as surface forces mediating the colloidal stability of a system (cf. Fig. 2.5) [WSFX05]. For this system in particular, the forces influence the steady-state z-position of the particle above the substrate. $\vec{F}_{vdW}$ represents the electrodynamic interaction between two surfaces (here, particle and substrate) separated by a liquid medium, while $\vec{F}_{el}$ describes the Coulomb interaction arising from adsorption of ions from the liquid medium on both surfaces [Huh22, WSFX05]. Typically, $\vec{F}_{vdW}$ has an attractive character (cf. Fig. 2.5) due to the interaction of induced dipoles in the electrically neutral atoms involved and is highly dependent on the geometries of the objects, the distance between them and the medium surrounding them [Huh22, WSFX05]. For the case where these objects are spheres, Hamaker derived a general equation for the retarded $\vec{F}_{vdW}$ [Ham37], from which the interaction between a sphere and a flat substrate can be expressed as [Isr11]:

$$\vec{F}_{vdW} = -\frac{A_{123}\, R}{6z^2}\left[\frac{1}{1 + 14\, z/\lambda_{ret}}\right]\hat{e}_z\,. \tag{2.31}$$

Here, A_{123} is the Hamaker constant for a sphere of material 1 with radius R at a distance z from the substrate of material 2 with infinite surface surrounded by the liquid medium 3 [Isr11]. This constant considers a retarded $\vec{F}_{vdW}$, which is the case for distances above 5 nm [BGK03]. Additionally, λ_{ret} represents a characteristic wavelength of the retardation.

On the other hand, the electrostatic interaction $\vec{F}_{el}$ has to be also considered to determine the z-position of the particle. This interaction arises from the electrical charged surfaces of both substrate and particle, which can be charged from:

Adsorption or binding of ions from the surrounding medium, ionization and dissociation of chemical surface groups, and/or transfer of electrons or protons between two closely spaced surfaces [Huh22, Isr11]. A charged surface in contact with a fluid medium is compensated by oppositely charged bound and unbound ions from the surrounding liquid, thus reducing the effective surface potential by forming a so-called electrochemical double layer, also known as the Stern layer [Huh22, BGK03]. Hence, the attractive or repulsive character of $\vec{F}_{\mathrm{el}}$ is determined from the interaction between both electrochemical double layers, which is defined by the respective surface potentials of the substrate Ψ_{s} and particle Ψ_{p}, the permittivity ϵ of the surrounding medium and the Debye length κ [WSFX05]:

$$\vec{F}_{\mathrm{el}} = \frac{2\pi\,\epsilon\,\kappa\,R}{1-\mathrm{e}^{-2\kappa z}}\left[2\,\Psi_{\mathrm{s}}\,\Psi_{\mathrm{p}}\,\mathrm{e}^{-\kappa z} \mp \left(\Psi_{\mathrm{s}}^2+\Psi_{\mathrm{p}}^2\right)\mathrm{e}^{-2\kappa z}\right]\hat{e}_z\,. \tag{2.32}$$

2.5.3 Transport Mechanism

Having introduced the particle transport concept, the generation of stray fields used to induce the transport and the main forces governing particle mobility, the theoretical background is complemented by describing the actuation mechanism used to transport EB capped JPs. This mechanism, developed by Holzinger et al., requires a magnetically structured EB substrate with an hh/tt magnetization configuration of parallel-stripe domains and was initially used in combination with superparamagnetic particles (SPPs). The mechanism consists of dynamically transforming the potential energy landscape of the particles $U_{\mathrm{p,z}}$ by means of external trapezoidal magnetic field pulses in z- and x-direction as shown in Fig. 2.6 [HKB15]. Different studies on the directed, remotely controlled transport of superparamagnetic particles in MFLs of varying complexity validate the effectiveness of this mechanism [HKB15, Deu16, Gö19, RHE21, HRS22]. The mechanism is better understood when following the temporal evolution of $U_{\mathrm{p,z}}$ above the EB substrate as a function of the applied external magnetic field sequence (cf. Fig. 2.6 (a)-(e)).

When performing a transport experiment, at first no external magnetic fields are applied and the SPPs sediment until reaching a certain position close to the substrate, in particular above a DW, as these positions are energetically preferred due to the stray fields emerging from them. Hence, SPPs create particle rows with the same periodicity than the stripe pattern, in this case, every 5 µm (cf. Fig. 2.6), with the particles aligning parallel to the corresponding stray field. For the first

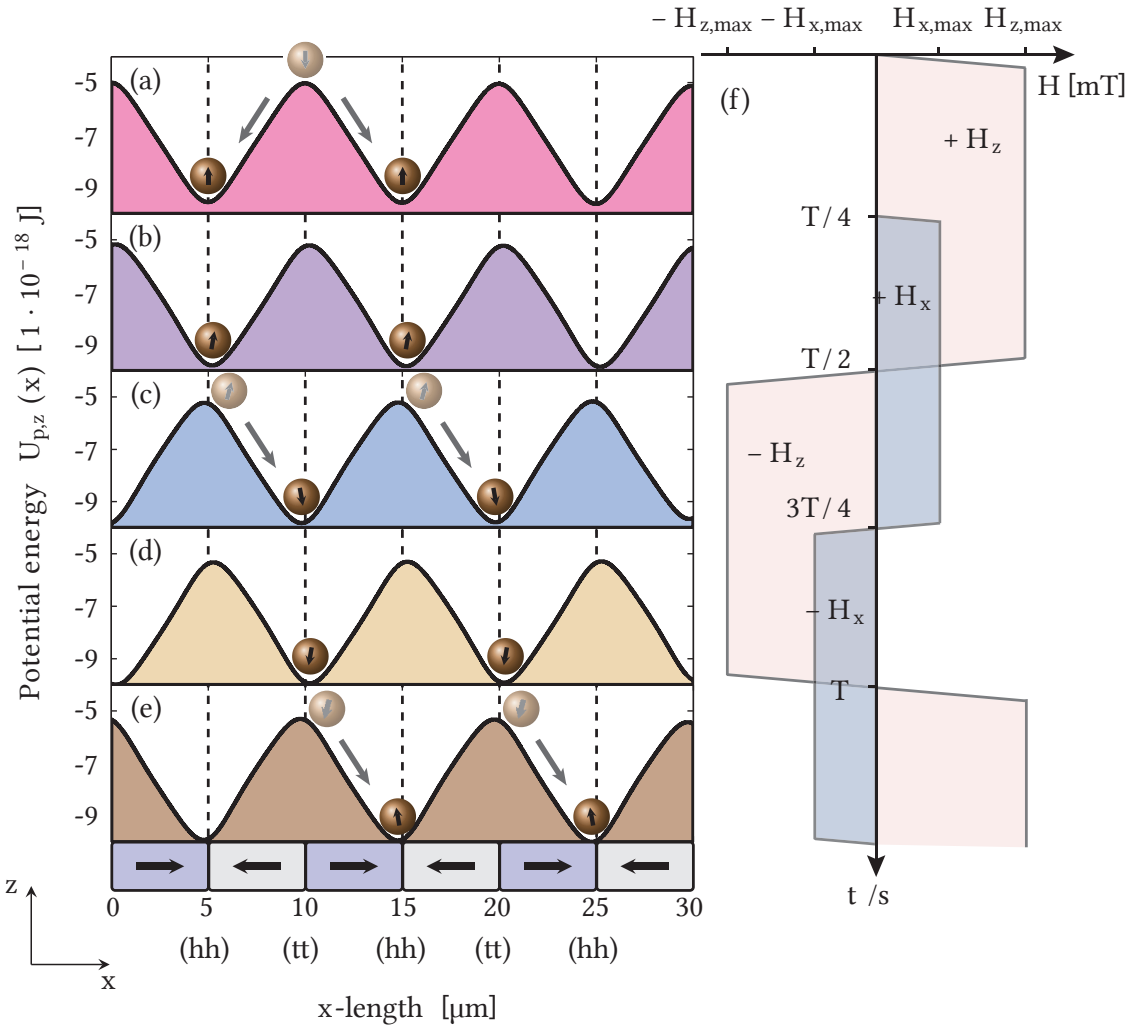

Figure 2.6: Schematic representation of the magnetic particle transport mechanism. The particles are transported above a EB thin film system with parallel-stripe domain pattern and hh/tt magnetization configuration. Directed magnetic particle transport is induced by dynamically transforming the potential energy landscape $U_{p,z(x)}$ (a)-(e) through a sequence of applied external magnetic field pulses (f). An inversion of H_z transforms the potential energy landscape such that previous maxima convert to minima and vice versa, resulting in transition of particles from one DW to the neighboring DW (e.g., from (b) to (c) and (d) to (e)). The inversion of H_x slightly shifts the potential energy landscape along the x-axis (e.g., from (c) to (d)), thereby defining the direction of the subsequent movement. Adapted from [Hol15].

step, an external magnetic field pulse in $+z$-direction $+H_{\mathrm{z,max}}$ is applied (cf. cf. Fig. 2.6 f)), causing the degeneracy of potential energy minima above hh- and tt-DWs to vanish for the particles, i.e., there are now energy minima above hh-DWs and maxima above tt-DWs. Consequently, SPPs perform lateral motion steps towards the newly formed minima. The direction of this movement (positive or negative x-direction) is, however, statistically distributed at first. Next, at $T/4$ for the external magnetic field pulse sequence (cf. Fig. 2.6 (f)), a field in $+x$-direction $+H_{\mathrm{x,max}}$ is now additionally applied. As can be seen in the resulting potential energy landscape (cf. Fig. 2.6 (b)), the minima for the particles are now slightly shifted toward positive x-direction. This leads to a small step of SPPs and a tilting of the respective magnetic moments (black arrows), as they are aligning with the direction of the effective magnetic field $\vec{H}_{\mathrm{eff}}$ (cf. Eq. 2.26). In the next step, at $T/2$ for the external magnetic field sequence (cf. Fig. 2.6 (f)), a large transport step of the particles is initiated. Here the sign of the $H_{\mathrm{z,max}}$ is inverted, i.e. a magnetic field pulse in $-H_{\mathrm{z,max}}$ is applied, leading to another transformation of the potential energy landscape now creating minima above the tt-DWs and maxima above the hh-DWs (cf. Fig. 2.6 (c)). Since $+H_{\mathrm{x,max}}$ slightly shifted the particles' position away from the center of the hh-DWs, a unified motion of the particles in the positive x-direction is now favored. Again, due to $H_{\mathrm{x,max}}$, the position of minima is not directly above tt-DWs but with a small shift towards negative x-direction with respect to the DW center. The lateral transport of the particles is again accompanied by a realignment of the particles' magnetic moments towards the new $\vec{H}_{\mathrm{eff}}$. To continue transporting the particles in the positive x-direction, an inversion of the sign for $H_{\mathrm{x,max}}$, induced at $3T/4$ (cf. Fig. 2.6 (f)), is necessary. This again leads to a small transport step of the particles towards the other side of the tt-DWs now, as can be seen by the potential energy landscape shown in Fig. 2.6 (d). Again, the magnetic moments of the particles are also realigned. Finally, the sign of $H_{\mathrm{z,max}}$ is inverted at T (cf. Fig. 2.6 (f)), thus completing a full cycle for the external field sequence. Once again the potential energy landscape of the particles is transformed, creating minima above hh-DWs and maxima above tt-DWs (cf. Fig. 2.6 (e)), thus resembling the initial situation after the first $H_{\mathrm{z,max}}$ was applied. The particles again perform a large lateral transport step towards the newly formed positions of energy minima, placing them above the hh-DWs but with a slight displacement with respect to the DW center with their magnetic moments realigned. To summarize, the described periodic transformation of the potential energy land-

scape for SPPs above a parallel-stripe domain pattern with hh/tt magnetization configuration by applying several cycles T of trapezoidal magnetic field pulses in x- and z-direction leads to a directed, step-wise particle transport along positive or negative x-direction. To illustrate the transport mechanism, only a transport in one direction (positive x-direction) was described, however, transport can also be initiated in the other direction (negative x-direction) by inverting the phase relation between $H_{\mathrm{x,max}}$ and $H_{\mathrm{z,max}}$. Furthermore, this mechanism can be used to induce 2D (in xy-plane) particle transport if a magnetic field in y-direction $H_{\mathrm{y,max}}$ is additionally applied and inverted within the same phase than $H_{\mathrm{x,max}}$. This concept was first introduced for SPPs, but, as Huhnstock et al. have shown, is also applicable for EB-JPs [HRT21]. As this work forms the basis for the experiments conducted within this thesis, it will be introduced in the following section.

2.5.4 Janus Particles in Dynamically Transformed Magnetic Field Landscapes

Huhnstock et al. investigated the question of whether magnetically capped Janus particles subjected to the same prototypical transport mechanism presented in the previous section would also perform a directed lateral translational motion, but in addition defined rotations. This was expected, as the magnetic Janus particles used incorporate a spatially fixed remanent magnetic moment within their caps and not a magnetic field-dependent moment like SPPs. They used 3 micron-sized EB-JP, leading to the assumption that the EB-related unidirectional anisotropy stabilizes an onion magnetic texture within the caps (cf. Section 2.4.2) [HRT21, TRH21]. Therefore, due to the fixed net magnetic moment of the caps, the particles, when subjected to a temporally changing magnetic field should reorient their magnetic moments by the so-called Brownian relaxation, i.e. by a physical rotation of the whole particle [CBV13]. On the contrary, SPPs are likely to perform Néel relaxation in this case, which means that the particles do not physically rotate, but realign their magnetic moment by spin flip instead [TKW13].

In their proof-of-concept experiment, Huhnstock et al., subjected the EB-JP inside a microfluidic environment to the MFL emerging from a parallel stripe domain pattern with 5-micron stripe width and a hh/tt magnetization configuration [HRT21], just like Holzinger et al. did for SPPs [HKB15]. When applying

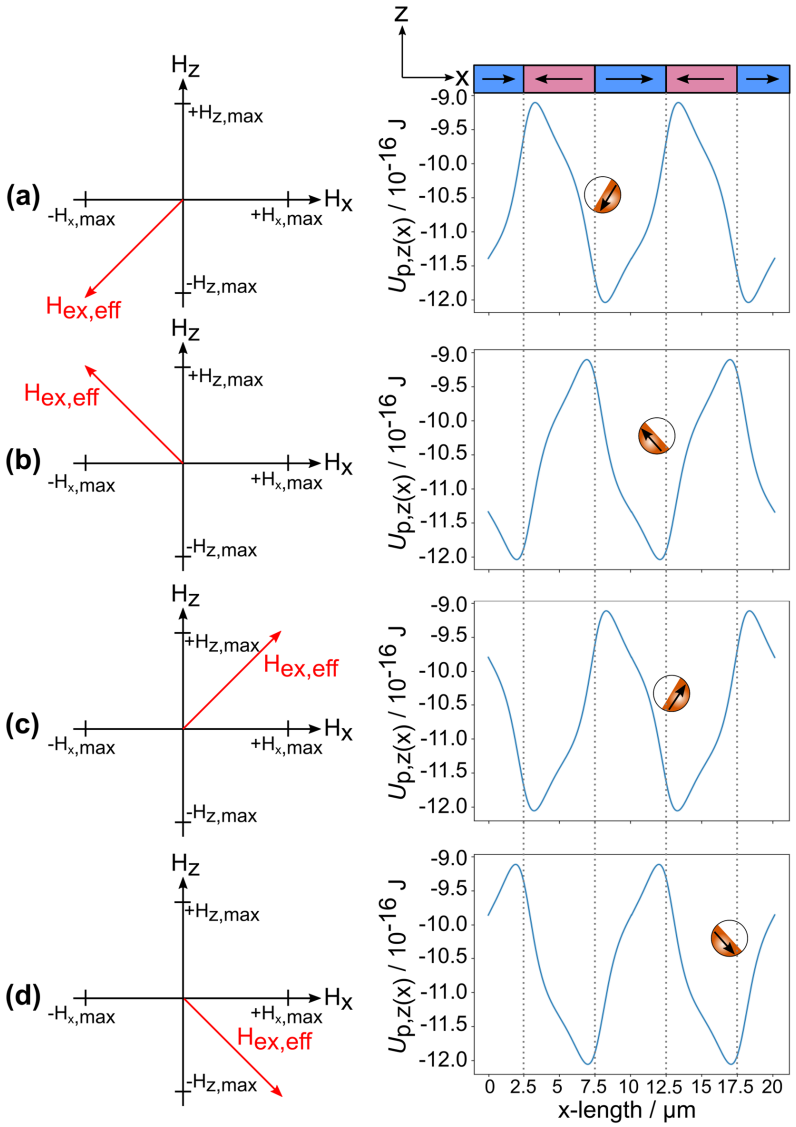

Figure 2.7: Correlation of EB-JPs lateral position and spatial orientation with respect to $U_{p,z}(x)$ (right column) and $H_{ex,eff}$ (left column). The calculated $U_{p,z}(x)$ is shown in blue, solid lines and a representation of the magnetic moment of EB-JP caps is depicted by a black arrow aligned with $H_{ex,eff}$. (a)-(d) Order of external magnetic field configurations applied in a magnetic field pulse sequence during transport experiments. Taken from [HRT21].

external magnetic fields in the perpendicular to the substrate plane z-direction, they observed that particles were trapped above either hh- or tt-DWs (depending on the direction of the z-field). Each displacement of the EB-JPs was accompa-

nied by a defined spatial orientation of the visible magnetic cap of the particles. This spatial orientation was attributed to the alignment of the fixed net magnetic moment of the caps with the direction of the externally applied field, effectively leading to a torque exerted onto the particles [HRT21]. Starting from this observation, periodic magnetic field pulses in x- and z-direction were applied in the same fashion as shown in Fig. 2.6 (f). This resulted in a step-wise directed translational movement of the EB-JP along the x-direction, whereby each transport step was accompanied by a distinct rotational motion of the particles. Evaluating the transport motion speed of the EB-JP, their steady-state velocities were found to be around 200 µm/s, which is an order of magnitude larger than previously reported motion speeds for magnetic JPs [HRT21]. Looking closer at the rotational dynamics of the particles, they were found to rotate around different axes depending on whether a large or a small transport step was performed. As Fig. 2.7 illustrates, these different rotation axes can be explained when looking at the configuration of the effective external magnetic field vector $H_{\text{ex,eff}}$ throughout the experiment (left side of Fig. 2.7) and relating it to the observed spatial orientation of the EB-JP (right side of Fig. 2.7). Here, the initial direction of $H_{ex,eff}$, defined by negative directions of the external magnetic fields in z- and x-directions (cf. Fig. 2.7 (a)), cause a corresponding alignment of the fixed net magnetic moment within the EB-JP cap. For this $H_{ex,eff}$ configuration, the EB-JP is placed above a tt-DW, as confirmed by the calculated potential energy landscape (blue solid lines on the right side of Fig. 2.7) for the particle, which positions energy minima above tt-DWs. Due to the external x-field, the energy minima are not placed directly above the DWs center, but are slightly shifted sideways (see previous section). Then, by changing the sign of the z-field which is now positive, potential energy minima are shifted to the positions of hh-DWs and the magnetic moment of the EB-JP is realigned with the new direction of $H_{\text{ex,eff}}$ (cf. Fig. 2.7 (b)). This realignment is only possible by rotating the whole particle around an axis along the y-axis (not shown here). Afterward, the sign of the x-field is inverted (cf. Fig. 2.7 (c)), leading to another reorientation of the EB-JP cap magnetic moment and, consequently, to another rotational motion to achieve this realignment. In this case, however, realignment is only possible by rotating the particle around the z-axis. As can be seen by the calculated potential energy of the particle in this case, this rotation is occurring when a small transport step is performed. In the last step, the sign of the z-field is inverted again, causing the EB-JP to rotate again around the y-axis

due to the new direction of the $H_{\mathrm{ex,eff}}$ along with conducting a large transport step in the positive x-direction.

The results obtained from the described proof-of-concept experiment of Huhnstock et al. will be the basis of the investigations carried out within this thesis. In addition to their work, the influence of the thickness of the ferromagnetic layer t_{F} within the EB cap on the particles' motion dynamics, as well as the motion behavior of prototypical EB-JP within a dynamically transformed 2D potential energy landscape, will be studied in the following. Before that, the used experimental methods will be introduced in the next chapter.

3 Experimental Methods

This chapter presents the experimental methods used to carry out the experiments of this thesis. First, the fabrication process of the Exchange-Bias Janus particles (EB-JP) is described in detail in Section 3.1. Afterward, Kerr magnetometry is explained in Section 3.2. This technique was applied for the magnetic characterization of the sample used for the two-dimensional (2D) transport. Section 3.3 presents the experimental setup employed to perform the EB-JPs transport experiments along with the corresponding sample preparation. Finally, in Section 3.4, the software used to track the particles' motion from the recorded videos is introduced, and two tracking modes are described. These tracking modes were used systematically for one-dimensional (1D) and 2D particle transport analysis.

3.1 Fabrication of Exchange-Bias Capped Janus Particles

EB-JPs were fabricated by depositing an EB thin film system on top of self-assembled spherical polystyrene particles with a nominal diameter of 3 µm. A step-by-step description of the fabrication procedure is given in the following.

3.1.1 Self-Assembly of Template Particles

Glass slides with a size of ca. 15 mm × 10 mm were used as base substrates for the self-assembly of polystyrene template particles. The substrates were exposed to a concentrated sulfuric acid bath for 24 hours to enhance the attraction between the substrate and water molecules [MFO95]. This attractive interaction improves the distribution of the particle suspension on the substrates during self-assembly. Afterward, the substrates were stored in a container with ethanol to prevent them

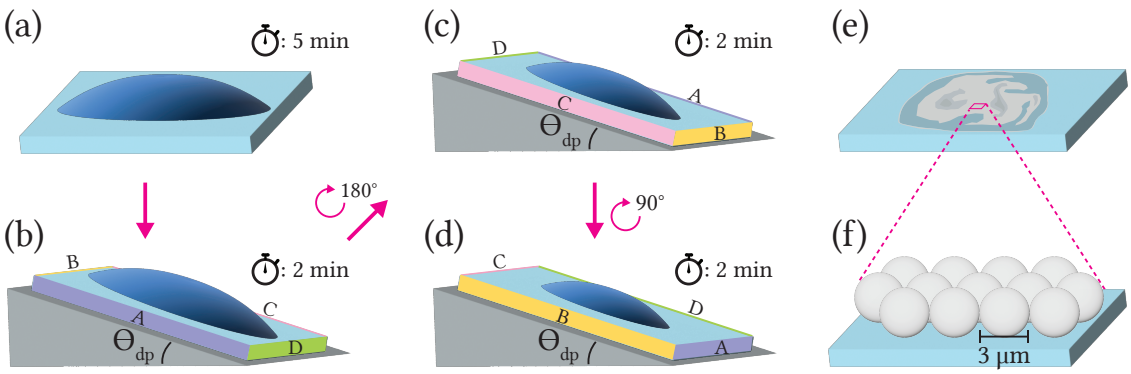

Figure 3.1: Depiction of the particle self-assembly procedure: (a) A droplet of the particle dispersion is placed in the middle of a previously cleaned glass substrate and is left for sedimentation for 5 min. (b) The substrate is transferred onto the heating device set at an angle (θ_{dp}). (c)-(d) The substrate is rotated 180° and 90° respectively, maintaining each orientation for 2 min. (c) and (d) are repeated until the droplet evaporates completely, remaining only the particles adhering to the glass (e). The particles are distributed in regions of multi- and monolayers. (f) Monolayer of hexagonal self-assembled particles. Adapted from [Reg22].

from losing their hydrophilic property and getting contaminated. Additionally, before usage, the substrates were cleaned with isopropyl alcohol.

For the self-assembly of the particles, the methodology described by *Micheletto et al.* in [MFO95] was followed. The parameters were varied as displayed in Table A.1 in Appendix A.1. Here, 3 µm nominal diameter micromer® particles from *micromod Partikeltechnologie GmbH* were used as template. These are polystyrene particles suspended in water with a nominal concentration of 50 mg/mL.

The first step in the particle self-assembly procedure was to set a heating plate to an inclination angle θ_{dp} and a temperature T_{dp}. Then, a droplet of volume V_d with a concentration c_p of particles suspended in distilled water was placed on the center of a clean glass substrate (see Fig. 3.1 (a)). After five minutes (to allow sedimentation of the particles), the substrate with the droplet was carefully moved onto the tilted sample heating device. Once the substrate was in position, a sequence of in-plane rotations alternating between 180° and 90° every two minutes was performed (see Fig. 3.1 (b)-(d)). These rotations improve the droplet distribution, and thereby the particle distribution, over the substrate during the evaporation process. The evaporation of the liquid takes place mainly at the top border of the sample [MFO95]; there, the contact area between the droplet and

the glass is reduced from the border to the center, dragging the particles closer to each other, thus forming closely-packed arrays. Then, by rotating the sample, the evaporation will occur on another area of the substrate (at the new top border), keeping the droplet in circular rather than oval form (cf. Fig. 3.1 (e)). The homogeneous distribution of particles over the whole area decreases the creation of multilayers of arrays of particles. This is advantageous for the efficient production of magnetically capped Janus particles as the subsequent sputter deposition procedure solely functionalizes the particles at the top of a multilayer structure. Thus, the particles underneath are not usable for microfluidic transport experiments due to their lack of a magnetic cap.

3.1.2 Thin Film Sputter Deposition on Assembled Particles

The assembled particles were capped with magnetic thin films by sputter deposition in radio-frequency (RF) mode. The machine employed for this process was a *Leybold Heraeus Z*400 and its setup is schematically depicted in Fig. 3.2 (a).

Sputter deposition is a thin film fabrication technique within the category of physical vapor deposition (PVD) [Ses12]. In this technique, high-energetic ions collide with a solid target, thereby ejecting its atoms. The free atoms are then adsorbed on the sample surface, where they will diffuse and eventually form molecule-molecule and molecule-surface bonds. As more atoms/molecules aggregate to the surface (nucleation), a self-organized film-like structure grows [Mer22, Pae02, Ses12].

This process is carried out in a vacuum chamber, generally maintained at a base pressure $p_{\text{base}} > 10^{-6}$ mbar. Here, an inert gas, in this case, argon (Ar), is initially supplied at a maximum flow rate of 200 sccm. After the ignition of the Ar plasma via gas discharge, the Ar flow is reduced to 140 sccm to achieve a working pressure $p_{\text{sputter}} \approx 10^{-2}$ mbar for the sputtering process [Mer22]. The ignition of the plasma and the further acceleration of its ions (Ar^+) is achieved through a potential difference created between the grounded substrate holder (anode) and the target (cathode). In RF mode, an alternating current (AC) voltage is applied to the cathode with a radio frequency of ~ 13.6 MHz [Ses12, Pae02], inducing an oscillation movement of the plasma Ar^+ and free electrons in opposite directions, where the electrons, due to their lighter mass, will reach the substrate and target more easily. The electrons arriving at the substrate will dissipate from the system

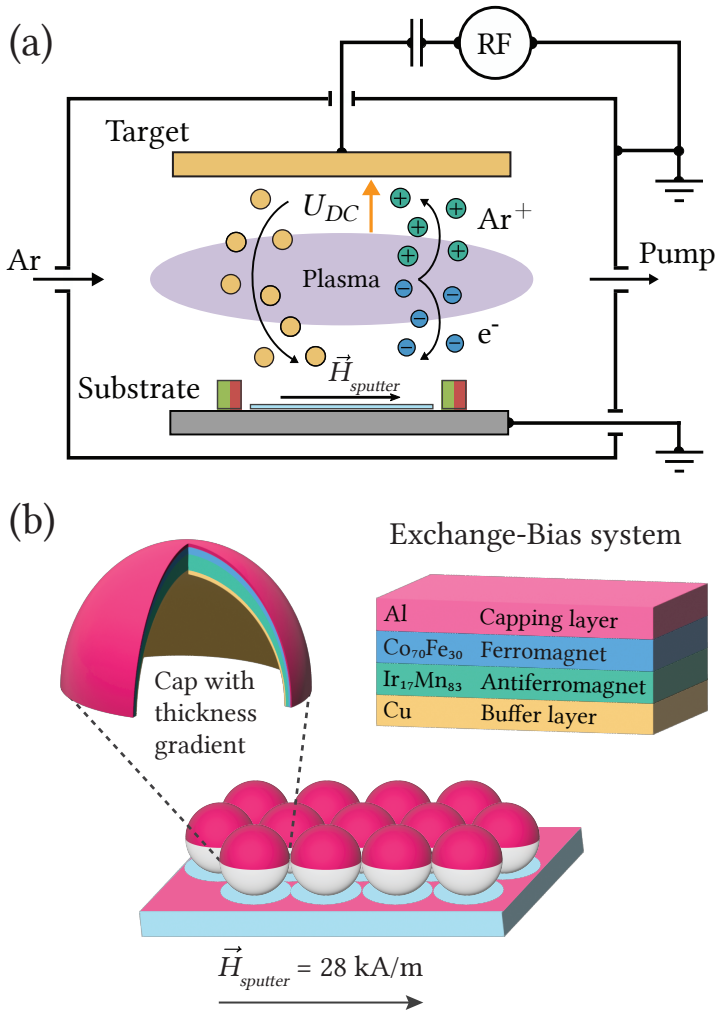

Figure 3.2: (a) Schematic representation of the main components in a sputter deposition system in RF mode. The ions (Ar^+) from the argon plasma are accelerated towards the target via the given potential (U_{DC}) created between the substrate and target. Due to collisions with the target, the ions eject target atoms into the chamber, which are eventually adsorbed on the substrate surface. (b) Depiction (not to scale) of the 3 µm particle array half-covered with the thin film system. The selected EB system consists of a buffer layer/antiferromagnet (AF)/ferromagnet (F)/capping layer stack. The sliced magnetic cap illustrates the thickness gradient formed from its pole towards the edges. For the latter, an Cu(5 nm)/IrMn(30 nm)/CoFe(10 nm)/Al(5 nm) system was taken as reference, keeping the ratio between layers to scale. Adapted from [Mer18] and [Reg22].

through grounding, whereas the ones reaching the target will accumulate there due to the capacitor, which isolates the target from the power source. In con-

sequence, a potential difference (U_{DC}) between the plasma and the target builds up. This potential decelerates the electrons while simultaneously accelerating the Ar^+ towards the target. The formation of this potential induces the collisions of the Ar^+ into the target, hence, initiating the sputtering process. This way of accelerating the Ar^+ towards the target makes the RF mode particularly relevant for the deposition of insulating materials. Additionally, the oscillatory motion of the electrons and Ar^+ in the plasma increases the number of collisions with the Ar atoms, leading to higher ionization rates, which results in higher deposition rates [Mer22, Pae02, Ses12].

For the sputter deposition on top of self-assembled arrays of particles, an EB thin film system was chosen. The layer stack starts with a Cu buffer layer, followed by an $Ir_{17}Mn_{83}$ AF layer, and a $Co_{70}Fe_{30}$ F layer, and culminates with an Al capping layer to prevent the underlying system from oxidation (see Fig. 3.2 (b)). The samples with the particle arrays were then fixed onto a sample holder with Kapton® tape and inserted through a load-lock chamber into the main chamber. In addition to the previously explained elements, a homogenous magnetic field $\vec{H}_{\text{sputter}} = 28$ kA/m was applied parallel to the substrate surface by using two permanent magnets (see Fig. 3.2 (a)). This induces a unidirectional magnetic anisotropy (cf. Section 2.3.4) in the F layer during the sputtering process. This anisotropy is induced due to the pairing of the uncoupled interfacial spins in the AF layer with the F layer on top, which establishes a magnetically ordered state in the system [MHR20]. Moreover, the presence of a magnetic field during deposition increases the sputter rate due to its influence on the plasma [Mer22, Ses12].

Once the sputter deposition process is completed, the final result will be a substrate composed of arrays of half-covered particles and fully covered flat areas (cf. Fig. 3.2 (b)). In the regions with multilayers of particles, only those particles at the surface of the volume will get covered. Hence, the particles underneath will have non to lesser magnetic content on their surface. The latter particles will not reflect the properties to study in this work and, therefore, will be discarded during the evaluation phase of the experiments (cf. Section 3.4). Additionally, to induce different magnetic states (cf. Section 2.4) in the cap of the EB-JPs, particles with different F layer thicknesses were produced. The values for the buffer, AF and capping layer were kept constant, while the thickness of the F was variated from 5 nm to 100 nm (cf. Table 3.1).

Table 3.1: Parameters for the sputter deposition of thin film on top of the self-assembled particle arrays. Different JPs were produced by changing the thickness of the $Co_{70}Fe_{30}$ layer, while keeping the rest of the system constant. The sputter rates on the same side of the column (left/right) correspond to similar deposition batches.

Material	Deposited thickness [nm]	Sputter rate [nm/min]	Ar gas flow [sccm]	DC potential [V]
Cu	5	6.16/6.53	140	600
$Ir_{17}Mn_{83}$	30	5.71/6.00	140	750
$Co_{70}Fe_{30}$	5, 10, 20, 30, 40, 50, 60, 100	3.35/3.44	140	600
Al	5	1.76/2.45	140	600

3.2 Kerr Magnetometry

Kerr magnetometry was selected to magnetically characterize the substrate used for the 2D EB-JPs transport experiments. This method was chosen due to its ability to characterize magnetic thin film samples with in-plane magnetization, whereupon variation of an external magnetic field (H_{ext}), magnetization reversals can be induced. This change in magnitude of the magnetization vector with respect to the H_{ext} applied is called magnetic hysteresis [HS98].

3.2.1 Magneto-optic Kerr Effect

Kerr magnetometry is based on the magneto-optic Kerr effect (MOKE), named after John Kerr, who first reported about this phenomenon [Ker77]. This effect occurs when linearly polarized light changes its intensity and/or rotates its plane of polarization after reflecting off a magnetized surface [HS98, Coe10]. These changes in intensity and polarization plane are proportional to the sample's magnetization. Therefore, MOKE can be used to investigate the magnetic properties of magnetic thin films as a function of an applied H_{ext}. A similar effect, called the Faraday effect, results when light is transmitted rather than reflected. Considering the linearly polarized incident light to be constructed by the superposition of two opposing circularly polarized light waves, the MOKE can be explained

through magnetic circular birefringence (MCB) and magnetic circular dichroism (MCD) [Mer22, Coe10]. The rotation of the polarization plane of the reflected light arises from the magnetic sample having different refractive indices for both helicities of circularly polarized light (MBC). This difference in refractive indices leads to unequal propagation of left (LCP) and right (RCP) circularly polarized light in the sample, thereby creating a phase shift, which ultimately translates into the Kerr rotation. In addition to the difference in propagation velocity, the absorption of LCP and RCP light in magnetic samples also differs according to the respective absorption coefficients (MCD). This uneven absorption leads to elliptical polarization of the reflected light. The Kerr angle will then correspond to the change in the polarization direction between the incident light and the reflected elliptically polarized light (major axis) [Reg22, Coe10].

MCB and MCD, and hence, MOKE, originate from two relevant physical interactions taking place in the magnetized sample, the spin-orbit coupling, and the exchange interaction [Kus11]. The spin-orbit coupling is a relativistic effect caused by a weak magnetic interaction of the electron spin and the orbital motion of this electron, i.e., its angular momentum. On the other hand, in the exchange interaction, the electron spins are coupled to each other. These interactions lead to splitting the electron's atomic energy levels and lifting the degeneracy between spin-up and spin-down states (Pauli principle), respectively. The energy level splitting leads to different allowed electric dipole transition for LCP ($\Delta l = \pm 1$, $\Delta m = -1$, $\Delta s = 0$) and RCP ($\Delta l = \pm 1$, $\Delta m = +1$, $\Delta s = 0$) light, i.e., different absorption rates [Mer22, Kus11].

Macroscopically, the MOKE can be explained via the Lorentz force $\vec{F}_\mathrm{L} = -e\,\vec{v}_e \times \vec{B}$. This force is exerted on the electrons of the magnetic sample, causing them to oscillate and act as Hertzian dipoles after interacting with the incident light. Here, e and $\vec{v}_e$ are the elementary charge and velocity of an electron, and $\vec{B}$ is the magnetic flux density linked to the sample's magnetization $\vec{M}$ [Mer22, HS98]. If the incident linearly polarized light is considered as an electromagnetic wave with an electric field amplitude $\vec{E}$ and the sample is non-magnetic, then the electrons would only oscillate parallel to $\vec{E}$. In this case, the reflected light with an electric field amplitude R would remain in the same plane of polarization. The latter is also mostly true for the magnetized sample, leading to a major component of the reflected electric field amplitude R_N. However, in this case, the electron oscillation is induced perpendicular to the initial electron motion and the magne-

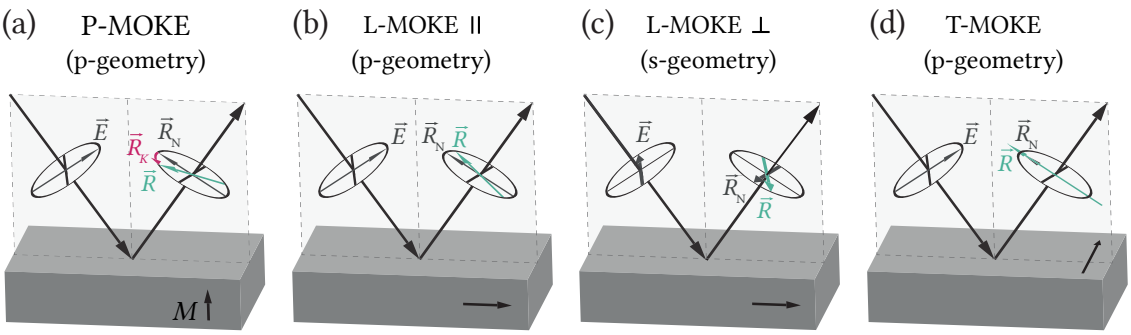

Figure 3.3: Schematic representation of different MOKE geometries. Here, $\vec{E}$ denotes the polarization plane of the incident beam, which can be in a p-geometry (parallel) or s-geometry (perpendicular) with respect to the plane of incidence. R is the rotated polarization plane of reflected light and results from the superposition of the regularly reflected electric field amplitude R_N and the Kerr amplitude R_K. For simplicity, R_K is only depicted for the P-MOKE. Taken from [Reg22].

tization direction of the sample. This electron motion creates part of the reflected light to have a rotated electric field amplitude R_K. Thus, the total reflected light amplitude R will have a polarization plane obtained from the superposition of R_N and R_K. This interaction between light, electrons, and magnetization can then be used to study the rotation in the polarization plane of the light as a function of the magnetization direction. Additionally, this effect can be quantitatively described by means of the dielectric displacement law:

$$\vec{D} = \varepsilon(\vec{E} + iQ\vec{m} \times \vec{E}), \tag{3.1}$$

where $\vec{D}$ is the electric displacement field, ε the dielectric permittivity tensor, $\vec{m}$ the sample's normalized magnetization vector, and Q the material-specific Voigt constant [Huh22, Mer22, HS98]. Here, it can again be noted that in the absence of magnetization, the electric displacement effect will take place exclusively relative to $\vec{E}$ and that in magnetic samples, this displacement will be maximal for configurations in which $\vec{E}$ and $\vec{m}$ are perpendicular to each other. Therefore, it is necessary to consider the different geometrical arrangements with respect to the polarization plane of the light and the direction of magnetization in the sample. These geometries are categorized as polar MOKE (P-MOKE), longitudinal MOKE (L-MOKE), and transversal MOKE (T-MOKE) (cf. Fig. 3.3) and will be briefly explained in the following. Additionally, in each of these geometries, $\vec{E}$

of the incident light can lay within the plane of incidence (p-polarized light) or perpendicular to it (s-polarized light) [Huh22, HS98].

- **P-MOKE:** The polar configuration has an out-of-plane magnetization $\vec{M}$, i.e., the magnetization is oriented perpendicular to the sample surface. Here, both p- and s-polarized light induce the Kerr rotation and display a maximal effect at a normal incidence to the surface [HS98].
- **L-MOKE:** In this geometry, $\vec{M}$ lies parallel to the sample plane and longitudinal to the plane of incidence. For both p- and s-polarized light, a Kerr rotation is induced but in opposite directions. In this case, the Kerr effect is strongest at a grazing angle and disappears at normal incidence [HS98].
- **T-MOKE:** Similarly to L-MOKE, $\vec{M}$ is oriented parallel to the sample plane, however, perpendicular to the plane of incidence. Here, p-polarized light does not induce a Kerr rotation but modifies the intensity of the reflected light. For the case of s-polarized light, the $\vec{E}$ and the $\vec{M}$ are aligned parallel to each other, hence, no Kerr effect can be observed.

3.2.2 Kerr Microscopy

Kerr microscopy was selected to perform a spatially resolved Kerr characterization, since this technique allows visualization of magnetic domains and magnetization processes, such as nuclei formation and domain wall (DW) propagation [HS98]. Therefore, this technique facilitates the creation of a laterally resolved magnetic domain map of the analyzed sample. For the purposes of this project, this magnetic domain map was subsequently correlated with the trajectories of the EB-JPs after being transported over the characterized area (cf. Chapter 5). To this end, an *evico magnetics* high-resolution Kerr microscope was employed (cf. Fig. 3.4). This device uses white light to illuminate the sampled area, which is supplied to the microscope through four pairs of LEDs arranged in a cross pattern, fed through optical fibers. The LEDs arrangement allows to set two planes of incidence perpendicular to each other and the sample surface. Then, by selecting an incidence plane in combination with a polarizer alignment parallel or perpendicular to this plane, the light can be set to be in a predefined p- or s-polarization state, respectively [Mer22]. After the light interacts with the sample, the incoming beam path is separated from the reflected one through a beam

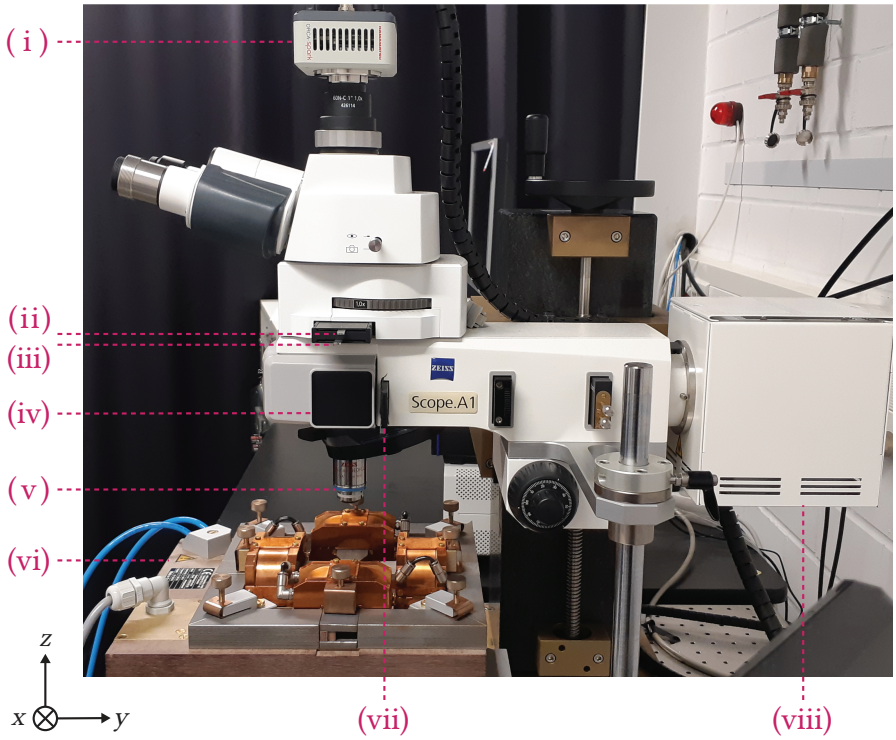

Figure 3.4: Picture of the MOKE microscope employed for the spatially resolved magnetic characterization of the sample with its main components: (i) camera, (ii) analyzer, (iii) compensator, (iv) beam splitter, (v) 50× objective, (vi) in-plane electro-magnets, (vii) polarizer, and (viii) LED lamp from glass fiber array.

splitter so that only the reflected light is analyzed. The reflected light passes then through a compensator made out of birefringent material, which in this case, corrects the elliptical polarization state of the reflected light into a linearly polarized state. Afterward, the reflected light passes through the analyzer (a second polarizer), which filters the portion of the light aligned to the original polarization state (set by the first polarizer). The analyzer is crucial to detect the MOKE signal since only a small part of the reflected light shows this effect [HS98]. Finally, the light is detected by a camera with an integrated charge-coupled device (CCD). The image then captured by the camera contains information related to surface magnetization within the field of view. Here, each pixel is directly related to a point in the sampled area, and the color it displays (typically, within a grayscale) denotes the magnetization state. Opposite colors within the chosen scale represent antiparallel magnetization states. The visibility of the domains depends on

the optimization of the image contrast. This optimization is performed by adjusting the analyzer and compensator in parallel until the image shows enhanced contrast and brightness [HS98].

To induce changes in the magnetization state of the sample, the microscope is equipped with different sets of electromagnets. However, in this project, only the arrangement of electromagnets with in-plane (xy-plane) magnetic fields shown in Fig. 3.4 was employed. These electromagnets allow fine-tuning of their longitudinal external magnetic field, resulting in a controlled change of the sample's magnetization state.

3.3 Particle Transport Setup

The remote-controlled transport of the EB-JPs and the microscope image acquisition for subsequent analysis were achieved through the particle transport setup shown in Fig. 3.5 (a). This setup has two main components, a coil arrangement, which will induce the transport of the EB-JPs over magnetically patterned substrates (cf. Section 2.5.3), and an optical microscope with a high-speed camera capable of recording the fast motion of the particles.

The coil arrangement consists of three pairs of orthogonally-placed, cupper-wired Helmholtz coils, enabling the application of homogenous magnetic fields in each direction of space. By using a computer-controllable power supply, these magnetic fields can be generated as pulses with periodic sequences, where the pulses are set to have a trapezoidal shape [Huh22]. Each pulse has a duration of a sequence's half period $T/2$ and is characterized by a linear rise time Δt_r, a plateau time Δt_p, and a linear fall time Δt_f. Here, Δt_r and Δt_f are constrained according to the time it takes to achieve the desired amplitude of the pulse (H_max), in this case, with a given alternation rate of ca. 4.02×10^3 mT/s [Huh22, Hol15, HKB15]. The pulses are alternated in sign (e.g., from $+H_{\mathrm{max},z}$ to $-H_{\mathrm{max},z}$) and temporally phase-shifted by $\pi/2$, i.e., $T/4$, to induce the motion of the particles (cf. Fig. 2.6). The latter, and further specifications for the magnetic field pulse sequence are set in a custom *LabView* computer program.

For the controlled motion of the EB-JPs, two different magnetic patterns within the underlying substrate were employed, one for the 1D and one for the 2D translation. Both substrates were fabricated prior to this project by means of sputter deposition of an EB thin film system on top of Si(100) substrates

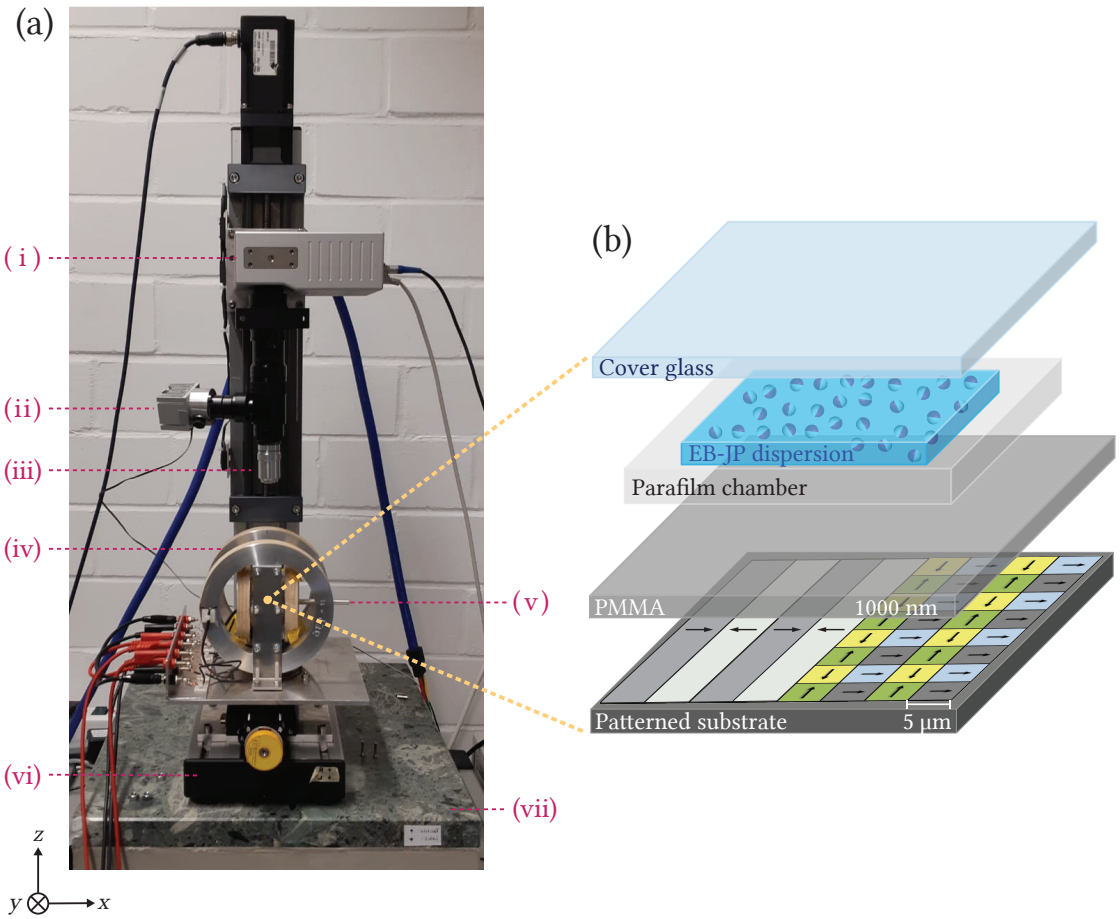

Figure 3.5: (a) Picture of the experimental setup used to perform and record the particle transport experiments in the framework of this project: (i) CCD high-speed camera CR450x2 from *Optronis*, (ii) white LED light, (iii) 100× magnification objective, (iv) Helmholtz coil pairs (x-, y-, and z-direction), (v) sample holder, (vi) adjustable xy table, and (vii) damping structure. (b) Components of the microfluidic chamber. Left (stripe) pattern on the substrate corresponds to the experiments related to the 1D particle transport, whereas the right (checkerboard-like) pattern was used for the 2D motion analysis. Different substrate samples were used for the respective domain patterns. The microfluidic chamber is mounted directly on the sample holder, where, for ease of transport and handling, the substrate covered with the PMMA layer is glued in the central area with double-sided tape. Afterward, the Parafilm® chamber, the EB-JP dispersion and the cover glass are added. Checkerboard-like pattern image taken from [Deu16].

and ion bombardment induced magnetic patterning (IBMP) [EKK04, EKH15, GHH16, Gö19]. The 1D transport of the EB-JPs was realized over a substrate with a magnetic domain stripe pattern with the following EB layer stack system: Cu(5 nm)/$Ir_{17}Mn_{83}$(30 nm)/$Co_{70}Fe_{30}$(10 nm)/Au(10 nm). The stripes were aligned parallel to the y-axis of the setup (cf. Fig. 3.5 (a)), having then the magnetization direction of the domains along the x-axis. Hence, only magnetic fields along the z- and x-direction are needed to transform the MFL and induce 1D transport of JPs (cf. Fig. 2.6). For the case of the 2D transport, a substrate with a checkerboard-like pattern on an EB layer stack of Cu(10 nm)/$Ir_{17}Mn_{83}$(30 nm)/$Co_{70}Fe_{30}$(10 nm)/Si(10 nm) was used. This sample was placed so that the DWs of the domains were aligned to the x and y axes of the particle transport setup. Here, magnetic field pulses were applied in all three directions, with a phase shift $T/4$ only with respect to the z-pulse sequence, i.e., x- and y-pulses are inverted simultaneously.

To perform the particle transport experiments, the particles have to be contained above the magnetically patterned substrate; this is achieved by creating a microfluidic chamber. The chamber is composed of the elements shown in Fig. 3.5 (b). The assembly starts by spin-coating a thin Aldrich® Poly(methylmethacrylate) (PMMA) layer on the surface of the substrate with either the striped (1D) or checkerboard (2D) pattern. This layer increases the distance between the EB-JPs and the substrate, thus decreasing the strength of the MFL felt by the particles, hence preventing particles from irreversibly attaching to the surface. Another reason could be that the PMMA provides more favorable DLVO interactions between substrate and particles (cf. Section 2.5.2), further preventing particle sticking. The PMMA layer was deposited following the procedure described in [Gö19], taking 150 µL of a solution with a PMMA concentration of 70 mg/mL and a spin-coating for 60 s at 3000 rpm with an acceleration ramp of 1000 rpm/s. After curing the substrate for 10 min on a hot plate at 100°C, the PMMA layer is estimated to have a thickness of ca. 1000 nm. The next step in the chamber assembly is to glue the substrate to the center of the sample holder with a double-sided tape and attach a Parafilm® frame with an inner area of ca. 5 mm × 5 mm on top of it. Within this area, the thickness of the Parafilm® (120 µm) will confine the 20 µL EB-JP dispersion with 0.1 wt % sodium dodecyl sulfate (SDS) that will be supplied by means of a microliter pipette. The anionic surfactant SDS is introduced into the system due to its proven enhancement in

the particle's mobility when utilized at low concentrations [RHE21]. The particle dispersion is obtained by manually and gently collecting the EB-JPs from half the surface of the glass substrate (cf. Section 3.1) with the help of a thin coverslip. The harvested particles are then contained in an *Eppendorf* PCR tube ($V = 200$ µL) by allowing two 50 µL droplets of distilled water to (not simultaneously) move across the coverslip before entering the tube. The *Eppendorf* tubes with the EB-JP dispersions are then sealed with Parafilm® and stored until needed. Before pipetting the particle dispersion into the microfluidic chamber, the dispersions are thoroughly mixed by subjecting the *Eppendorf* tube to a Vortex machine for two minutes. The latter minimizes particle agglomeration, which has an unfavorable impact on the transport experiments. The 20 µL EB-JP dispersion with 0.1 wt % SDS are supplied into the chamber as 10 µL EB-JP dispersion, followed by a slow supply of 10 µL of distilled water with 0.2 wt % SDS and using the tip of the microliter pipette to mix the two solutions to avoid bubble formation. Finally, the chamber is sealed with a cover glass to suppress liquid evaporation. Once the microfluidic chamber is fully assembled, the sample holder is placed in the center of the Helmholtz coil arrangement. The coil arrangement, and thus the sample, is on an adjustable table in the xy plane. Therefore, the area of interest on the sample can be aligned with the optical path of the microscope unit, which consists primarily of a high-speed camera, a white LED light, and a magnification lens. The microscope unit can be moved toward the sample by a stepper motor, thus, bringing the area of interest into focus. The stepper motor is also controlled through a custom *LabView* program, which enables the adjustment of the step size of the motor. This step can be set to have a size of approx. 200 µm down to approx. 400 nm. Here, the shortest step ensures a careful approach to the sample at close range and facilitates obtaining a sharp image by adjusting the position to find the focal point. Another factor influencing the sharpness and magnification of the images is the microscope objective used. All transport videos within this project were recorded using a 100× magnification immersion objective. This objective sets two additional requirements: The use of a specially thin cover glass (thickness between 60 µm and 130 µm) and immersion oil. For the latter, a 10 µL droplet of *AppliChem GmbH* (A0699,0100) is placed on the coverslip enclosing the microfluidic chamber before placing the sample holder in position [Huh22]. Ultimately, the particle transport can be recorded by a *Optronis* CCD high-speed camera (CR450x2), which transmits images to a connected PC at a maximum frame

rate of 1000 frames per second. This camera has a maximal sensor resolution of 800 px × 600 px, and a pixel size of 14 µm × 14 µm. To minimize the influence of the external vibrations on the experiments, the particle transport setup is placed on top of a damping structure, consisting of a concrete plate mounted on top of an aluminum profile fixed on air-damped feet.

Manual activation of the video acquisition and magnetic field pulse sequence was required to perform the particle transport experiments. The activation was done after examining the field of view provided by the camera and finding an area with the least amount of particle agglomeration possible. Video acquisition was initiated first, followed immediately by activation of the magnetic field pulse sequence to ensure the collection of as much information as possible.

3.4 Particle Tracking

The particle transport videos were first analyzed by tracking the position of the EB-JPs. To ease the tracking process, a preprocessing of the transport videos was routinely implemented as a step prior to tracking the particles (see Fig. 3.6). This image processing exhibited its advantages for the tracking procedure in the early stages of the analysis and consists of subtracting an "average image" from each frame and afterward filtering the noise to improve the signal-to-noise ratio. The average image is obtained, as its name suggests, by averaging all the frames of the video. Whereas, the noise of each image is reduced by performing a Fast Fourier Transformation (FFT) to the input image, subsequently attenuating the high frequencies of the image with a low-pass filter and finally transforming the image back to its equivalent in the spatial domain by means of an inverse FFT [Huh22]. The resulting images (cf. Fig. 3.6 (b)) display an improved light homogenization over the whole sampled area, which helps to identify the particles away from the center of the sample and, in particular, their cap. Additionally, background subtraction through the average image, which in this case, considers the static particles as part of the background, avoids potential erroneous tracking of the particles. The latter is due to the possibility that the selected particles may pass over visible defects in the sample or near static particles during their trajectory, in which case, the assigned trackers could mistake the originally tracked particle for the defect or static particle and continue tracking one of the latter. It is important to mention that particle transport analyses were performed on the original

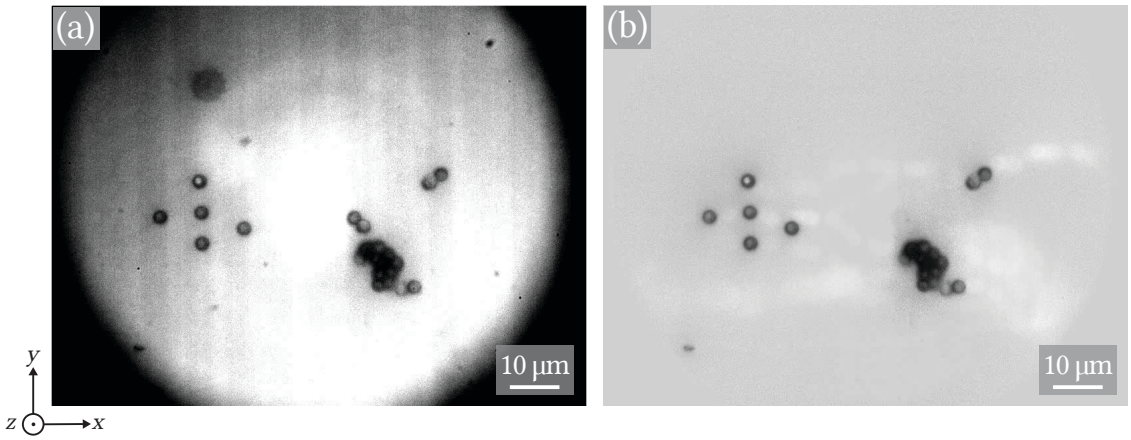

Figure 3.6: Example of a frame from a particle transport video. (a) Shows the original frame, whereas (b) shows the processed image obtained after subtracting the "average frame" from (a) and reducing the noise of the resulting image. The average frame is obtained by averaging all frames in the video. This process leads to homogeneous illumination and removal of non-moving particles and visible defects on the surface of the sample.

video, as well as on a video with only the background subtraction and another with the additional noise reduction to the latter, where no significant deviations were found.

The tracking was achieved by means of a free software called *Video Spot Tracker* (version 8.01) from the Center of Computer Integrated Systems for Microscopy and Manipulation (CISMM) of UNC Chapel Hill [CIS]. This software not only allows for visualization of the particle trajectories in the xy plane by following the x- and y-coordinates of the particle but can also track the orientation of the cap with respect to the xy-plane when the contrast of the EB-JP cap with respect to the transparent template particle is visible (cf. Section 3.1). Both the position of the particle and the orientation of the cap will be essential information for studying the motion dynamics of the magnetic EB-JPs, such as their translational and rotational velocity, respectively. This information will be tracked by the software in each frame of the loaded video. Figure 3.7 shows an image of the *Video Spot Tracker* user interface (UI) with a video frame taken as a reference.

Throughout this project, two tracking modes were used to analyze the transport videos, which will be referred to as "rectangular" and "circular" tracking modes. These names were chosen according to the shape of corresponding track-

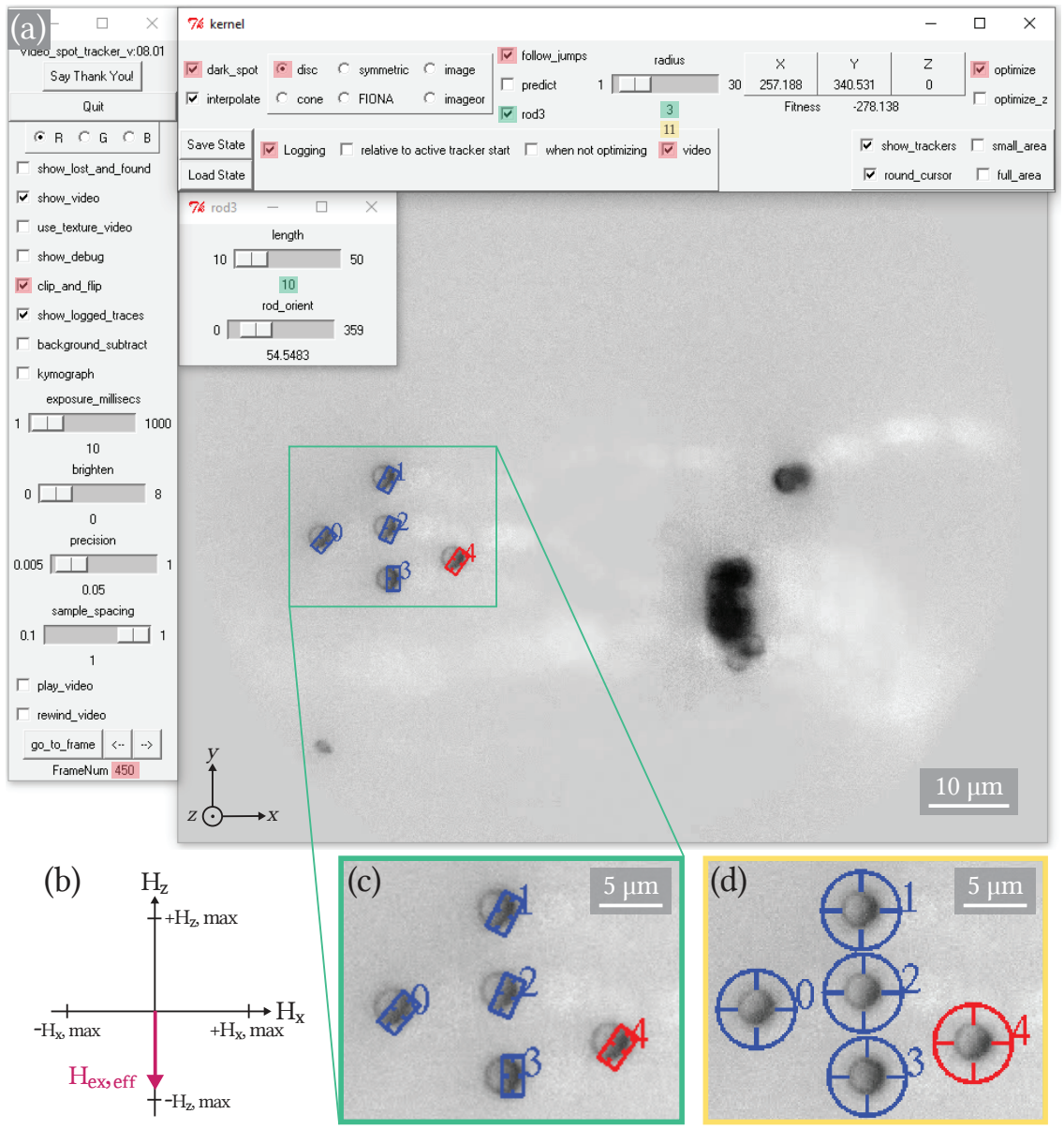

Figure 3.7: (a) Video Spot Tracker (version 8.01) user interface [CIS]. Here, an example image is shown along with the selected settings for the two different tracking modes. The settings used in both tracking modes are marked in red. The initial frame number for tracking (FrameNum), in this case, 450, corresponds to the frame in which the particles have aligned with the MFL after the first pulse of the magnetic field pulse sequence was applied (b). Additional settings for the (c) "rectangular" tracking mode are indicated in green. This mode tracks the x- and y-coordinates of the EB-JP cap and its orientation. (d) Shows an insert image of the particles and their markers in "circular" tracking mode. In this mode, the position in the xy plane of the particle center is followed. The settings selected that are not marked with any color are the default settings when starting the program.

ing markers in each mode (see Fig. 3.7 (c) and (d)). Generally, before proceeding to select the corresponding tracking mode settings, the "flip_in_y" option should be selected in the "clip_and _flip" menu, especially when analyzing a 2D transport video. The latter ensures to analyze the video following the original alignment of the sample in the lab reference frame, since the program inverts the image with respect to the y-axis by default when loading a new video. When working in rectangular tracking mode, it is necessary to determine the initial frame for the tracking process. This frame corresponds to the first alignment of the EB-JPs with the MFL triggered by the first pulse of the magnetic field pulse sequence, typically along the negative z-axis (cf. Fig. 3.7 (b)). In this frame, the particles will ideally be aligned so that maximum visibility of the dark-contrasted magnetic cap is ensured. It was found relevant to display this frame in the UI before selecting other settings to ensure the proper assignment of the rectangular tracking markers. Although the latter does not influence the position of the tags in circular tracking mode, it was kept as part of the procedure for consistency. The following setting to activate is "dark_spot". This setting is chosen due to the darker appearance of the particles and, in particular, the magnetic cap compared to the lighter background. Then, the option "disc" is selected with a radius $r_r = 3$ and $r_c = 11$ for rectangular and circular modes, respectively. This will give the tracking markers the shape shown in Fig. 3.7 (d), which will require additional activation of "rod3" with $length = 11$ to obtain the rectangular shape necessary to track the cap (Fig. 3.7 (c)). The corresponding markers will then be assigned manually to the EB-JPs under study by clicking on top of them; this excludes dimers, agglomerates, and static particles. When selecting "optimize", the program will confirm and automatically correct the position of the markers if necessary. Another important setting is "follow_jumps". This option ensures the correct tracking of the particles through their characteristic jumping-like motion caused by the alternating MFL. After the different settings have been selected, a file is created to store the information; this is done by clicking "Logging" and naming the file. The tracking process is then started by selecting "play_video". The generated file will consist of the x- and y-coordinates of the particle/cap with respect to the assigned tracker ID per frame number. If the tracking is done in rectangular mode, the file will also show the orientation angle of each cap per video frame.

It should be noted that the Video Spot Tracker software has the limitation that only particles in the selected initial frame will be tracked unless manually added

afterward. Therefore, if particles appear in the field of view in subsequent instances, it would be necessary to perform additional tracking. The latter is also required if one of the particles in the initial frame leaves the field of view, as this will cause the program to stop tracking. Discarding these additional traceable particles/steps may represent a considerable loss in statistical terms (cf. Section 4.3).

1D Transport: Influence of the Ferromagnetic Layer Thickness

4

In this chapter, the results of the experiments related to the one-dimensional (1D) directed transport of Exchange-Bias capped Janus particles (EB-JP) over a parallel-stripe domain pattern via dynamic transformation of magnetic field landscapes (MFL) are presented. Within the framework of this project the motion dynamics of 3 µm sized EB-JPs with different thicknesses of the cap's ferromagnetic layer (t_F) were investigated. Previous investigations on submicron-sized disks [CKA99, WGP16, WRP19] and nanometer-sized JP [SKS12, SMK12, Reg22] have shown that different magnetization textures can be induced within the disk or cap depending on the ferromagnetic layer thickness. Therefore, EB-JPs were fabricated following the methodology presented in Section 3.1, with t_F varied between 5 nm and 100 nm to trigger the formation of different magnetization states within the EB-JPs' caps (cf. Section 2.4.1). It is hypothesized that the magnetization state, i.e., the magnetic properties of the EB-JPs will influence their motion behavior in a 1D transport experiment, thus potentially allowing for an identification of the EB-JP cap magnetization state solely from observing its movement pattern. For this analysis, a parallel-stripe domain pattern fabricated by means of ion bombardment induced magnetic patterning (IBMP) was selected [GEU18]. This pattern was chosen in combination with a stripe width of 5 µm due to its proven effectiveness in generating the MFL required to induce transport of particles with diameters on the order of a few microns [Hol15, EKH15, HRT21, RHE21]. The stripes have opposite magnetization direction with respect to adjacent stripes along the periodicity axis, defined as head-to-head (hh)/tail-to-tail (tt) magnetization configuration. This configuration maximizes the strength of the magnetic stray fields emerging at the domain walls (DW) [HZK13]. In general, this system requires only weak external magnetic field pulses to induce particle transport [HKB15, HRT21], which is relevant in order not to destabilize the EB-JPs caps from their remanent magnetic state.

In addition to having a specific magnetic state, magnetic Janus particles possess the ability to physically rotate upon application of an external magnetic field due to their asymmetric structural composition. This distinguishes their motion behavior from symmetric magnetic particles, e.g., superparamagnetic beads, that typically do not exhibit rotational movements. The ability to rotate arises from the intrinsic magnetic state of the JP, which gives its cap a magnetization direction that can be used to control the orientation of the particle and, thus, rotate it. Therefore, another relevant aspect of this project was the determination of the rotational velocity of the EB-JPs.

Upon initial analysis of the particle transport recordings, an asymmetry in the stripe domains' width in the sample used for the transport experiments became evident. This asymmetry was subsequently confirmed by characterizing the sample with Kerr microscopy, resulting in average stripe widths of ca. 6.3 µm and 3.7 µm (cf. Appendix A.2), while maintaining the (hh)/(tt) magnetization configuration and periodicity of ca. 10 µm. Therefore, working with this sample implied modifying the analysis method usually used in the research group, since it is necessary to distinguish between the particle transport performed over the two different stripes. Nevertheless, this also gave rise to the possibility of additionally studying EB-JP transport dynamics with respect to the stripe domain width.

In the following section, a description of the evaluation process developed to determined the translation and rotation velocities of the EB-JPs as a function of the width of the two stripes will be introduced (Section 4.1). Subsequently, a qualitative analysis of the EB-JPs individual and agglomerate motion as a function of t_F will be presented in Section 4.2. Finally, the obtained translational and rotational EB-JPs velocities as a function of t_F, the main focus in this chapter, will be discussed in Section 4.3.

All particle transport experiments regarding the 1D transport of EB-JPs were recorded at 250 fps using a 100× magnification objective, with strength of the externally applied magnetic field pulses of $H_{\max,z/x} \cdot \mu_0 = 3$ mT alternating every $T/4 = 1$ s. It should be noted that the scale factor used to convert the dimensions from the captured images to the physical system was obtained from the analysis of the 2D motion of the EB-JPs presented in the following Chapter (5). However, since both studies were performed under similar conditions (similar microfluidic chamber and same amplification objective for the particle transport setup), they are considered to represent the same system. Additionally, the scaling factor leads

to similar values for the stripes widths determined from the sample characterization.

4.1 Evaluation Process

To determine the translation and rotation velocities of the EB-JPs, a systematic procedure to evaluate the particle transport experiments needed to be established. In particular, to correctly classify the information obtained from the tracking procedure (cf. Section 3.4). Information that later on will be categorized into transport steps, according to the principle of the particle transport mechanism (cf. Section 2.5.3). For this purpose, tracking data corresponding to a transport video of EB-JPs with a ferromagnetic layer thickness $t_F = 10$ nm will be used as an example. The first frame of this transport video is shown in Fig. 3.6, while Fig. 3.7 shows the ID assignment to the transported particles. Following the methodology described in Section 3.4, the particles were tracked twice, once with a circular tracker and a second time with a rectangular one. The resulting data is plotted as presented in Fig. 4.1, except for the data points corresponding to the first $T/4$, which are removed from the evaluation, since they do not contribute to the velocity determination. Here, (a) shows the displacement along the x-axis for the five tracked particles for the two tracking modes. The distance traveled obtained from the rectangular tracking is plotted with an offset of 5 µm to differentiate it from the circular tracking data. However, since the particles 1, 2, and 3 are aligned and move parallel with respect to the x-axis (cf. Fig. 3.7), it is not possible to distinguish them without introducing additional offsets. Furthermore, Fig. 4.1 (b) displays the angular change of the EB-JP's cap relative to the xy-plane. This information can only be obtained with the rectangular tracker. Additionally, the applied magnetic field sequence is plotted in (c), to correlate the information from (a) and (b) with the corresponding change of the external magnetic field (H_z or H_x) (cf. Section 2.5.3).

To ease the description of the data in the following section, where the different steps are classified, the analysis is focused on the data highlighted in graphs Fig. 4.1 (a) and (b) for the particles 1 and 4.

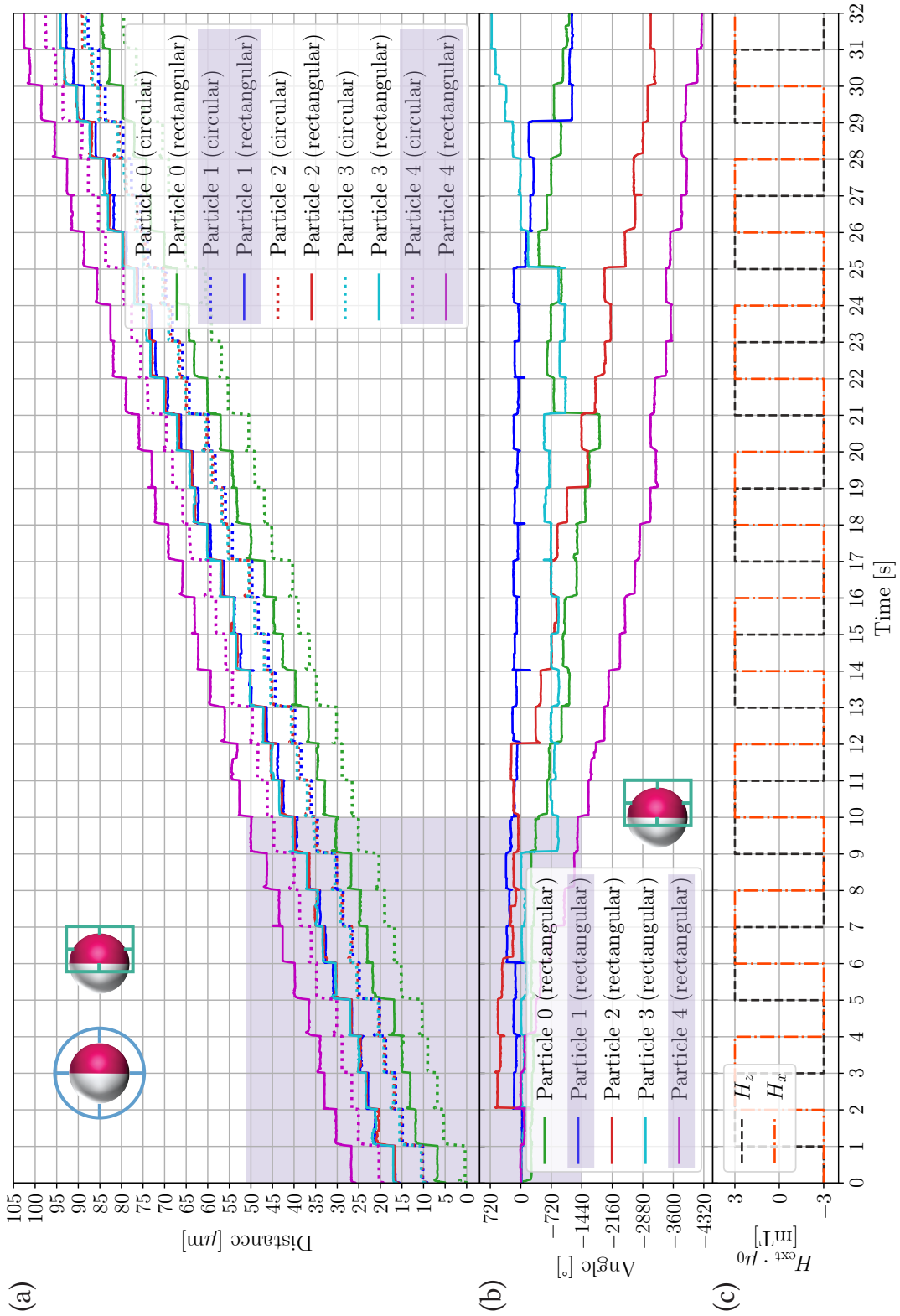

Figure 4.1: Particle transport tracking data of five EB-JPs with t_F = 10 nm. (a) Displacement along the x-axis. (b) Angular change in cap orientation. (c) Applied magnetic field sequence. For more information, see the text.

4.1.1 Transport Step Classification

Upon analysis of the tracking data, four different types of induced motion steps could be identified. These steps were determined from the combination of the translational motion induced by the particle transport mechanism, giving rise to the so-called small and large steps (cf. Section 2.5.3), and from the width asymmetry of the stripe domain pattern, identified as wide and thin stripes.

Figure 4.2 (a) shows the schematic representation of two distinct rotations and four distinct translational movements that EB-JPs where observed to perform while being transported over the asymmetric stripe domain pattern with hh and tt configuration. The rotation depicted on the left side (y-rotation) can be described as a rotation in the xz-plane, which takes place simultaneously as the EB-JP performs a large step [HRT21], crossing over the wide or the thin stripe domain, or in other words, crossing from a side of a tt-domain wall (DW) to the next hh-DW or vise versa. This rotation cannot be followed unambiguously by the tracking system, as the tracker loses visibility of the contrast between the opaque EB-JP cap and the transparent template particle, represented here as the intermediate step of the rotation, where the cap is completely oriented downward with respect to the z-axis. However, the rotation illustrated on the right side (z-rotation) takes place in the xy-plane and can be followed when the rectangular tracker is assigned to the EB-JP cap. Similar to the y-rotation, the z-rotation occurs in parallel to a translation of the EB-JP, although, in this case, with respect to the small step [HRT21], which corresponds to the crossing from either wide-stripe to thin-stripe or vice versa. The small step can also be explained as the transition from one side of a tt- or hh-DW to the other side of the same DW. By additionally considering the stripe width, the steps can then be classified as shown in Fig. 4.2 (f) in wide stripe-large step, thin stripe-large step, wide stripe-small step, and thin stripe-small step.

The need for this classification procedure for further evaluation became apparent after a close look at the tracking data, e.g., in Fig. 4.2 (b). Once again, the data obtained with the rectangular and the circular marker is shown with an offset of 5 µm. Focusing first on the trajectory traversed by the particle 1 tracked with the circular marker, different segments with a behavior similar to a step function can be observed. This stepwise motion is an intrinsic property of the particle transport mechanism (cf. Section 2.6), where the applied external magnetic field (here, H_z or H_x) that induces the particle movement is periodically alternated, as shown

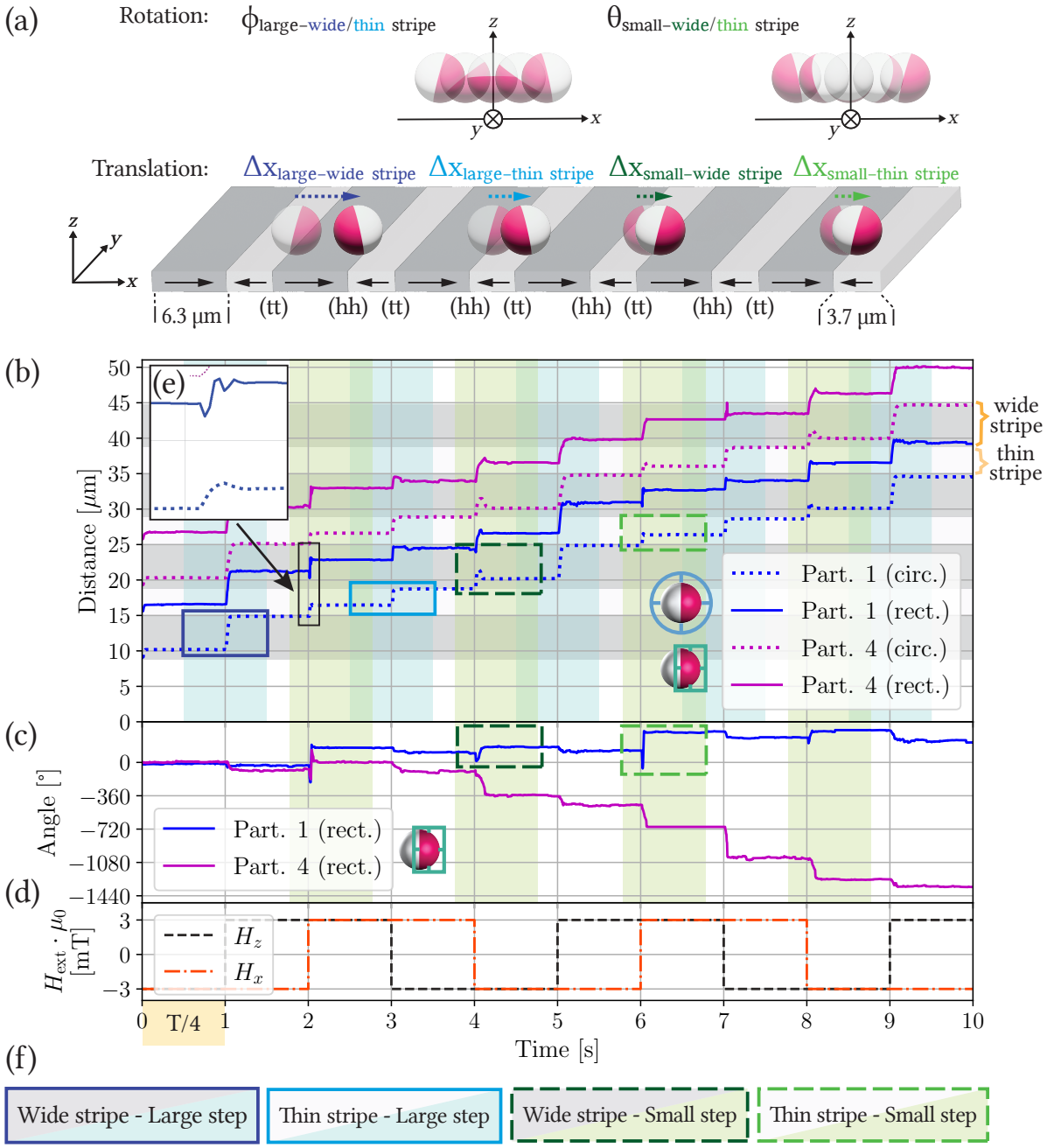

Figure 4.2: Visualization of the particle transport step classification for EB-JPs over a hh/tt stripe domain pattern with asymmetric width. (a) Schematic depiction of the possible two rotations and four translation steps of the EB-JPs over the stripe pattern. (b) Displacement along the x-axis and (c) angular change of particles 1 and 4 from the data highlighted in Fig. 4.1 with the corresponding (d) applied magnetic field sequence. (e) Close-up of a small translation step for comparison of data obtained with a rectangular vs. circular tracker. (f) Step categories with color association to the highlighted areas within (b) and (c).

in Fig. 4.2 (d). Here, the frequency of the alternation is defined as a quarter of a period T, with $T/4 = 1$ s. Thus, one transport step is induced every second. It is well established that, when working with a hh/tt stripe pattern configuration, a reversal of H_z induces a large translational motion step [HKB15], e.g., at times $t = 1$ s, 3 s, 5 s, etc. This is followed by a small step induced by the subsequent sign inversion of H_x, here, at times $t = 2$ s, 4 s, 6 s, etc. However, comparing only large steps, it was noted that steps at times $t = 1$ s, 5 s, 9 s show a distance traveled of ca. 5 µm, whereas, large steps at times $t = 3$ s, 7 s show a smaller distance of ca. 2.5 µm. Contrary to the latter, the EB-JPs traversed a similar distance of ca. 1.5 µm in all the small steps. This asymmetry regarding the large steps was observed in all tracking data sets and for all particles, evidencing a stripe width asymmetry in the sample used for the 1D particle transport experiments and the need for proper motion step processing to ensure correct statistical analysis of particle transport velocities.

To determine the steady-state translational and rotational velocities of the EB-JPs acquired during an induced motion event, the data sets were cropped according to the step to be evaluated. The translational velocities are hereby derived solely from the large steps. For each of these steps 250 data points were selected from the initial data set, with the step being at the center of these data points, as shown in Fig. 4.2 (b) by the blue highlighted areas. The size of the cropped data section for each individual step, i.e., 250 data points, is equivalent to the number of video frames within which one motion step of the EB-JP could be recorded. In this case, the transport experiments were recorded at 250 fps with $T/4 = 1$ s, resulting in 250 frames per step. On the other hand, the rotational velocities are determined solely from the small steps. However, here, the data points to be analyzed are selected as such that the step is located at 50 points (20% of the cropped data per step) from the beginning of the selection range, as marked in Fig. 4.2 (b) with green color. In addition to the vertically highlighted areas, the horizontal lines in the same figure indicate the steps corresponding to the wide stripes (dark gray) and the thin stripes (white areas between the dark gray). The overlap of the horizontally and vertically marked sections indicates the selected data for the corresponding step category, as shown in Fig. 4.2 (f). It should be noted that since for the small steps the EB-JP moves from one stripe to another (cf. Fig. 4.2 (a)), the correlation of the small steps with a wide or thin stripe was made by convention. Here, the small steps were assigned to the stripe type on which the EB-JP finished

Table 4.1: Overview of the EB-JP motion step categories defined in the framework of the 1D particle transport analysis.

Step category	Depiction in Fig. 4.2 (a)	Tracking mode needed	Selected data sections	Used to determine
Wide stripe-large step	from tt-DW to hh-DW	circular	overlap of blue with dark gray	translational velocity
Thin stripe-large step	from hh-DW to tt-DW	circular	overlap of blue with white	translational velocity
Wide stripe-small step	from one side of a tt-DW to the other	circular and rectangular	overlap of green with dark gray	rotational velocity
Thin stripe-small step	from one side of a hh-DW to the other	circular and rectangular	overlap of green with white	rotational velocity

its motion. This correlation was then transferred to the tracking data corresponding to the angular change of the EB-JP cap orientation (cf. Fig. 4.2 (c)) in order to determine the data sections used for the evaluation of the rotational velocities.

The rectangular tracking marker used for the identification of the EB-JP cap orientation provides the translational displacement as well (cf. Fig. 4.2 (b)). The corresponding trajectories, however, display more noise compared to the same trajectories obtained with the circular marker. The latter can be seen in Fig. 4.2 (e), which shows a magnified view of a small step. Here, the appearance of a small peak in the small step tracked with the circular marker is particularly relevant, as it was used to establish the time window in which the rotational step takes place (cf. Section 4.1.3).

An overview of the EB-JP motion step categories and the relevant information regarding them is presented in Table 4.1. Once the tracking data was correctly classified, it was analyzed as explained in Sections 4.1.2 and 4.1.3 to determine the corresponding steady-state translational and rotational velocities, respectively.

4.1.2 Translational Velocity Determination

The translational velocities of the EB-JPs were determined following the same methodology used in previous scientific studies in the research group [RHE21, HRT21, Huh22]. First, the individual translational steps were plotted within the same category as shown in Fig. 4.3 (a) for the steps corresponding to wide stripe domains, and (b) to thin stripe domains. This allows to visualize the difference in transport distances originating from the asymmetry of the magnetic stripe domain in the underlying substrate. Here, only every second data point is shown for better distinction. A Gaussian error function is then fitted to each individual step, shown in Fig. 4.3 (a) and (b) as color-matched lines. This function was chosen since it has been previously used to resemble the stepwise motion behavior of magnetic particles within the investigated transport system [RHE21, HRT21, Huh22]. Additionally, this approach can be used to filter out noisy steps or steps that were not tracked correctly by defining a threshold value for the fitting error. Therefore, only fit functions that consistently represent tracking data of a clear stepwise movement are considered for determining the velocities. Figures 4.3 (a) and (b) only show steps and fit functions that have satisfied this condition. This is the reason why particle 1 in (b) has a transport step less than particle 4. Once the steps have been filtered, the time derivative of each individual fit function is calculated, leading to distributions of velocities for each step as shown in Fig. 4.3 (c) and (d). The colors of the resulting time-dependent velocity curves match their corresponding transport step in (a) or (b). Here, the curves are plotted with increasing displacement along the time axis to improve their visual distinction. Then, the maximum value of each curve, marked with a circle or a triangle, is taken as the steady-state velocity of the EB-JP for the corresponding step. In the framework of this project, this steady-state velocity is used as a metric for comparing the translational motion speeds of the investigated EB-JPs. The steady-state velocity takes the main forces governing the motion of the particles, the drag force and the magnetic force (cf. Section 2.5.2), into account.

Focusing now on Fig. 4.3 (c) and (d), it can be seen that translational velocities for both particles (1 and 4) corresponding to transport steps above thin stripes (d) are on average higher than those obtained from transport steps over wide stripes (c). As a possible physical explanation, this is attributed to magnetic stray fields being confined in a smaller space for thinner stripe domains, therefore leading to steeper field gradients and, according to Eq. 2.28, a larger magnetic

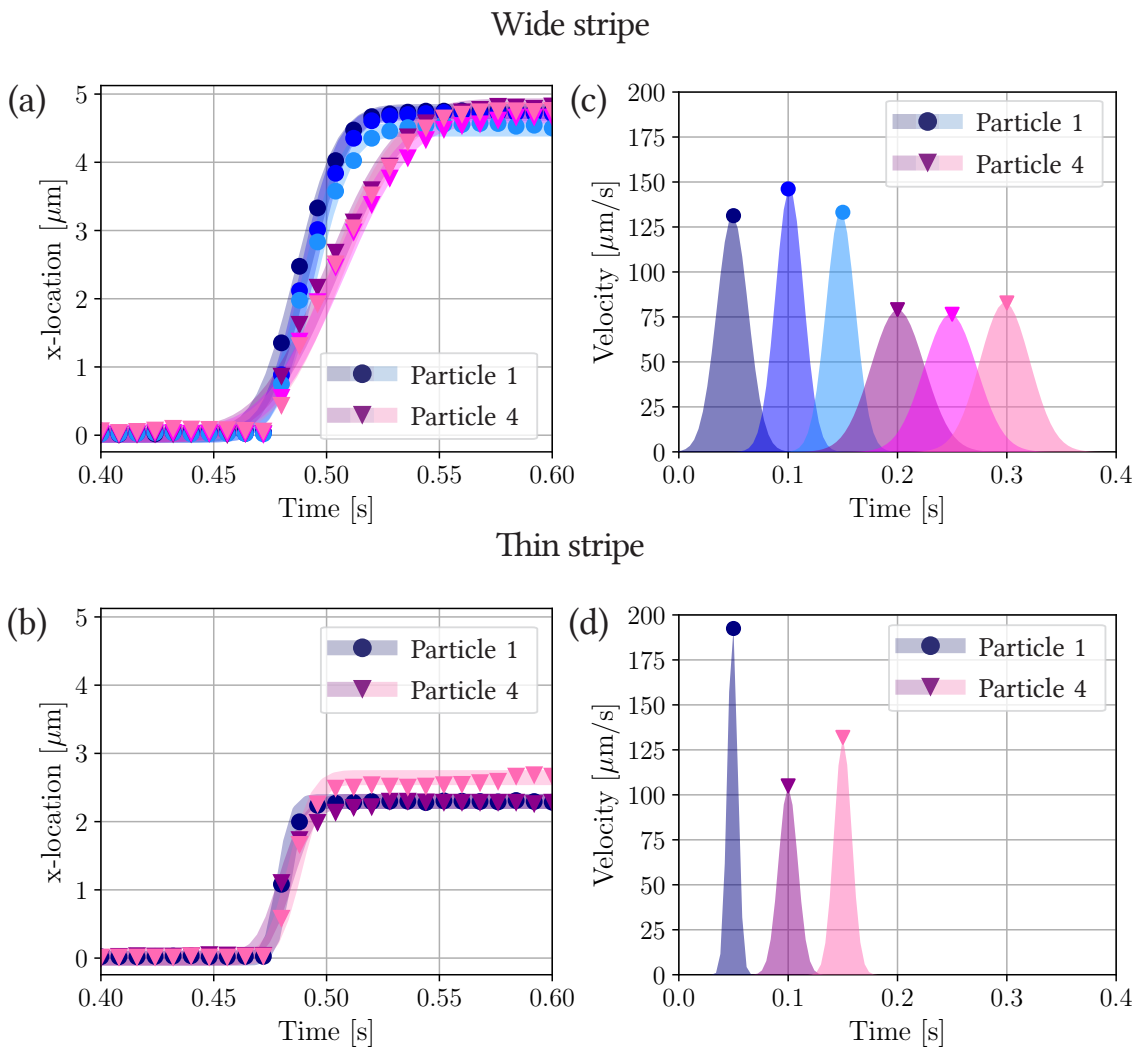

Figure 4.3: Evaluation of single transport steps used to determine translational velocities of EB-JP. (a) and (b) Data points corresponding to large steps extracted from the trajectories shown in Fig. 4.2 (a), for wide and thin stripe, respectively. Each step was fitted by a Gaussian error function, shown as a color-matched line. Only transport steps with a sufficiently low fit error are shown. (c) and (d) Translational velocities determined from the steps shown in (a) and (b). The velocities were calculated from the time derivatives of the fitting curves, resulting in time-dependent velocity curves. These curves are arbitrarily placed along the time-axis to ease the distinction between the individual curves. Here, the maximum of each velocity curve, marked with a circle or triangle, represents the estimated steady-state velocity of the EB-JP during the corresponding transport step.

force acting on the particles. This trend was also observed in studies on superparamagnetic beads [Huh22], where the beads were transported above a parallel stripe domain pattern with a continuously increasing stripe width. Although it has been shown that a critical pulse time length exists that marks the transition between linear and non-linear transport behavior [Huh22], such an influence on the velocity difference with respect to the bandwidth can be excluded. This is evidenced by the transport steps occurring in less than 0.1 seconds for all cases, as can be seen in Fig. 4.3 (a) and (b), which allows sufficient time for the particles to finish their motion and attain a resting position before the next transport step is induced by a change in the external magnetic field. Additionally, the ratio between the velocities of the particles 1 and 4 stays roughly the same for small and wide stripes. The latter underlines the necessity to perform several transport experiments to obtain an accurate representation of the average velocity for EB-JPs with the same t_F.

4.1.3 Rotational Velocity Determination

For a systematic and reliable evaluation of rotational velocities of the EB-JPs, a relationship between the translational and rotational data of small transport steps was established. For this purpose, as in the previous section, the individual translational steps were separated and plotted within the same category. Here, Fig. 4.4 (a) shows the translational steps classified as wide stripe-small step and (c) as thin stripe-small step. The corresponding rotational steps were plotted below in the same color, as shown in Fig. 4.4 (b) and (d), respectively. For clearer visualization, only one out of every 10 data points is shown with a line connecting them. Analyzing first the translational steps, a noticeable peak in the trajectory can be observed, in particular in the steps of Fig. 4.4 (a). This peak is used as a reference for determining the time window in which the transport step takes place. By analyzing a small transport step frame-by-frame, it has been observed that the EB-JP first passes through the final resting position and then returns to it (cf. Fig. 4.6). Furthermore, it has been identified that the time interval in which the EB-JP changes its angular orientation corresponds to the time between the beginning and the end of the peak in the translational data (cf. Fig. 4.4 (b)). Therefore, each translational step paired with its corresponding rotational step was analyzed individually. To illustrate the latter, Fig. 4.4 (e) shows a zoomed interval of a trans-

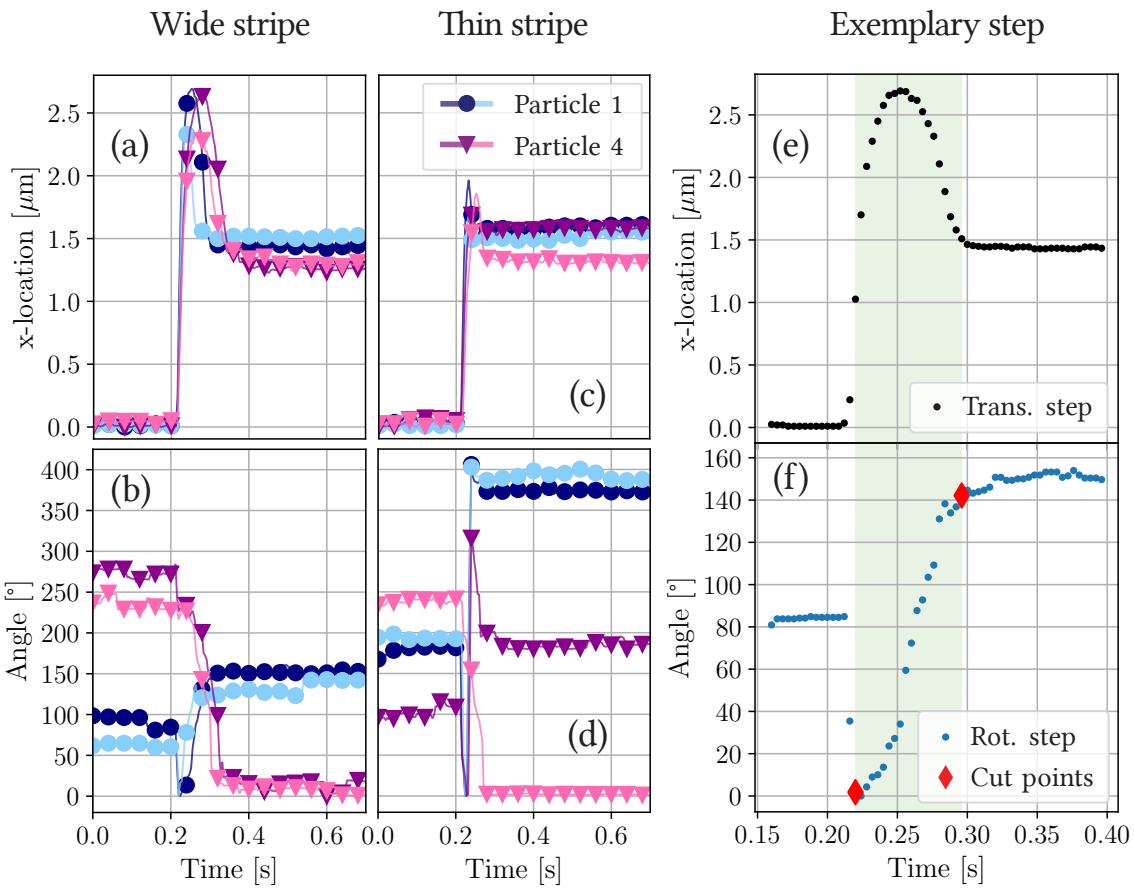

Figure 4.4: Evaluation of the transport steps used to determine the rotational velocities. Transport steps (data points) previously defined as (a) wide stripe-small steps and (c) thin stripe-small steps extracted from the trajectories shown in Fig. 4.2 (a). (b) and (d) Angular change for the corresponding transport steps shown in (a) and (c). Here, only every 10th data point is shown for a clearer view of the data. (e) Close-up of a transport step in (a) with (f) its respective rotational step, i.e., angular change. Here, all data points are shown. The area marked in green highlights the time window in which the transport step takes place. Diamond-shaped indicators mark the start and end of the time window and the cutting points for the subsequent fitting procedure.

lational step from (a), and (f) its equivalent rotational step from (b). Here, all data points are shown and the time window in which the motion event took place can be clearly defined. However, it had to be taken into account, as in this case, that upon beginning of translational movement the rotational orientation of the EB-JP cap is often times drastically adjusted by the tracking software. This mea-

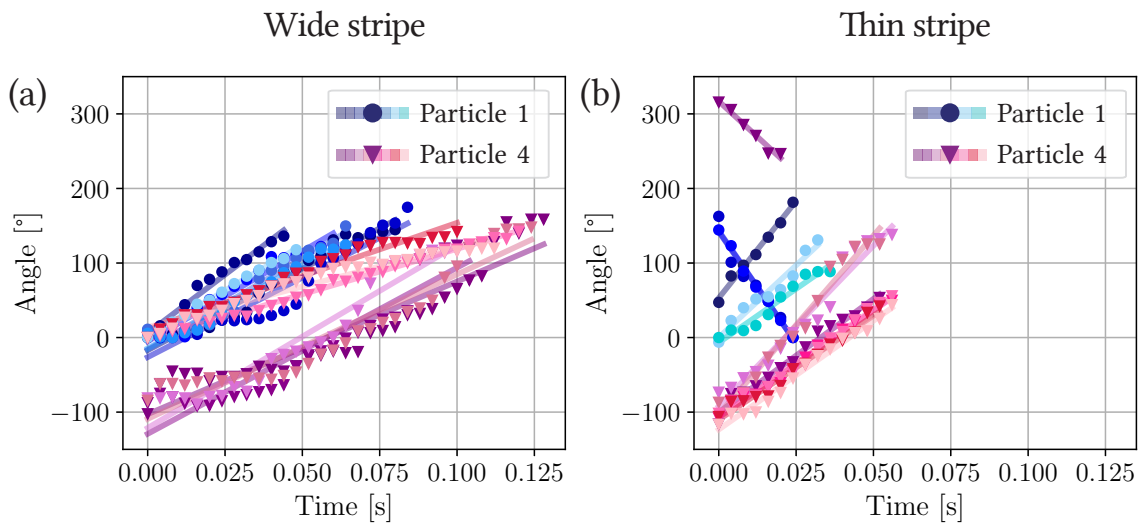

Figure 4.5: Rotational steps (data points) extracted from the trajectories shown in Fig. 4.1 (b) for particles 1 and 4, for (a) wide stripe and (b) thin stripe. Each step was fitted with a linear function. The rotational velocities were calculated from the slope of the linear fits. Only rotational steps with a significant number of data points and sufficient agreement of the corresponding fit function are shown.

surement artifact can be exemplary seen in Fig. 4.4 (f) by the jump of the tracked angle from ca. 80° to ca. 0° within a few milliseconds, coinciding with the start of the transport step visible in Fig. 4.4 (e). The data points containing this artificial jump of the orientation angle should be excluded from the analysis, therefore, the data points relevant for rotational velocity determination were selected manually. The initial and final data points of the resulting area of interest for the rotational step are marked with red diamonds and the relevant area is highlighted in green. Although this step in the evaluation process is time-consuming, the noise in the tracking data from EB-JPs with greater t_F imposed the need to carry out the analysis in a handpicked fashion. Nevertheless, an alternative approach to determine the relevant data for the rotational steps is presented in Appendix A.3. The latter requires, however, less noisy tracking data, which could be obtained by recording the images of the transport experiments with higher resolution and more homogeneous illumination or by using other tracking methods.

Once the rotation steps have been cropped according to the defined area of interest, they are filtered by their duration, i.e., steps consisting of a number of data points below a given threshold are discarded. This was implemented because it

was observed that the EB-JPs require a certain minimum amount of time to perform the steps. Therefore, rotational steps with only a few tracking data points do not represent a correctly tracked EB-JP cap orientation. Typically these steps are characterized by not showing a distinct peak in the translational tracking data, accompanied by unrealistic angular changes for rotation, e.g., the steps of the particle 1 and the dark step of particle 4 shown in Fig. 4.4 (d). Afterward, a linear function is fitted to each individual rotational step and the slope of this linear fit is defined as the steady-state rotational velocity of the EB-JP for the corresponding step. As in the analysis for the translational velocity (Section 4.1.2), fit functions that showed a fit error larger than a selected threshold value were filtered out, and those steps were not taken into account for the evaluation. The resulting rotational steps with their corresponding fit functions are shown in Fig. 4.5 (a) for the wide stripe category, and in (b) for the thin stripe category. Here, the rotational steps corresponding to the particles 1 and 4 are presented for the entire trajectories shown in Fig. 4.1 to improve the visualization of the trends. Comparing Fig. 4.5 (a) and (b), there is a clear difference between the average time taken by EB-JPs to perform the rotational step corresponding to the two different categories of small steps (wide stripe and thin stripe). Here, according to the previously established definition for the small step category (cf. Section 4.1.1), EB-JPs take longer to perform steps when crossing the DW from the thin stripe side toward the wide stripe than vice versa. The average steady-state rotational velocity for each EB-JP is then calculated taking the absolute value of the rotational velocities calculated for the different steps. Therefore, the direction of rotation is not taken into account, e.g., in the rotational step in Fig. 4.5 (b) located at the upper left corner, which gives a negative velocity.

4.2 Influence of t_F on the Motion Patterns of Individual JPs and Agglomerates

As mentioned previously, as part of the investigation on the 1D motion of EB-JPs with different t_F on a substrate with hh/tt parallel stripe domain pattern, the motion sequences of the EB-JPs were analyzed frame-by-frame to qualitatively characterize their motion dynamics. For illustration, Fig. 4.6 (a)-(d) shows microscope snapshots of individual EB-JPs with t_F = 5 nm, 20 nm, 40 nm and 60 nm, respec-

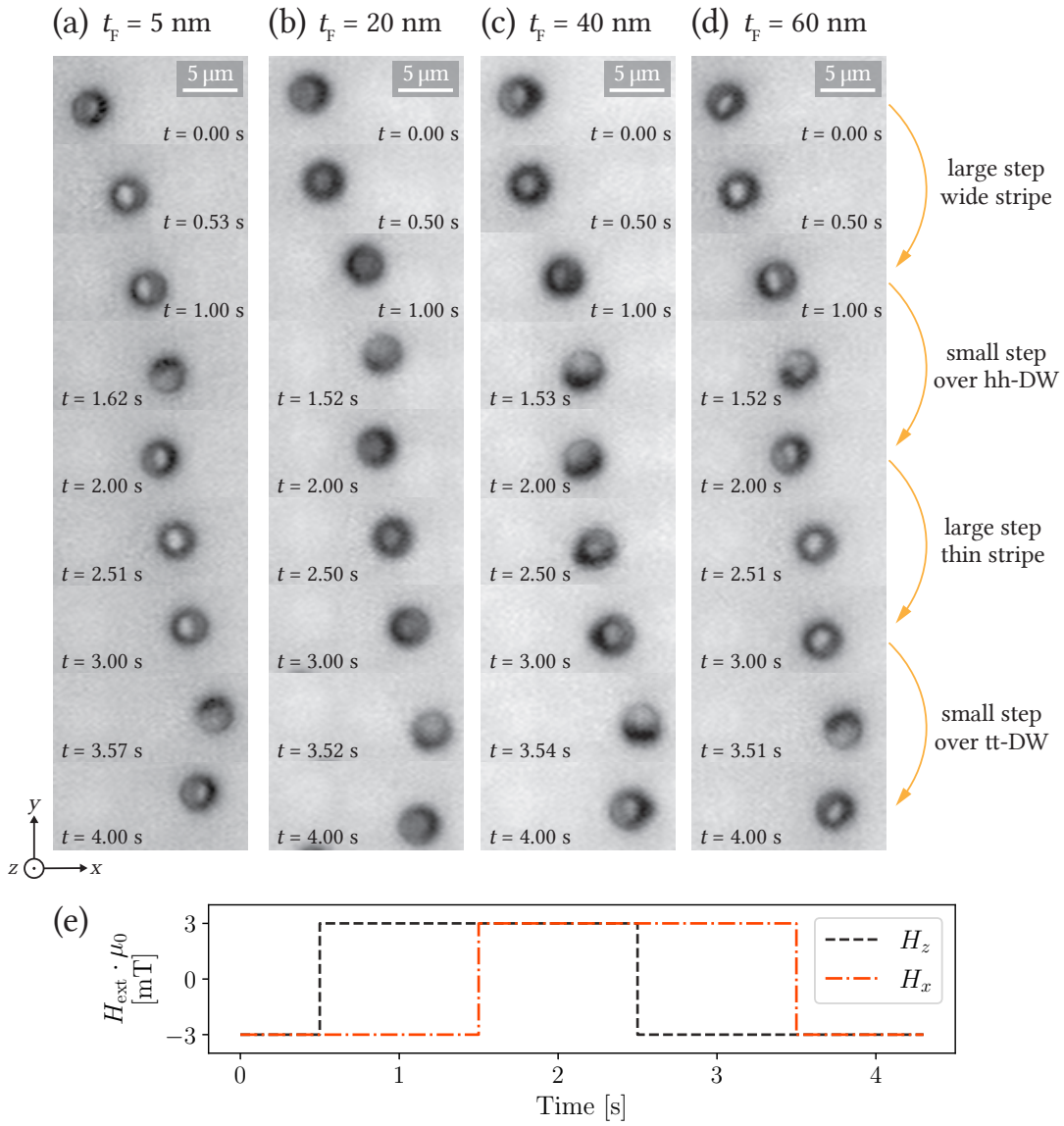

Figure 4.6: Visualization of the movement of individual EB-JPs on a substrate with hh/tt parallel stripe domain pattern. (a)-(d) Microscope snapshots of exemplary EB-JPs with t_F = 5 nm, 20 nm, 40 nm and 60 nm, respectively, at different times during the experiment. The indicated time on each image corresponds to a time within the applied magnetic field sequence shown in (e).

tively, at different times throughout the experiment. Here, motion sequences for four transport steps are presented. Although there is no visual reference to the underlying stripe-patterned substrate, the positions of the EB-JPs with respect

to the stripe pattern can be deduced from the externally applied magnetic field pulses $H_{\mathrm{max,z/x}} \cdot \mu_0$, which modify the MFL of the substrate and, thus, the potential energy of the EB-JP $U_{\mathrm{P}}(x, z)$ [HRT21]. All trajectories shown in Fig. 4.6 start with a snapshot corresponding to the time $t = 0$ s of the applied magnetic field sequence shown in Fig. 4.6 (d). At this time the EB-JP caps are located on the right of a tt-DW due to $H_{\mathrm{max,z}} \cdot \mu_0 = -3$ mT and $H_{\mathrm{max,x}} \cdot \mu_0 = -3$ mT [HRT21]. In resume, for all EB-JPs in Fig. 4.6 (a)-(d) at $t = 0$ s the cap, which can be distinguished by its darker contrast from the transparent template particle, is on the right side. In some cases, the cap exhibits a light spot roughly located at its center, which is attributed to light reflection at the aluminum capping layer of the cap. From this initial position the EB-JPs perform a large step above the wide stripe, triggered at $t = 0.5$ s, with their final position ($t = 1$ s) on the left side of a hh-DW and the cap located on the particle's left side. Then, the EB-JPs exhibit a small step crossing the hh-DW ($t = 1.5$ s), followed by a large step above a thin stripe (from hh-DW to tt-DW at $t = 2.5$ s), to finally take another small step over a tt-DW ($t = 3.5$ s). These four transport steps illustrate a full cycle of the externally applied magnetic field pulse sequence. Here, the stripe type can be distinguished by the length of the large steps, i.e., the EB-JPs are displaced by greater length from $t = 0$ s to $t = 1$ s than from $t = 2$ s to $t = 3$ s. Furthermore, these snapshots illustrate the traceable rotation of the EB-JPs that takes place simultaneously while the particles perform the small steps (around $t = 1.5$ s and $t = 3.5$ s) together with the overshoot used to determine the time window for the rotational step described in Section 4.1.3. From the intermediate stages of the large steps (around $t = 0.5$ s and $t = 2.5$ s) it can be observed that the rotation cannot be followed unambiguously, since the cap is at no time oriented perpendicularly (perpendicular to the xy-plane) to its previous position. Apart from the variations in the time taken by the different EB-JPs to perform the steps, observed from the intermediate stages of the steps, no significant differences in their qualitative motion behavior and therefore no obvious relation to their caps' magnetic state can be inferred from Fig. 4.6 (a)-(d) with the current image quality. For instance, observable differences would have been expected for the rotational movement accompanied by the small transport step when comparing JPs with onion and vortex state caps due to different spatial alignments of the respective net magnetic moments. The physical reason for the absence of recognizable motion variations in the conducted experiments is not entirely clear, but may be attributed to either the JPs being in the same remanent

magnetic state for all considered t_F or an influence of the external magnetic field on the JPs' magnetic state. The first reason ca be easily discarded as magnetic characterization measurements, conducted prior to particle transport, revealed significant differences in the remanent magnetization of the JPs as a function of t_F. These measurements are not included, as their discussion would be beyond the scope of this thesis. As for the second reason, the combination of MFL and the externally applied magnetic field could lead to remagnetization within vortex state JP caps and therefore to similar alignments of net magnetic moments within the JPs' caps for all considered t_F, resulting in indistinguishable motion behaviors. To gain further insights, the motion of not only single EB-JPs but also of agglomerates was qualitatively studied as well.

It should be noted, that the assembly behavior of ferromagnetically capped JPs dispersed in liquid is a research field on its own [SGM09, YBG15, LCFK19]. Besides planar hexagonal sheets and microtubes [YBB12], mostly double-chain or zigzag structures have been reported [RRS12], where the formed configuration depends on the choice of externally applied magnetic field sequence and the cap thickness and composition. The here investigated EB-JPs also show assemblies of different configuration depending on the ferromagnetic film thickness as will be analyzed in the following.

Figure 4.7 (a)-(c) illustrates the movement of agglomerates for EB-JPs with t_F = 10 nm, 40 nm and 60 nm, respectively. These thicknesses were selected as they represent the three main configurations that the agglomerates exhibited in the experiments. These agglomeration configurations were observed in multiple transport experiments for the corresponding thickness, typically formed for agglomerates with high particle density. Here, in contrast to the snapshots shown previously in Fig. 4.6, the motion dynamics start at t = 0 s related to the fields $H_z \cdot \mu_0 = H_x \cdot \mu_0 = 0$ mT (cf. Fig. 4.7 (d)). This allows to visualize the agglomerates prior to the modification of the MFL, i.e., without an alignment with respect to an applied external magnetic field. Moreover, individual particles within the agglomerates can still be partially recognized at this position, since the agglomerates rest within the focal plane of the microscope. At t = 0 s, the agglomerate of EB-JPs with t_F = 10 nm (cf. Fig. 4.7 (a)) shows an arrangement similar to an hexagonal array, whereas the agglomerates for EB-JPs with t_F = 40 nm and 60 nm display a formation similar to a bent chain. Starting from t_F = 40 nm the EB-JPs agglomerates began to show this characteristic. The snapshots around t = 0.5 s show how each

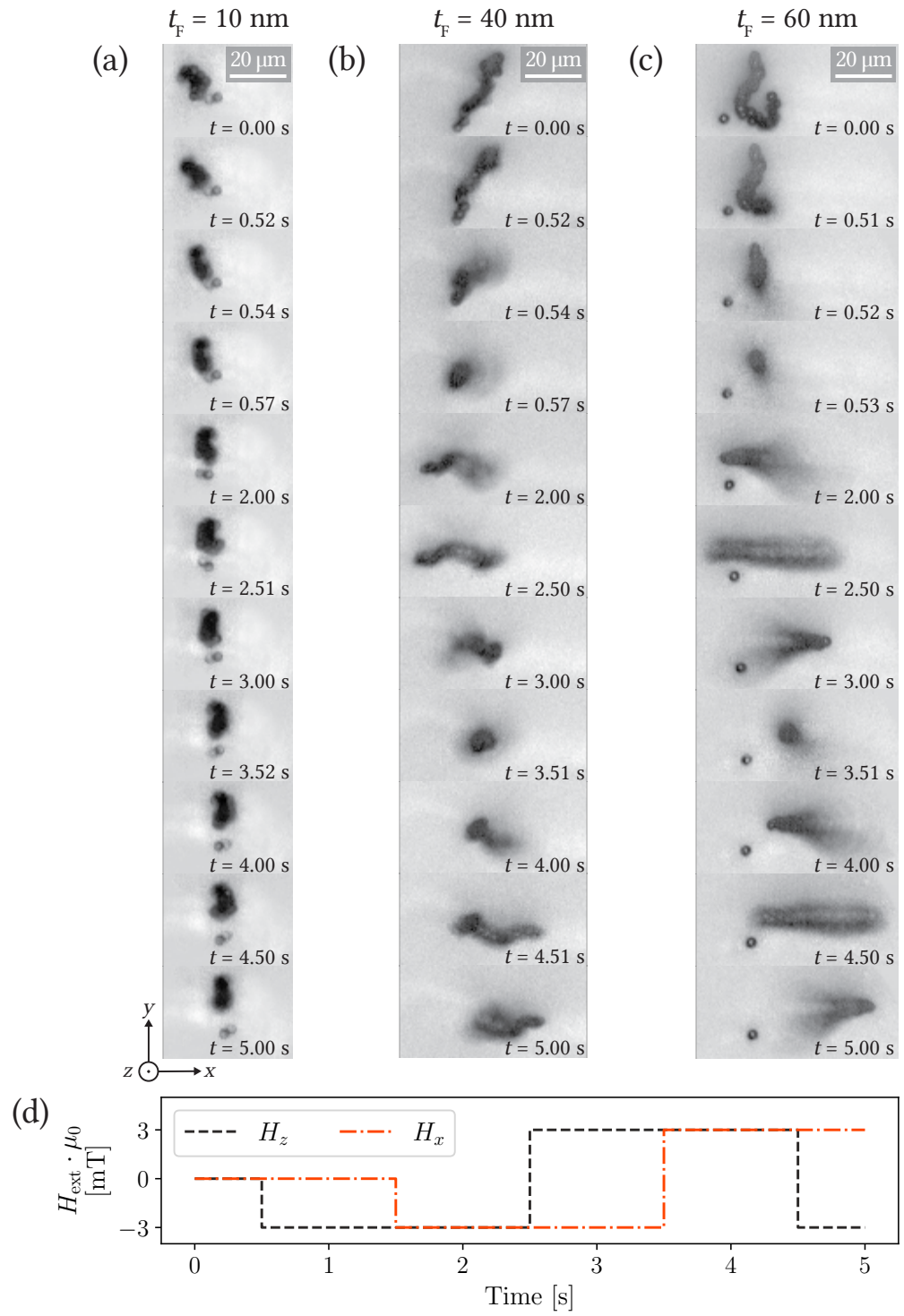

Figure 4.7: Visualization of EB-JP agglomerate movement on a substrate with hh/tt parallel stripe domain pattern. (a)-(c) Microscope snapshots of exemplary EB-JP agglomerates with t_F = 10 nm, 40 nm and 60 nm, respectively, at different times during the experiment. The indicated time on each image corresponds to a time within the applied magnetic field sequence shown in (d).

of the agglomerates aligns after the external magnetic field $H_{max,z} \cdot \mu_0 = -3$ mT is applied, where again, a clear distinction can be made between the agglomerates for Fig. 4.7 (b) and (c) as compared to (a). Here, the agglomerates for thicker t_F align along the z-axis, while for thinner t_F, the agglomerate creates a cluster shape. This may be explained as the magnetic moment of EB-JPs with $t_F \geq 40$ nm is larger than for thinner t_F, and thus, their magnetostatic interaction is strong enough to keep the particles stable in a vertical chain. However, focusing on the snapshots in Fig. 4.7 (b), it can be observed that the chain shows a wavelike shape, particularly visible at times when the external magnetic field in z-direction is inverted (around $t = 2.5$ s and $t = 4.5$ s). This observation may be connected to the magnetic states expressed by the particles caps (cf. Section 2.4). While in purely ferromagnetic caps, thick ferromagnetic layers exert vortex states which possess only a weak remanent magnetization. Thin ferromagnetic layers, on the other hand, can stabilize magnetic textures, like onion states, which possess a larger net magnetization. For the here studied EB-JPs, it has been shown that the Exchange-Bias affects the magnetic cap's remanent state [TRH21, Reg22]. Hypothetically, EB-JPs with $t_F = 40$ nm could exhibit an unstable magnetic state, i.e., around this thickness the particle caps potentially transition from an onion or a shifted vortex with an absolute (non-zero) net magnetization to a vortex state or a mixed or metastable state with reduced net magnetization [Reg22]. By further increasing the thickness of the ferromagnetic layer, the caps transition to another stable state, e.g., a multidomain state[1]. This magnetic configuration possibly allows for the alignment of the magnetic orientation within these domains driven by the external magnetic field and the other particles in their environment, so that the particles can build and stabilize chains or tubular agglomerates by dipolar interaction (cf. Fig. 4.7 (c) for $t = 2.5$ s and $t = 4.5$ s).

It should be mentioned that, although agglomerates cannot be used to determine single EB-JP velocities, they strongly interfere with the analysis of individual particles. This is because, while moving across the substrate, the agglomerates pick up nearby individual particles or even merge with other agglomerates. This observation was prominently made in experiments with EB-JPs with thick t_F, as the agglomerates have a higher range due to their chain-like alignment. Moreover, because of their larger size, they move faster, in the sense that they can

[1] Multidomain state formation has been shown to be the the preferred state of EB (IrMn(5 nm)/NiFe(6 nm)) disks with a diameter of 3 µm [SAKS09].

cross more than one domain at a time, as can be seen by comparing the agglomerate with the individual particle in Fig. 4.7 (c). As a consequence, this behavior unfortunately lowers the statistics of the quantitative analysis of the individual particles velocity, as their number is more and more reduced when the chains collect the individual JPs to form even larger agglomerates.

4.3 Influence of the Magnetic Cap Composition on the Translational and Rotational Velocities

The analysis of the 1D EB-JPs transport step motion presented in Section 4.1 led to the mean steady-state translational and rotational velocities of the EB-JPs shown in Fig. 4.8 (a) and (b), respectively. The translation and rotation analyses were carried out taking into account the two stripe domain types present in the parallel-stripe domain patterned sample used for the transport experiments. In addition to the mean steady-state translational and rotational velocities as a function of EB-JPs cap thickness t_F, Fig. 4.8 (c) and (d) show the number of evaluated steps from which the average velocities were determined. The translational and rotational velocities both follow a trend, where with increasing cap thickness from t_F = 5 nm to 20 nm, the EB-JPs move and rotate faster. Afterward, both velocities decrease for t_F = 30 nm and 40 nm, to finally increase again for EB-JPs caps with t_F > 40 nm. Comparing the mean steady-state velocities with respect to the two stripe domain types, it can be observed that for the translational motion, as well as for most of the rotational motion, the EB-JPs move/rotate faster when this motion is related to the thin stripe. As previously mentioned in Section 4.1.2, this is attributed to the stray fields of the thin stripe forming in a more confined area (xy-plane), thus, creating larger potential energy gradients for the particles. In this case, it is hypothesized that the faster rotation of the EB-JPs is related to their faster translational motion, i.e., since both particle motions take place simultaneously, the faster transport of the JPs additionally accelerates the accompanied rotational motion. Here, it should be noted that the substrate employed to perform these experiments was fabricated via IBMP (cf. Section 2.3.4). This method modifies the magnetic properties of the bombarded area (in this case of one type of stripe), more precisely, the anisotropy strength and saturation magnetization are reduced for the bombarded stripes. This leads to asymmetric magnetic charge

profiles within the DWs (cf. Section 2.5.1), thus creating a MFL with additional asymmetry. This additional asymmetry in the MFL could also influence the velocity difference with respect to the stripe width. This trend of higher velocity for thin-stripe related motions seems to be in disagreement only for EB-JPs with cap thickness $t_F = 100$ nm. However, as the number of evaluable steps is significantly decreased in this case, the resulting velocities for $t_F = 100$ nm have a lower statistical significance.

It was hypothesized that for thicker t_F, the EB-JP caps have a higher magnetic moment due to a larger amount of ferromagnetic material, leading to a stronger magnetic force acting on the EB-JPs (cf. Section 2.5.2) within the transformed MFL, and thus, faster particle motion. Therefore, it is striking that the EB-JP steady-state velocities decrease for caps with $t_F = 30$ nm and 40 nm. This can be related to the qualitative analysis of the motion of EB-JP agglomerates presented in Section 4.2, where it is assumed that around this thickness, the magnetic state of the EB-JPs caps transitions from one texture to another. Therefore, taking the qualitative and quantitative results from the influence on the motion dynamic of EB-JPs with respect to t_F and results from previous investigations on the magnetic properties of caps (cf. Section 2.4) into account, the following hypothesis for a phase diagram can be inferred:

1. For low t_F (5 nm, 10 nm and 20 nm), the caps are expected to have a remanent onion magnetization state or at least a far enough shifted vortex state due to the contribution of the unidirectional anisotropy in the cap induced from the EB interaction. This leads to caps with a certain (non-zero) net magnetic moment.

2. For intermediate t_F (30 nm and 40 nm), the EB interaction is not strong enough to induce the unidirectional anisotropy, consequently, the caps incorporate the energetic more favorable magnetization, i.e., a vortex state. This results in caps having a reduced net magnetic moment.

3. For high t_F ($t_F \geq 50$ nm), the caps present a multidomain texture with in-field aligned domains [SAKS09], leading to caps with large magnetic moments.

Considering that the mobility of the EB-JPs is primarily determined by the magnetic moment of their cap (cf. Section 2.5), the trend of the determined steady-state velocities (cf. Fig. 4.8 (a) and (b)) can be better understood.

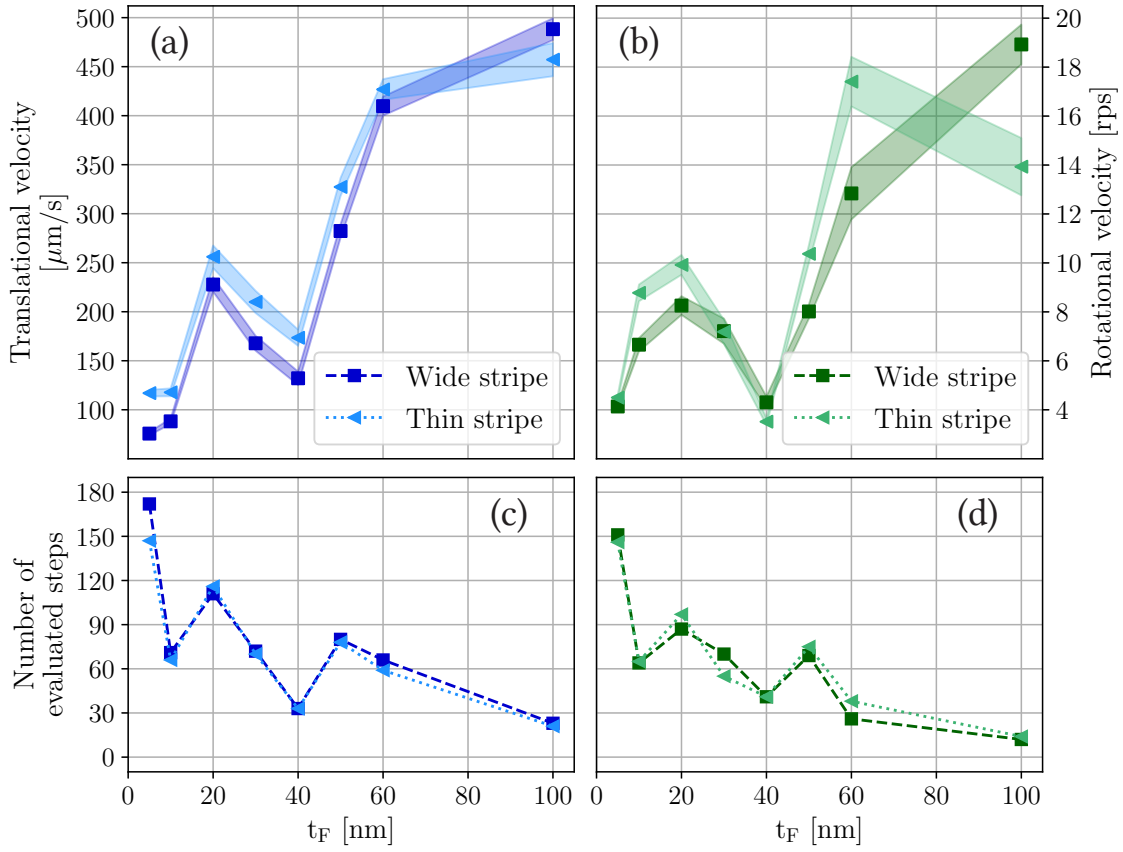

Figure 4.8: Quantitative results for the evaluation of translational and rotational motion of EB-JPs over a parallel-stripe domain pattern as functions of their cap thickness t_F. The results are shown in relation to the two types of stripe domains present in the sample used to perform the 1D transport experiments, where squares with dashed lines represent wide stripes and triangles with dotted lines represent thin stripes. Mean steady-state translational and rotational velocities of EB-JPs are shown in (a) as blue data points and in (b) as green data points, respectively. Transport experiments were conducted with external magnetic field strengths $H_{max,z/x} \cdot \mu_0 = 3$ mT and a quarter period of the external magnetic field sequence $T/4 = 1$ s. Shaded areas indicate the standard deviation of the mean velocities. (c)-(d) Number of transport steps evaluated for the determination of the mean steady-state translational and rotational velocities, respectively. The lines are included as a guide for the eye. There is no direct relationship between the number of steps analyzed and the number of videos/particles analyzed for each t_F.

Although a greater number of evaluated steps is desired to improve the reliability of the statistical analysis, it should be noted that the results present low standard deviations, shown in Fig. 4.8 (a) and (b) by the shaded areas. Particularly, low standard deviation values can be observed for the EB-JPs with t_F = 5 nm, 10 nm and 50 nm, although, for t_F = 10 nm and 50 nm only less than half as many steps were evaluated as for 5 nm. To obtain the number of steps shown for t_F = 5 nm, it was only necessary to analyze three particle transport recordings, showing a total of 27 traceable individual particles. However, for t_F = 40 nm and 100 nm six and four particle transport experiments were recorded, where only a total of six and three particles could be used for the analysis, respectively. This can be again related to the qualitative analysis, where it was shown that for thicker t_F the agglomerates impose difficulties on the transport of individual particles. Thus, although EB-JPs with thinner t_F of their caps exhibit slower steady-state translational and rotational velocities, their motion dynamics may be addressable in a more controlled fashion, which improves their overall applicability.

2D Transport: Correlation of JP Trajectories and Domain Pattern

5

Continuing with the analysis of the motion dynamics of Exchange-Bias capped Janus particles (EB-JPs) within tailored magnetic field landscapes(MFL), an experimental approach that correlates the trajectories of transported magnetic particles with the artificial domain pattern exhibited by the underlying substrate is presented in this chapter. The concept of remotely controlling the motion of magnetic particles via dynamic transformation of MFLs over a topographically flat Exchange-Bias (EB) thin film system was initially proposed using a magnetic parallel-stripe domain pattern [HKB15]. Although the resulting MFL allows only for a one-dimensional transport of magnetic particles, this prototypical system has been studied thoroughly [EKH15, USK16, RHE21, HRT21, HRS22], building the foundation for the development and investigation of more complex domain patterns for use in particle transport. For instance, magnetized stripe domains exhibiting gradually varying length or gradually modified stripe width [Huh22], concentric hollow cylinders [UHE18], hexagons in a honeycomb-like pattern [Gö19], and squares in a checkerboard-like pattern [GHH16] have been utilized for inducing all kinds of different particle motion behaviors. Typically, magnetic particles guided over these patterns show more complicated, two-dimensional (2D) trajectories, which can be applied to achieving, e.g, focusing of a particle population at a defined sample position. However, analyzing the particle motion with respect to the position of magnetic domains, respectively domain walls (DWs), in the underlying substrate becomes a non-trivial task in this case, since the domain structure at itself is not visible within the recordings of particle transport obtained by optical bright-field microscopy.

This information is often times crucial for a more complete understanding of the observed particle motion dynamics, especially when studying different characteristics of the system, e.g., domain and particle geometries and sizes, magnitude and length of the external magnetic field pulses, magnetic properties of

the particles (e.g., the analysis presented in Chapter 4), biofunctionalization, etc. Therefore, a systematic method for correlating particle trajectories, i.e., particle transport individual steps, with the underlying magnetic domain pattern is desired. Furthermore, a thorough understanding of particle motion over different magnetic domain configurations would lead to an improvement in the design of future patterns with more complex geometries. This holds especially true for asymmetrically structured magnetic particles, like the herein investigated EB-JPs, that exhibit an additional degree of motion freedom by being able to rotate.

As a case study, the motion of 3 µm sized EB-JPs over a 2D transport checkerboard-like domain pattern was analyzed in this work. This pattern was fabricated by means of a two-step photolithography process in combination with ion bombardment induced magnetic patterning (IBMP) [GEU18, Gö19], and consists of squared domains with an area of 5 µm × 5 µm in a periodically repeated head-to-head (hh)/tail-to-tail (tt) domain configuration along one spatial dimension and head-to-side (hs)/tail-to-side (ts) domain configuration along the other dimension. The EB-JPs used for this analysis were fabricated as described in Section 3.1, however, in contrast to the analysis presented in Chapter 4, only EB-JPs with a ferromagnetic layer thickness $t_F = 10$ nm of the cap were investigated. Typically, to induce the 2D directed motion of the magnetic particles within the employed particle transport system, external magnetic field pulses are additionally applied along the y-axis, which is defined to be within the substrate plane, orthogonal to the x-axis (cf. Section 2.5.3). However, in this analysis the additional pulses, compared to the one-dimensional (1D) transport mechanism, were applied along the x-axis, due to the selected sample alignment, which consisted of rotating the sample 90° in the xy-plane. This alignment was kept constant throughout all analytical methods employed in this investigation. The pulses in the x-direction were hereby applied with the same phase as the pulses in y-direction, i.e., with a phase shift of 0 with respect to the y-pulses and a phase shift of $\pi/2$ with respect to the z-pulses. However, the amplitude of the x-pulses was varied for different transport experiments (from $H_{\max,x} \cdot \mu_0 = 1$ mT to 4 mT), while the amplitude for the pulses in y- and z-direction were kept constant at $H_{\max,y/z} \cdot \mu_0 = 3$ mT. All transport experiments regarding this analysis were recorded at 500 fps using a 100× magnification objective and a quarter period of the external magnetic field sequence $T/4 = 1$ s.

At the beginning of the investigation a selected area (cf. Section 5.1.1) of the sub-

strate used for the 2D particle transport experiments was characterized by means of Kerr microscopy (cf. Section 5.1.2) and Magnetic Force Microscopy (MFM) (cf. Section 5.1.3). Afterward, the transport experiments were carried out, and the recorded videos were analyzed following the method presented in Section 3.4. Finally, a map of the EB-JPs trajectories over the checkerboard-like pattern was obtained by combining the information obtained from the Kerr microscopy and the particle transport analysis (cf. Section 5.2.1). Additionally, the translational and angular motions of the EB-JPs were analyzed with respect to the individual transport steps (cf. Sections 5.2.2 and 5.2.3, respectively), and a transition field strength for switching from vertical to diagonal particle trajectories was determined (cf. Section 5.2.4).

5.1 Substrate Characterization

In order to relate the trajectories of transported EB-JPs to the underlying domain pattern, it was first necessary to select a specific area of the sample later used for the transport experiments and to magnetically characterize it by means of Kerr microscopy and MFM. The results of these characterizations will be presented in the following sections.

5.1.1 Reference Point Identification

To generate a map of the trajectories followed by the EB-JPs during their transport over the sample with the checkerboard pattern, it was first necessary to establish an area of interest of the sample. This was done to focus the magnetic characterization to a specified section of the sample and, consequently, to carry out particle transport experiments over this area. This required generating a map of the sample itself as shown in Fig. 5.1 (a), which could then be used to analyze the entire area for a large distinctive mark (cf. Fig. 5.1 (b)) that can easily be found in both magnetic characterization and transport experiments. It is important to define the area of interest as close to the center of the sample as possible for two reasons. First, the border of the sample area is typically covered by the Parafilm® frame used to create the microfluidic chamber needed for the transport experiments (cf. Section 3.3), represented in Fig. 5.1 (a) by the light blue frame, and secondly, the utilized microscope objective within the particle transport setup cannot reach the

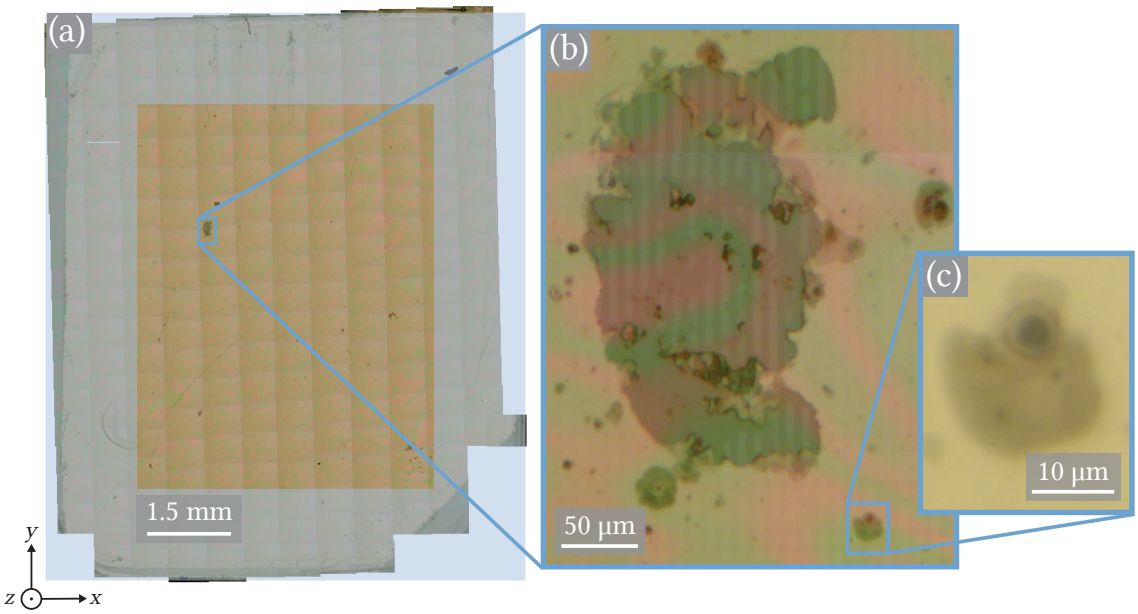

Figure 5.1: Identification of a reference point in the 2D transport substrate from optical microscopy images at different magnifications. (a) Map of the full sample consisting of 226 individual optical microscopic images recorded with a 10× objective. (b) Zoomed area of the rectangle indicated in (a). (c) Selected reference point for the transport experiments.

edges of the sample due to space limitations. However, it is also relevant to select a mark large enough to be easily identified with the naked eye in order to correctly place the sample under the microscope. Afterward, a second mark close to the initial large mark, but considerably smaller in size, was selected as the reference point (cf. Fig. 5.1 (c)). This mark had a unique form and an adequate size, such that it would completely fit in the recorded images of the transport experiments without covering most of the field of view (cf. Section 5.2.1). It should be mentioned that these reference marks are defects on the sample, so they have not been created deliberately. Therefore, the inclusion of a reference mark in the future design of transport domain patterns would improve this procedure.

The large mark was first located with the optical microscope of the particle transport setup in combination with a 40× magnification objective. Once the area of interest was located, the process was repeated using an 80× magnification objective. Finally, from the previous position, the reference point was located using a 100× magnification objective. For this process it was convenient to have the map of the complete sample (cf. Fig. 5.1 (a)).

5.1.2 Kerr Microscopy Imaging

Kerr microscopy imaging allows visualization of magnetic domains and magnetization processes (cf. Section 3.2.2) [HS98]. Therefore, it was used to obtain a magnetic domain map of the checkerboard sample and establish the magnetization direction of the individual domains. To this end, two analyses were carried out with the Kerr microscope, one to investigate the magnetic domain contrast of the sample in the remanent state regarding the y-axis (same axis system as in Fig. 5.1) shown in the left column of Fig. 5.2 and the second with respect to the x-axis, shown in the right column of the same figure. Considering that the magnetically patterned thin film exhibits an in-plane magnetization, both measurements were performed in longitudinal magneto-optical Kerr effect (L-MOKE) geometry (cf. Subsection 3.2.1). The analysis for the magnetization of the sample along the y-axis was done with parallel polarized (p-polarized) light (L-MOKE $\parallel$) and with the external magnetic field $+\vec{H}_{\mathrm{ext},y}$ in the $-y$-direction (in the xy-plane). For the analysis along the x-axis, perpendicularly polarized (s-polarized) light (L-MOKE $\perp$) was used in combination with $+\vec{H}_{\mathrm{ext},x}$ in the $+x$-direction. In both cases, the microscopic analysis consisted of first locating the previously defined reference point and then recording individual frames of an area surrounding the reference point while varying the external magnetic field. The applied external magnetic field was changed between ca. 30 kA/m and ca. −30 kA/m, to ensure that positive and negative saturation of the sample magnetization are included. At this point, the recorded raw images show no magnetic contrast visible to the naked eye. Therefore, a reference frame must be subtracted from all other individual frames. To do so, the drift between images occurring due to experimental conditions must first be corrected. The drift correction, as well as other parts of this analysis, were performed using analysis techniques developed in the research group. To correct the drift between individual frames, each frame (f_i) is compared to the initial frame (f_0). Here, the f_0 was taken at positive saturation, i.e., $\vec{H}_{\mathrm{ext}} =$ ca. 30 kA/m. For each pair of frames (f_i, f_0) the image noise is reduced by means of Fourier transformation and low pass filtering, with the resulting pixel gray scale values being normalized. Then, f_i is shifted with respect to f_0 for a defined shift interval, resulting in a mean squared error when calculating the difference between pixel gray scale values for a set area of f_i and f_0. Performing this procedure for several shift intervals, the shift with the minimum error is selected and applied to f_i to obtain a corrected frame f_i'. Finally, the difference image $f_\mathrm{i}' - f_0$

yields the magnetic contrast for oppositely magnetized domains along the chosen sensitivity axis, e.g., as shown in Fig. 5.2 (a) for $H_{\mathrm{ext},y}$ of ca. 0 kA/m and in Fig. 5.2 (b) for $H_{\mathrm{ext},x}$ of ca. −12 kA/m. Here, $f_0 - f_\mathrm{i}'$ would lead to an inversion of the grayscale.

To determine the magnetization direction of the different domains present within the analyzed checkerboard-patterned substrate, a magnetic contrast image corresponding to the remanent magnetization state of the sample was initially investigated. From this image, areas A_i corresponding to visible domains with different magnetization directions were selected, as well as a larger section including all occurring domain types to represent the entire sample (cf. Fig. 5.2 (a) and (b)). Subsequently, as for the individual frames, a subtraction of the individual areas $f_\mathrm{i}'(A_\mathrm{i}) - f_0(A_\mathrm{i})$ was calculated. The mean pixel gray scale value of each resulting area was then taken as a representation for the magnetization M of that area projected on the chosen sensitivity direction, for the corresponding H_ext. After normalization of M, the hysteresis loops shown in Fig. 5.2 (c)-(f) were obtained.

From the fabrication process described by *Gaul* et al. in [GEU18] for a checkerboard-like domain pattern, the sample is expected to exhibit periodic repetitions of domains with hh/tt magnetization configuration along one in-plane axis and of domains with hs/ts magnetization configuration along the in-plane axis perpendicular to the previous one. Focusing first on the hystereses shown in Fig. 5.2 (c), it can be observed that two curves resemble magnetization reversals along the easy axis (green and yellow solid lines), while the other two show reversals for a hard axis (blue and purple dashed lines). Consequently, the magnetization direction for the domains marked by the yellow and green frames (top and bottom left domains) lies within the axis of $\vec{H}_\mathrm{ext}$, in this case, along the y-axis. Additionally, the yellow hysteresis shows a larger coercive field H_C and EB field H_EB, which indicates that the hysteresis corresponds to the domain with the original magnetization direction (EB_0) imprinted on the sample. This is due to the fact, that both H_C and H_EB magnitudes are known to be reduced for an ion-bombarded sample given a large enough ion dose [CBF98, MMJ01]. Thus, the green hysteresis (IB_1) with lower H_C and H_EB is most likely resembling the ion-bombarded area of the sample with inverted magnetization direction compared to the original magnetization state. Furthermore, it can be seen from the hysteresis that the magnetization for EB_0 at remanence has not yet reversed, which indicates that, the domain corresponding to EB_0 marked by the yellow frame has a magnetization

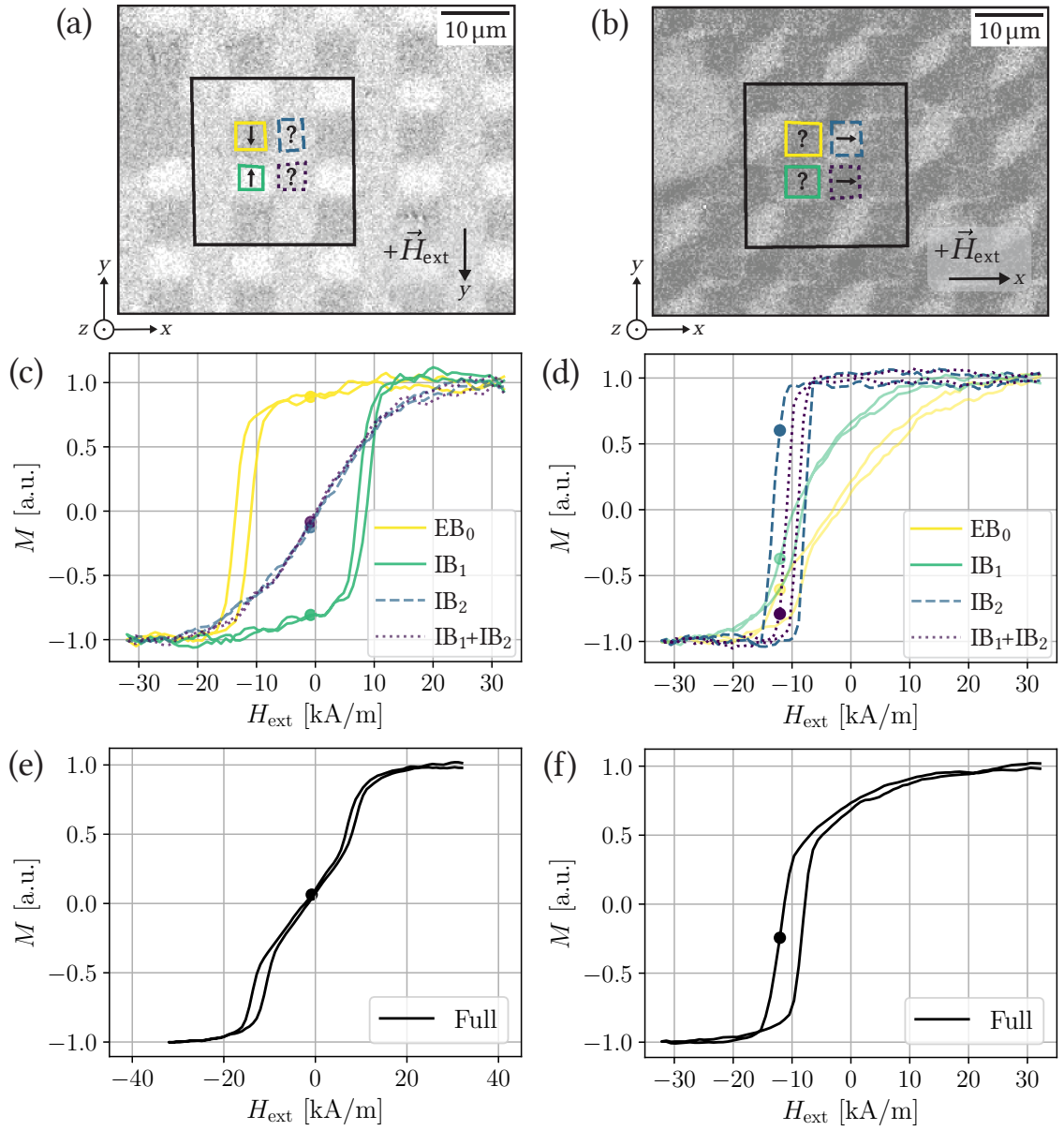

Figure 5.2: Magnetic domain mapping of the 2D transport substrate by means of Kerr microscopy. Analyses performed in L-MOKE geometry with p-polarized light to maximize the contrast of the magnetic domains with vertically opposed magnetization directions (left column) and with s-polarized light to show the contrast of the domains with horizontally opposed magnetization directions (right column). (a) and (b) Contrast images obtained from Kerr imaging subtraction. Here, part of the reference point used for subsequent particle transport experiments can be seen at the left edges. (c) and (d) Magnetization curves extracted from Kerr measurements for individual domains of the checkerboard pattern shown in (a) and (b), respectively. (e) and (f) Magnetization curves extracted from Kerr measurements for the black marked areas shown in (a) and (b), respectively, representing the remagnetization behavior of the whole sample. The circular points in (c)-(f) mark the H_{ext} at which the Kerr images (a) and (b) were taken.

direction aligned parallel to $+\vec{H}_{\mathrm{ext},y}$ as indicated by the black arrow. Following a similar analysis for the green hysteresis, it is determined that this hysteresis represents a domain whose magnetization direction has been imprinted after the first ion bombardment procedure IB_1, in this case, in the opposite direction to EB_0. These opposite domain magnetization directions, are also evidenced by the highest contrast between the EB_0 and IB_1 domains in Fig. 5.2 (a). However, the magnetization direction of the domains marked by the blue dashed and purple dotted frames cannot be determined unambiguously by this analysis. Hence, additional measurements with the sensitivity axis now being perpendicular to the previous one were conducted, with the results presented in Fig. 5.2 (b),(d), and (f). Following the same procedure as above, it can be observed that now EB_0 and IB_1 correspond to reversals along a hard axis and the blue dashed and purple dotted hystereses to reversals along the easy axis of their corresponding domains. Here, the blue and purple hystereses represent domains with a similar remagnetization behavior, i.e., their remanent magnetizations must be aligned in the same directions. However, the purple dotted hysteresis has a smaller H_{C} and H_{EB}, indicating that the corresponding domains have been exposed to a higher ion dose during the IBMP process than the domains marked by the blue dashed frames. Comparing with the IBMP process described in [GEU18] it can be deduced that the domain with the blue dashed frame (top right) corresponds to areas of the sample that have been ion bombarded in the second stage (IB_2) of the IBMP, and that the domain with the purple dotted frame (bottom right) corresponds to areas which were ion bombarded twice (IB_1+ IB_2). Finally, considering that at remanence the IB_2 and IB_1+ IB_2 domains have not reversed their magnetization direction, when coming from positive saturation, it can be determined that the remanent magnetization direction of both domains points parallel to $\vec{H}_{\mathrm{ext},x}$ as indicated by the black arrows. Although the image in Fig. 5.2 (b) was taken at around $H_{\mathrm{ext},x} = -12$ kA/m, which is shown here for maximum visibility of the different domain types, the indicated magnetization directions of IB_2 and IB_1+ IB_2 domains are still referring to the remanent magnetization state.

In both analyses, a black hysteresis is included as shown in Fig. 5.2 (e) and (f) to represent the contributions of the individual domains to the magnetic characteristics of the whole sample. Furthermore, it can be seen in all hystereses that the magnetization state of the individual domains is stable around remanence. Therefore, external magnetic field pulses with magnitudes of a few kA/m applied

to induce the transport of EB-JPs above this sample does not significantly alter the magnetization state of the sample. Nevertheless, it should be noted that asymmetric DWs are present in the sample due to different anisotropy strengths in the neighboring domains [GEU18], which could influence the particle trajectories.

5.1.3 Magnetic Force Microscopy Analysis

In addition to the Kerr microscopy characterization of the checkerboard pattern, a magnetic force microscopy (MFM) analysis of the sample was performed to obtain information about the distribution of magnetic charges within present DWs. MFM is situated within the family of scanning probe microscopy techniques, where samples can be imaged through interactions between an ideally atomically thin tip with the sample surface. In MFM, the focus is on magnetic interactions, which can be measured by incorporating a magnetic force on the probe. This technique can be used to analyze magnetic stray fields above the sample surface and thereby also magnetic charge distributions within the sample [RMG90]. These magnetic charge distributions can be used to characterize magnetic domain formation, e.g., artificial domain patterns. Therefore, it was employed to laterally characterize the checkerboard-like domain pattern used in this work.

The MFM measurements for this analysis were carried out in an area close to the reference point established in Section. 5.1.1, at a tip elevation of 100 nm from the sample. The phase contrast image of the selected area is shown in Fig. 5.3 (a). Here, the domain color classification and magnetization directions obtained from Kerr microscopy (cf. Section 5.1.2) is additionally included. In this image, the checkerboard pattern is visible similarly to the contrast image shown in Fig. 5.2 (a), as the pattern is particularly visible along the stripes similar to the one marked by the number 1. It is also along these stripes where the phase contrast is greatest, which is to be expected due to the opposite magnetization direction of the domains located along these stripes, creating hh- and tt-DWs. A minor, but still visible, contrast can also be observed along both types (3 and 4) of horizontal stripes, corresponding to hs- and ts-DW. However, there is no visible contrast within the vertical stripes similar to the one marked with the number 2, since both types of domains located along this area have the same magnetization direction, ergo, there is no DW between them. These observation are corroborated by the phase signal line profiles shown in Fig. 5.3 (b) and (c) extracted from the areas

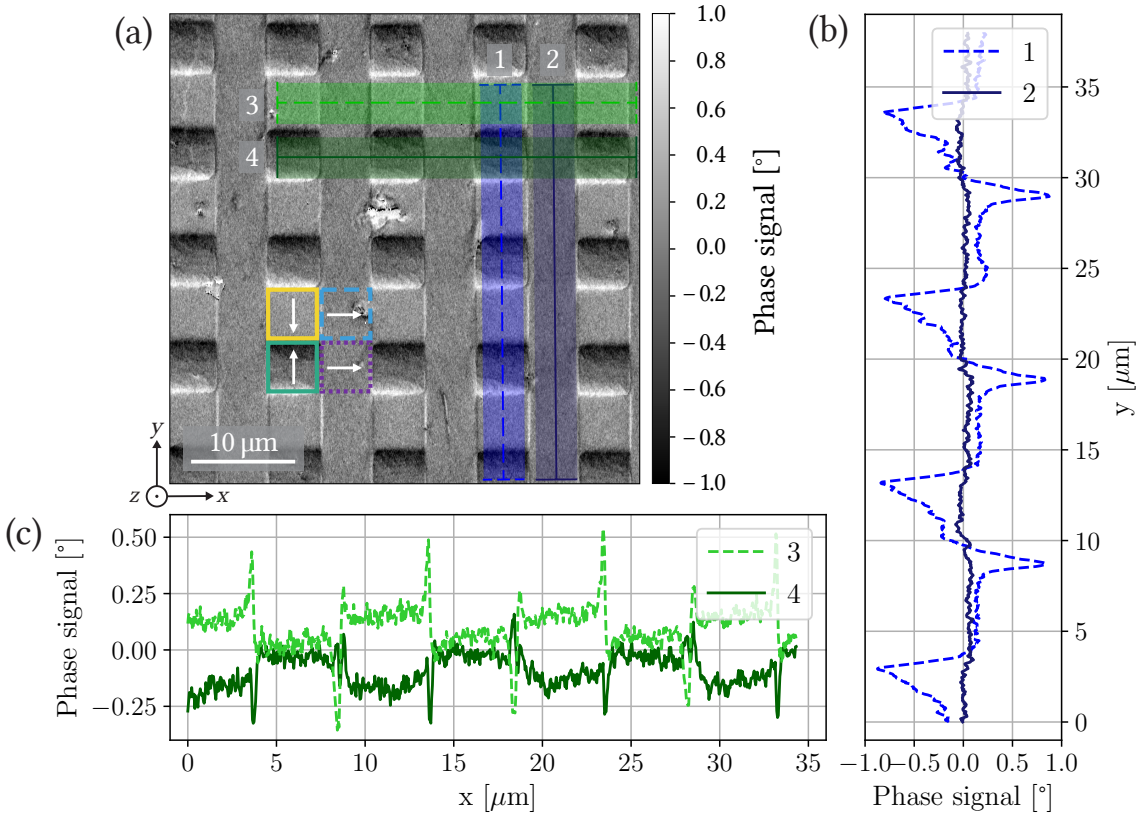

Figure 5.3: Characterization of magnetic charge distributions within a checkerboard pattern by means of MFM. (a) Scan of a sample area, located in the proximity of the reference point, with a size of 45 µm × 45 µm at an MFM tip lift height of 100 nm. (b) Phase signal of line profiles in vertical direction extracted from the areas highlighted in blue in (a), also marked by the numbers 1 and 2. Here, the y-axis increment corresponds to (a) from bottom to top. (c) Phase signal of line profiles in horizontal direction extracted from the areas highlighted in green in (a), marked by the numbers 3 and 4. The color coding for the domains and magnetization directions established in Sec. 5.1.2 are included in (a) for reference.

in Fig. 5.3 (a) highlighted in blue for the vertical stripes and in green for the horizontal stripes. The vertical line profile corresponding to the stripe 1 (blue dashed line), shows the largest variations of the phase signal in the form of peaks and dips, with its maxima and minima located at the boundaries of the domains. This line profile has the shape observed for profiles across 5 µm stripe domains with hh/tt configuration [GEU18], where the peaks and dips have a symmetry similar to a monopolar charge contrast [HZK13]. Additionally, from the distances between

the peak and dip positions, the vertical dimension of 5 µm for the individual domains can be confirmed. Furthermore, the horizontal dimension of the domains can also be confirmed from the distances between the peaks and dips in the horizontal line profiles shown in Fig. 5.3 (c). Here, the peaks/dips are narrowed and appear to be less symmetric, and have approximately half of the amplitude of the peaks/dips from the profile 1, which are characteristics of hs-DWs [HZK13]. The profiles 3 and 4 show opposite phase signal, which corresponds to the interaction at the same x position of the parallel domains IB_2 and IB_1+ IB_2 (cf. Section 5.1.2) with the neighboring domains EB_0 and IB_1, respectively, where EB_0 and IB_1 have opposite direction. In resume, the results obtained by MFM imaging of the investigated checkerboard-patterned sample support the information gained from Kerr microscopy measurements. The characterization of magnetic charge distributions indicates that identified hh/tt and hs/ts DWs are the sources of magnetic strayfields, therefore constituting the MFL above the sample that will guide the directed transport of magnetic particles.

5.2 Trajectory mapping

Once the checkerboard pattern was magnetically characterized, the next step was to perform EB-JP transport experiments and to obtain their trajectories via single particle tracking. Here, an area within proximity to the previously established reference point on the substrate was observed, so that acquired particle trajectories can be viewed with respect to the already characterized magnetic domain pattern (cf. Section 5.1.1). Afterward, the recorded videos were analyzed following the tracking procedure described in Section 3.4, which establishes a double analysis of the particle trajectories by using first a circular tracker and subsequently a rectangular one. From the tracking procedure, the x- and y-position of each individual EB-JP and its cap, and the cap orientation in the xy-plane can be determined for every frame of the recorded videos. Then, by combining individual frames of transport videos with positional information of transported particles and the measured map (cf. Section 5.1.2) of the underlying domain pattern, a visualization of EB-JPs trajectories in relation to the domain pattern can be obtained. The procedure for the practical realization that was conceptualized and conducted within the framework of this thesis will be presented in the following section.

5.2.1 Image Processing

A map containing the EB-JPs trajectories aligned to the underlying checkerboard domain pattern was obtained by merging information obtained from particle transport experiments, particle tracking and Kerr microscopy. The procedure developed to correlate the information from these different analyses consisted mainly of image processing using a Python-based algorithm, since the images recorded with the Kerr microscope and the particle transport setup had different resolutions. The main stages of this procedure are illustrated in Fig. 5.4. The first stage consisted of finding the correct scaling factor between images obtained by the employed Kerr microscope (denominated as Kerr image in the following) and the optical microscope used within the particle transport setup (denominated as transport image in the following). For this, a reference image from each analysis was taken. For the particle transport video, the selected reference image was a computed average image of the whole recording. This average transport frame was calculated by averaging all individual frames (their pixel values) of the corresponding transport video, resulting in an image in which only the background is visible, i.e., transported particles are removed (cf. Fig. 5.4 (a)). This ensures that the particles do not affect the comparison between the reference image from the Kerr analysis and this image. The reference image regarding the Kerr microscopic characterization is taken from measurements with sensitivity along the y-axis, specifically, the unsubtracted image taken at remanence (cf. Section 5.1.2) shown in Fig. 5.4 (b). To compare these images, the Kerr image must be scaled down, since it originally has a higher resolution than the transport image. This is achieved by transforming the image into a numerical array which can then be enlarged or reduced by spline interpolation using the Python libraries "OpenCV" [Bra00] and "SciPy" [VGO20]. Additionally, it has to be taken into account that the images could present a misalignment, originated from differing experimental procedures and conditions. Therefore, a range of rotation angles and scaling factors were tested on the Kerr image in order to find the best match towards the transport image. For this purpose, an area of proportional size enclosing the reference point is selected in both transport and reduced, rotated Kerr reference image. This area is shown in Fig. 5.4 (a) and (b) by a blue square centered at a similar location of the reference point. The images were then cropped so that only the selected areas are kept. Next, these regions of interest were compare to each other so that the correct scaling factor and rotation angle for adjusting the Kerr image (cf. Ap-

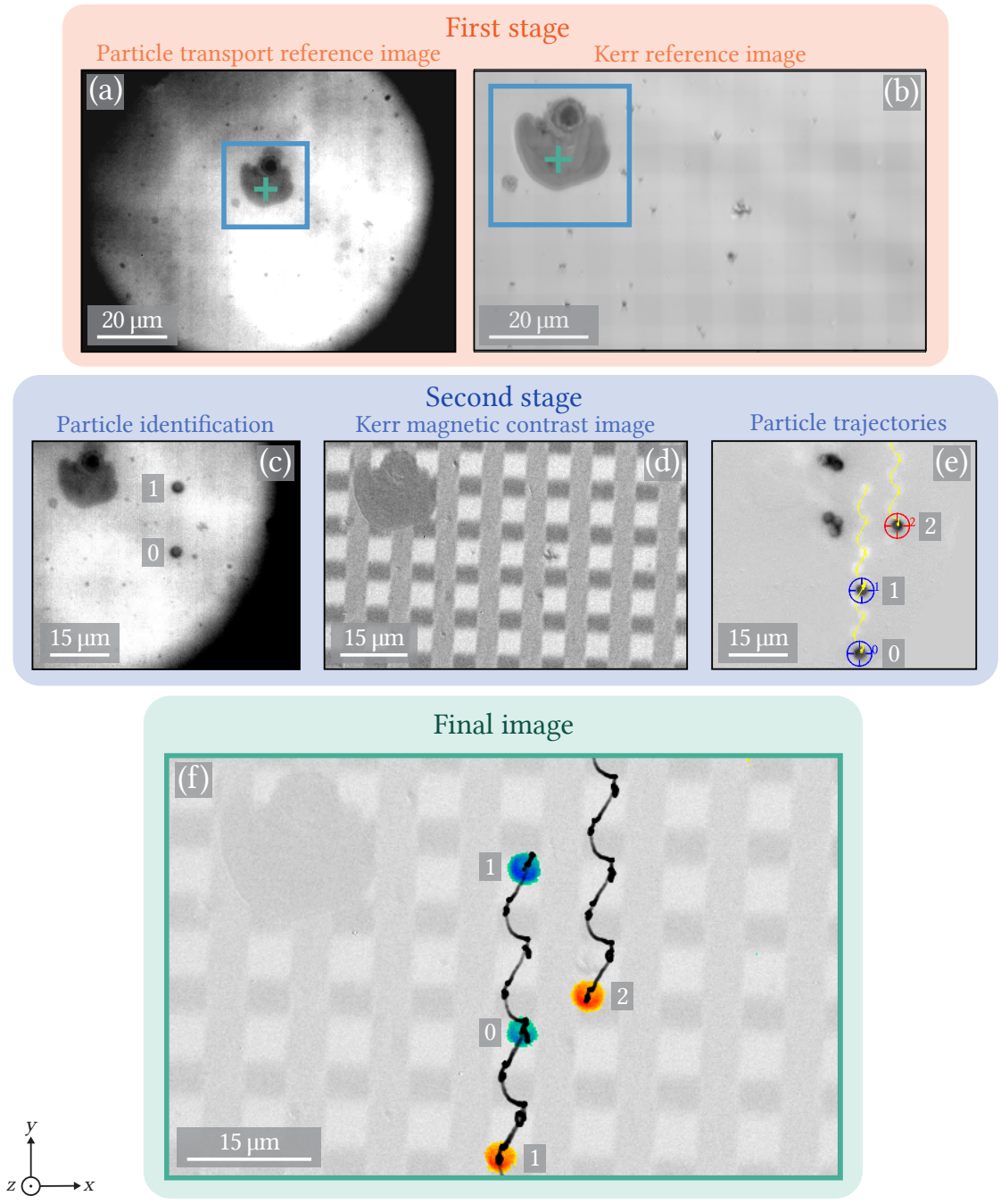

Figure 5.4: Image processing to determine 2D EB-JP transport trajectories in relation to the underling magnetic domain pattern. (a) Average image of a particle transport recording. (b) Unprocessed Kerr microscopy image of the checkerboard-patterned substrate. (c) Cropped frame of a particle transport recording including the to be analyzed EB-JPs. (d) Magnetic domain map (cf. Section 5.1.2). (e) Frame of particle transport recording with identified trajectories (yellow) of translated EB-JPs tracked by a circular marker (red or blue). (f) Exemplary visualization of EB-JP trajectories and cap orientations with respect to the underlying checkerboard-like domain pattern. For more information, please consult the text.

pendix A.4 for detailed information) could be found. From the reduced Kerr image and its proportional scale bar, an approximation of the correspondence between pixel size and physical dimensions in the transport images was determined. This pixel size determined for the transport images was also employed in the 1D transport analysis of EB-JPs presented in Chapter 4, since the particle transport setup does not have a system that automatically determine the pixel size.

Once the scaling factor and rotation angle were identified, the image processing procedure move to its second stage. To facilitate alignment of transport images with the Kerr image, each individual frame of the particle transport video and the average transport frame were cropped at the top and left edges according to the margins set when selecting the areas around the reference point, as shown in Fig. 5.4 (c). Subsequently, the average transport frame was subtracted from each individual frame to obtain images in which only the particles were visible. Then, the procedure described in Section 5.1.2 was performed on the original Kerr image shown in Fig. 5.4 (b) to add a magnetic contrast and therefore visualize the checkerboard-like domain pattern within the substrate. Afterward, the identified rotation angle and scaling factor were both applied to this image in order to obtain the corrected magnetic domain map like the one shown in Fig. 5.4 (d). In the next step, the particles trajectories shown in Fig. 5.4 (e) obtained from the circular tracking procedure (cf. Section 3.4) were corrected according to the corresponding shifts along the x- and y-axis resulting from cropping the transport and Kerr images. Finally, the information from the different analyses, i.e. the corrected Kerr and transport images together with identified trajectories of directionally transported EB-JPs, were merged to create the final image shown in Fig. 5.4 (f). Here, the Kerr image is taken as the new background for the particles with the trajectories on top. For clearer distinction, EB-JPs (blue or orange) are only shown for the first and close to last tracked frame of the particle transport video. The EB-JPs are depicted using a continuous color gradient so that the respective cap orientation is visible and the particles are still distinguishable from the grey-scaled background. The numbers to the left side of the particles in Fig. 5.4 (f) refer to the numbers in Fig. 5.4 (c) that show the initial position of the EB-JPs, whereas the numbers to the right side of the particles refer to the last visible position of the EB-JPs shown in Fig. 5.4 (e). By performing this process on individual frames of the whole particle transport recording, a video showing the translational and rotational motion dynaimcs of the EB-JPs over the underlying checkerboard-like

domain pattern can be generated.

The trajectories shown in Fig. 5.4 (f) correspond to EB-JPs transported by applying external magnetic field pulses with the following amplitudes $H_{\mathrm{max},y/z} \cdot \mu_0 = 3$ mT and $H_{\mathrm{max},x} \cdot \mu_0 = 1$ mT. Here, EB-JPs, although actuated above a pattern designed for 2D transport, show vertical trajectories (in the xy-plane). Comparing with the Kerr microscopy and MFM investigation, the particles are crossing the positions of hh/tt domain walls in this case, making the mechanism analogous to the 1D transport of magnetic particles over a stripe patterned substrate. The lack of a 2D transport, which has been previously reported to be inducible for superparamagnetic particles above the same substrate [Deu16], is supposedly related to the chosen amplitude of the external magnetic field pulses along the x-axis. Therefore, transport experiments were performed for different amplitudes of the field pulses $H_{\mathrm{max},x} \cdot \mu_0$ (from 1 mT to 4 mT) keeping $H_{\mathrm{max},y/z} \cdot \mu_0 = 3$ mT. This was done in order to find a transition field (for the x-axis) at which the particles switch from moving vertically to moving diagonally across the different magnetic domains. To get a complete picture of the observed motion dynamics, analyses of the trajectories with respect to the individual steps induced by the field pulses, for translational and angular motion, are presented in the following sections.

5.2.2 Translational Motion

Once a map of the trajectories of EB-JPs above the checkerboard pattern was obtained (cf. Fig. 5.4 (f)), a qualitative analysis of the translational motion was performed to relate the different steps taken by the particles to the externally applied magnetic field pulses. For this, the transport experiment used to demonstrate the image processing method in Section 5.2.1 was selected. Figure 5.5 (a) shows a similar image to the one shown in Fig. 5.4 (f). However, here, the trajectories are represented by fragments with different colors. These fragments were obtained by dividing the tracking data into sections of 500 data points, corresponding to the recording frame rate of the experiment videos of 500 fps and the quarter period for the external magnetic field sequence of $T/4 = 1$ s, i.e. each fragment represents 1 s of recording time. Each of these colors signify a different motion event observed throughout the whole transport of the EB-JPs. The starting point of each colored section corresponds to the position of the EB-JP prior to the moment a magnetic field pulse is applied, i.e., the sign of the external field in either z- or

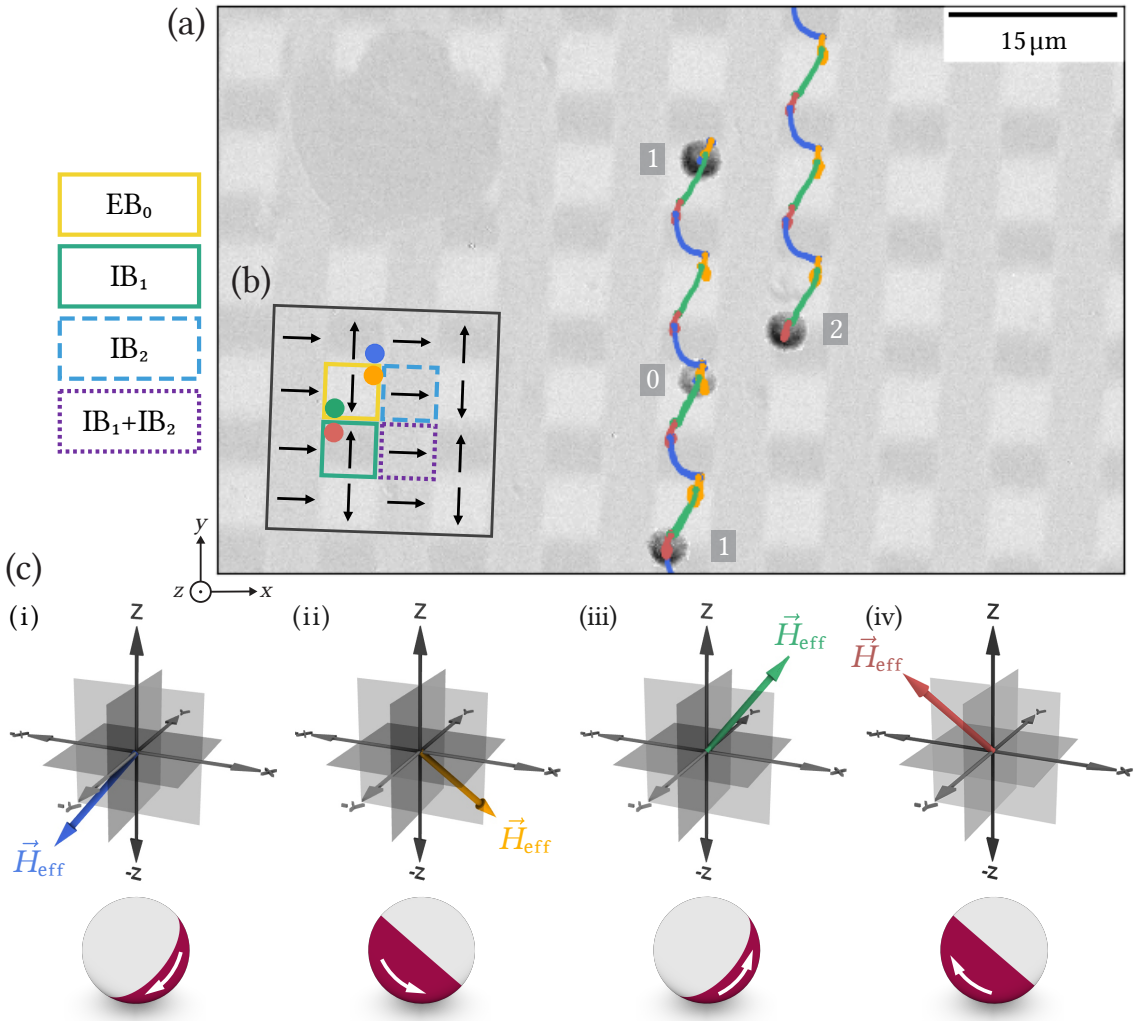

Figure 5.5: Translational motion of EB-JPs above a checkerboard-like domain pattern in relation to externally applied magnetic field pulses. (a) Mapping of identified trajectories for directionally transported EB-JPs in relation to a Kerr microscopy image of the underlying domain pattern. (b) Color-coded domain magnetization direction guide with the stage of the pattern fabrication procedure. (c) Externally applied effective magnetic field vector $\vec{H}_{\mathrm{eff}}$ and the corresponding alignment of an EB-JP. Axis systems (i)-(iv) show the sequence of experimentally applied configurations for $\vec{H}_{\mathrm{eff}}$. Here, the EB-JP is viewed from the same viewing angle as the axis system. Color association is used to relate fragments of the trajectories shown in (a) and preferred location of EB-JP relative to the domains shown in (b), marked with circles, to the $\vec{H}_{\mathrm{eff}}$ configuration.

x-/y-direction is inverted. The last point of the section corresponds to the resting position reached by the EB-JP upon the induced transformation of the particle's potential energy landscape. From this depiction of the trajectories, four resting positions can be recognized in relation to the domain magnetization configuration shown in Fig. 5.5 (b), in particular, to the respective DWs. This magnetization configuration was taken from the Kerr analysis presented in Sec. 5.1.2. Here, the Kerr image used as background for the trajectory map presents a contrast opposite to that of the Kerr image shown in Fig. 5.2 (a), which originates from a different subtraction order of the Kerr images. Therefore, to avoid confusion, the magnetization domain configuration (black arrows) and a legend for the fabrication process stage of a specific domain type are shown. The circles in Fig. 5.5 (b) with colors matching the segments of the trajectories, represent the areas where a particle comes to rest, i.e., where positions of minimal potential energy for the EB-JP can be inferred. Each of these positions corresponds to a specific configuration of the externally applied magnetic field, emphasized in Fig. 5.5 (c). Here, the colors of the effective magnetic field vectors ($\vec{H}_{\text{eff}}$) match the corresponding induced steps in Fig. 5.5 (a) and thus, the positions in relation to the domain configuration reached from that step (cf. Fig. 5.5 (b)). The (i)-(iv) $\vec{H}_{\text{eff}}$ are presented in the order they were applied in the magnetic field pulse sequence and the EB-JPs schematically placed under the corresponding axis system illustrates the alignment of the EB-JP cap to $\vec{H}_{\text{eff}}$. Here, it is assumed that the EB-JP caps have an onion magnetization texture, originating from the sputtered EB system (cf. Section 3.1) that introduces a strong unidirectional anisotropy to result in a pinning of the magnetic moments in the ferromagnetic (FM) layer of the cap [TRH21, HRT21, Huh22, Reg22]. The respective net magnetic moment of the cap is, thus, indicated by the white arrows in Fig. 5.5 (c). Analyzing the supposed areas for the minimal potential energy of the EB-JPs with respect to the domain pattern, it can be observed that they are primarily located next to the hh-/tt-DWs. This is in agreement with theoretical expectations as DWs originating from domains with opposing magnetization direction exhibit stronger stray fields than hs/ts DWs [HZK13], therefore favouring the attraction of magnetic particles.

Analyzing the individual steps together with the corresponding configuration of $\vec{H}_{\text{eff}}$ (cf. Fig. 5.5 (c)), it can be observed that the applied pulses with $\vec{H}_{\text{eff}}$ configurations (i) blue and (iii) green induce large translational steps. This is to be expected as the transport mechanism (cf. Section 2.5.3) establishes that

an inversion of $\vec{H}_{\mathrm{ext,z}}$ induces a motion of the magnetic particle towards a DW with intrinsically inverse stray field in z-direction compared to the previous DW [HKB15, HRT21, Huh22]. Additionally, a sing change in $\vec{H}_{\mathrm{ext}}$ along the x- and y-axes induces a small transport step, where the particle moves to the opposite side of the same DW, as it can be seen for the $\vec{H}_{\mathrm{eff}}$ configurations (ii) orange and (iv) red. The trajectories shown here were obtained using the circular tracker which follows the position of the center of the EB-JPs (cf. Section 3.4). Here, as in Fig. 5.4 (f), four EB-JPs have been included in the trajectory map (cf. Fig. 5.5 (a)) to show the first and last tracked visible location of the EB-JPs within the map area, marked by a number to the left or right side of the particle, respectively. It can be observed that particles show a downwards movement and that the particles 0 and 1 follow the same trajectory as they pass through the same domains.

5.2.3 Angular Motion

The previous analysis decomposed the particle trajectories into the individual translational steps taken over the checkerboard-like domain pattern (cf. Section 5.2.2). Now, the investigation of the EB-JP motion dynamics is deepened by additionally studying tracking data obtained by using a rectangular marker on the particles, where the orientation of the EB-JP cap with respect to the xy-plane is followed. Then, based on the analysis of the translational motion Fig. 5.6 was generated to visualize the EB-JP spatial cap orientation throughout the whole conducted experiment. The trajectories of the EB-JPs are shown as well, however, in addition to the x- and y-location of the center of the particles (gray points), differently colored arrows illustrating the orientation of the EB-JP cap are now included. The size and direction of each arrow was calculated from the vector subtraction of the EB-JPs position obtained with the circular tracker and the position obtained with the rectangular one. Here, following the same methodology as in the translational motion analysis, the arrows are shown in colors that match the configuration of the corresponding $\vec{H}_{\mathrm{eff}}$ (cf. Fig. 5.5 (c)) for the individual steps. Additionally, the arrows within a step show a gradient of color to indicate the direction of the rotation, where the brightest arrow indicates the first orientation of the cap and the darkest one the last orientation. To improve the visual distinction between the arrows, they have been assigned the same length (longer than the longest arrow obtained from the vector subtraction), and only a limited number

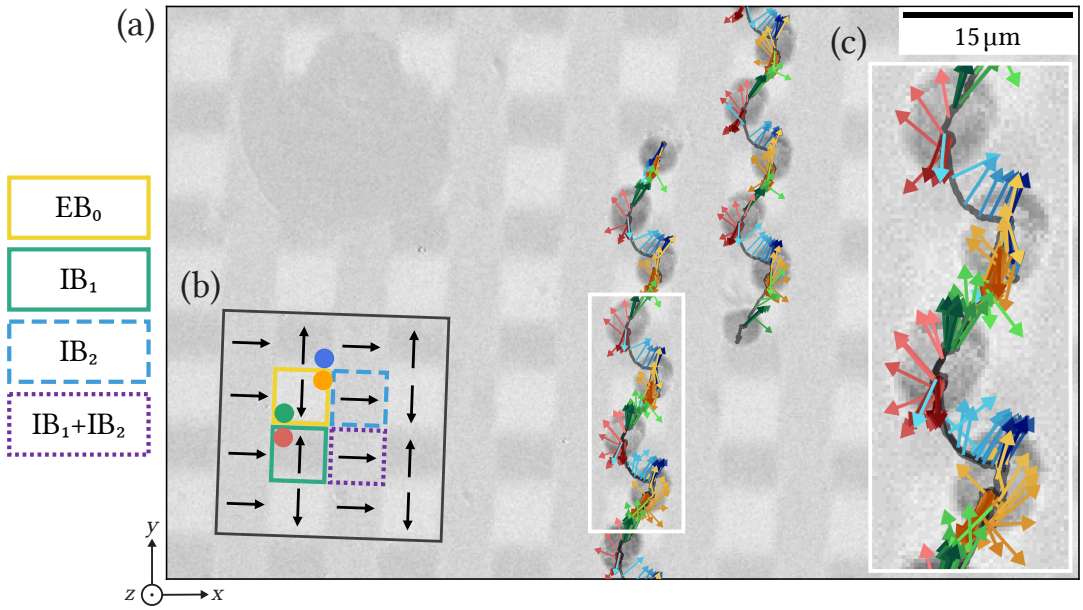

Figure 5.6: Analysis for the rotational motion of EB-JPs above a checkerboard-like domain pattern in relation to externally applied magnetic field pulses. (a) Mapping of identified trajectories for directionally transported EB-JPs in relation to the Kerr microscopy image of the underlying domain pattern. Here, the differently colored arrows indicate the orientation of the EB-JP cap in the xy-plane with respect to the center of the particle. The arrows follow the same color coding as used for distinguishing the $\vec{H}_{\text{eff}}$ configurations of the individual pulses shown in Fig. 5.5 (c) (i)-(iv). (b) Color-coded domain magnetization direction guide with the stage of the pattern fabrication procedure. (c) Zoomed area to improve visual distinction of the time-dependent cap orientations.

of them have been included. For the same reason, an inset showing an enlarged selected area is included (cf. Fig. 5.6 (c)). In contrast to the previously shown EB-JP trajectory maps (Fig. 5.4 (f) and Fig. 5.5 (a)), here, all the resting/reached positions of the EB-JPs after each individual step along their trajectories are shown to improve the association of the arrows with the particles' positions. From this arrow depiction of the trajectories, it can be observed that only for the small steps (red and orange steps) a rotation in the xy-plane of the EB-JP cap can be followed. This is in agreement with previous investigations on the employed prototypical transport mechanism [HRT21, Huh22]. The rotations are easier to follow within the red colored steps, where the JPs always have the same sense of orientation. In the case of the orange colored steps, an angular change of ca. 180° can also be

observed between the first and last arrow of the individual step, but the intermediate phases of the rotation can not be identified unambiguously for most of the steps. This is attributed to difficulties for the tracking software to follow these rotations. Analyzing now the large steps (blue and green), it can be observed that although a change in the orientation of the arrows is visible, this angular change takes place within the first milliseconds and that afterward, the arrows keep their orientation for the same step. This angular reorientation within the first milliseconds of the step has been discovered to correspond to a readjustment of the rectangular tracker upon the initial movement of the particle and not to a traceable particle rotation. Still, a physical reorientation of the EB-JP cap upon inducing a large transport step is recognizable from the particles shown for the initial and final positions in Fig. 5.6 (a) and (c), but a more detailed analysis of the corresponding rotational motion is hindered thus far.

5.2.4 Transition Field Strength

In addition to the EB-JPs trajectory analyses presented in Sections 5.2.1, 5.2.2 and 5.2.3, transport experiments were conducted that had the premise of determining a transition field strength for switching from vertical to diagonal particle trajectories and vice versa. From the initial particle transport experiments carried out to determine the trajectories of the EB-JPs, it became evident that the particles exhibit a preferential vertical trajectory (along the here defined in-plane y-direction). Therefore, the question arose under which experimental conditions the EB-JPs would perform diagonal 2D translational movement, since this behaviour has been previously observed for superparamagnetic particles [Deu16]. Probing different amplitudes for the external magnetic field pulses, it could be deduced that the strength of the external field in x-direction is the critical parameter for provoking a transition in the observed transport trajectories. To this end, EB-JPs transport experiments were performed with a constant amplitude of the externally applied magnetic field pulses along the y- and z-direction of $H_{\mathrm{max},y/z} \cdot \mu_0 = 3$ mT, while the amplitude for the pulses along the x-direction was varied in different transport experiments from $H_{\mathrm{max},x} \cdot \mu_0 = 1$ mT to 4 mT. Figure 5.7 summarized the trajectory maps obtained from these experiments and close-ups of selected areas marked with black rectangles. To improve visualization of the trajectories, no arrows and only particles corresponding to the initial

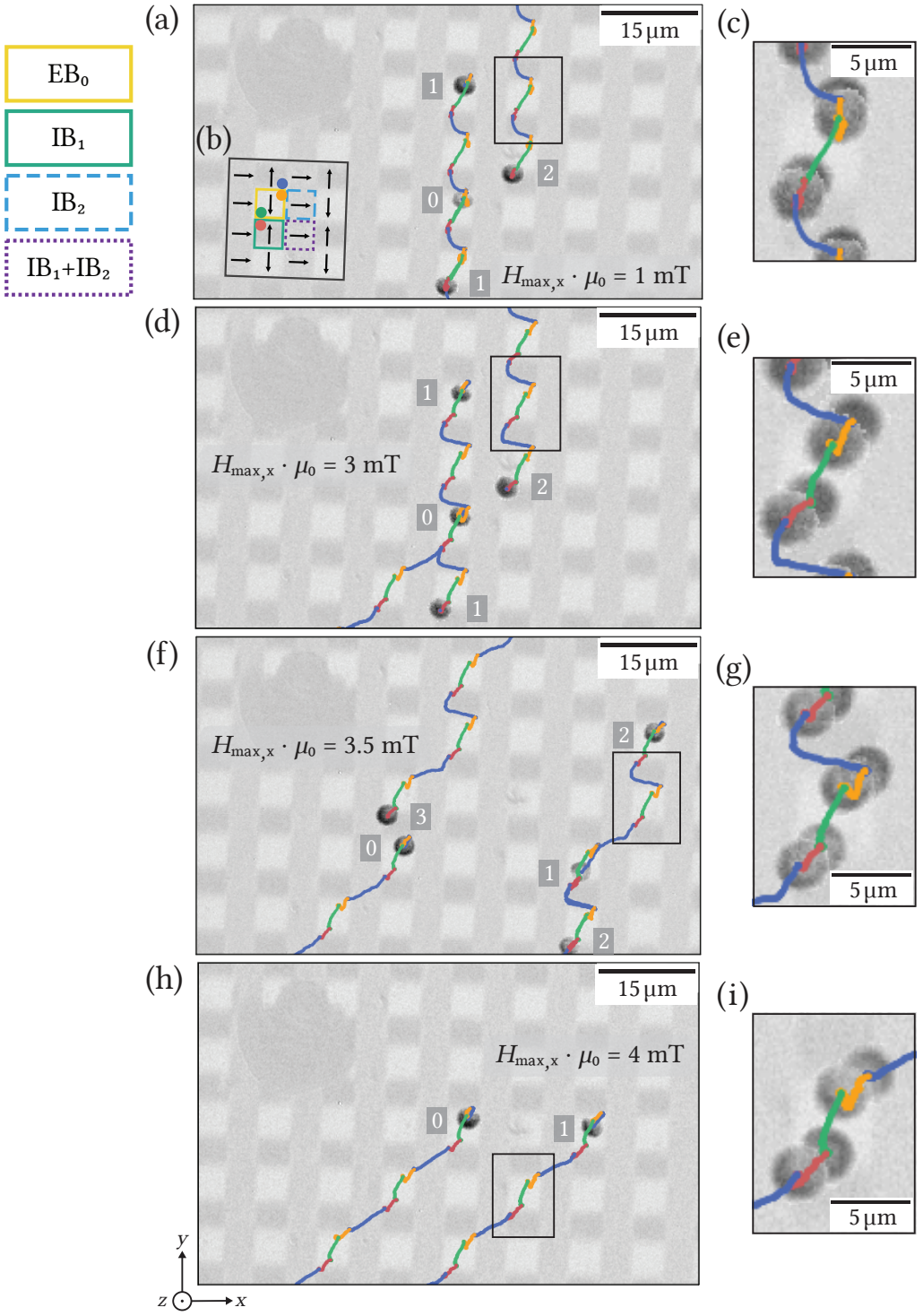

Figure 5.7: Trajectory maps of EB-JPs above a checkerboard-like domain pattern obtained with external magnetic fields pulses along the x-axis of (a) 1 mT, (d) 3 mT, (f) 3.5 mT, and (h) 4 mT amplitude. Here, $H_{\mathrm{max},y/z} \cdot \mu_0 = 3$ mT was kept constant for all experiments. (b) Color-coded domain magnetization direction guide. (c), (e), (g) and (i) Close-ups of the areas indicated on the corresponding maps by the black rectangle. For more information, please consult the text.

and last tracked position are shown in the trajectory maps this time. The numbers to the left of the particles mark the initial tracked position, while the numbers to the right mark the last tracked position. The close-ups, however, show the resting positions reached by the EB-JPs after performing each step. In Fig. 5.7 (a), the map with the vertical trajectories used so far for the different transport analyses is shown. Here, the amplitude of the x-pulses (1 mT) was smaller than for the y- and z- pulses, therefore, no diagonal motion of the EB-JPs was observable. This is supposedly due to $H_{\mathrm{ext,x}}$ not being large enough to push the particles, i.e., their cap, toward the outer boundaries of the hh-/tt-DWs, closer to the hs-/ts-DWs. Thus, when $H_{\mathrm{ext,z}}$ is inverted, the particles prefer to move to the opposite corner of the same domain. However, when the pulses along all three directions are set to have the same amplitude of 3 mT, one of the visible particles in the map (particle 0), exhibits a diagonal trajectory. This is particularly interesting, since the particles shown in Fig. 5.7 (a) and (d) are the same, implying that a 2D pattern combined with a predetermined transition field strength could be used to sort particles with respect to their magnetic characteristics by directing them to different substrate areas. Comparing the close-ups shown in Fig. 5.7 (c) and (e), it can be observed that although both images exhibit sections of a vertical trajectory, the EB-JPs move differently in the individual steps. The trajectories of both small steps (red and orange) in Fig. 5.7 (e) show a more pronounced lateral motion, which is due to the particles aligning to a position closer to the hs/ts DWs (cf. Fig. 5.7 (b)) in the blue and red steps compared to the positions reached by the particles in the orange and green steps. This can also be distinguished by the distance between the resting positions of the particles at the end of the red and green steps, or blue and orange steps, when comparing them with the distances between the particles at the equivalent positions in Fig. 5.7 (c). Additionally, the blue particle trajectories differ slightly but significantly when comparing the results of Fig. 5.7 (c) and (e).

By further increasing $H_{\mathrm{ext,x}}$ to an amplitude of 3.5 mT, EB-JPs exhibit trajectories that combine vertical and diagonal motion events (cf. Fig. 5.7 (f)) until the field is strong enough to stabilize purely diagonal trajectories for all observed EB-JPs (cf. Fig. 5.7 (h)). From the maps showing parts of diagonal trajectories, it can be observed that the blue trajectory fragments, where the particle crosses a domain with horizontal magnetization direction (IB_1+IB_2), is crucial for establishing a diagonal trajectory. This is for H_{ext} configurations used within the applied

magnetic field pulse sequence. However, additional diagonal trajectory directions can be obtained by selecting different relations between the magnetic field pulses applied in all three directions. Inverting the current H_{ext} along the x- and y-axes would lead to trajectories in the opposite direction (from bottom left to upper right corner) to the ones shown here, while inversion of H_{ext} only along the x- or y-axis, would cause particles to move upwards or downwards between the upper left and bottom right corner. Nevertheless, in all these configurations for the external magnetic field pulses, the large steps (either blue or green) would be the ones establishing the diagonal trajectories as the particles would cross over the IB_2 or IB_1+IB_2 domains during these steps. Looking at Fig. 5.7 (g) and (i), the lateral motion of the particles when performing the small steps is also visible, however, it is most noticeable when comparing the particle positions (red and orange) in Fig. 5.7 (c) and (i).

In resume, an experimental and evaluation method has been successfully developed that can be used to obtain distinctive maps for the motion trajectories of transported magnetic particles in direct relation to the underlying magnetic domain pattern; an analysis which was previously not available when studying solely particle transport data retrieved from optical bright-field microscope images. These maps have been used to qualitatively study the motion dynamics of EB-JPs directed over a checkerboard-like domain pattern in relation to the configuration of applied magnetic field pulses. Finally, a transition field strength that modifies the trajectories from being vertical to diagonal, for all EB-JPs investigated here, has been found, which is around $H_{\text{max},x} \cdot \mu_0 = 3.5$ mT in combination with $H_{\text{max},y/z} \cdot \mu_0 = 3$ mT.

6 Summary and Outlook

The work presented in this thesis was focused on two main investigations regarding the directed transport of Exchange-Bias capped Janus particles (EB-JPs) above topographically planar, magnetically patterned substrates. For this purpose, EB-JPs were fabricated via sputter deposition of an Exchange-Bias (EB) layer system on a self-assembled array of nominal 3 µm sized polystyrene particles, thus creating particles with an attached hemispherical EB thin film cap. For the first investigation, the influence of the ferromagnetic layer thickness (t_F) in the cap's EB layer system, varied from 5 nm to 100 nm, on the one-dimensional (1D) translational and rotational motion dynamics of EB-JPs was studied. In a subsequent study, an analysis was carried out to determine the two-dimensional (2D) trajectories of EB-JPs over a checkerboard-like domain pattern in relation to the configuration of the applied magnetic field pulse sequence. The aim of these particle transport studies was, on the one hand, to determine whether the magnetic properties of EB-JPs caps have an influence on the particles' motion behavior as well as mobility and, on the other hand, to develop a systematic method that would reveal 2D trajectories of transported particles in conjunction to an underlying complex domain pattern, in particular of EB-JPs. To this end, two magnetic domain patterns with in-plane magnetization fabricated via ion bombardment induced magnetic patterning (IBMP) were selected: A prototypical parallel stripe domain pattern used for the analysis of 1D particle transport, and a checkerboard-like domain pattern for inducing 2D particle trajectories. The analysis of EB-JPs mobility, in the framework of this project, consisted primarily of recording particle transport motion with a high speed camera and subsequently tracking the time-dependent positions of EB-JPs from individual frames of the recordings. The tracking procedure was systematically performed twice, by using a circular and a rectangular particle marker, respectively, to gather information on the particles' center and cap position as well as the rotational in-plane orientation.

Upon analysis of 1D particle transport experiments presented in Chapter 4, a stripe width asymmetry became evident for the utilized periodic stripe domain pattern. This asymmetry was characterized by means of optical microscopy and exploited to simultaneously study the cap ferromagnetic-thickness-dependent particle mobility above two types of stripes, in this work defined as wide (ca. 6.3 µm) and thin (ca. 3.7 µm) stripes. This width asymmetry, however, imposed the need to develop a sorting strategy of the tracking data obtained from the transport experiments, leading to four step categories, depending on whether a large or small transport step was induced by the externally applied magnetic field sequence: "wide stripe-large step", "thin stripe-large step", "wide stripe-small step", and "thin stripe-small step". According to these step categories, mean steady-state translational and rotational EB-JPs velocities were determined for both stripe types and a selected range of t_F. Steady-state translational velocities were extracted from the time-dependent particle center position data from the large steps, whereas steady-state rotational velocities were extracted from the time-dependent cap angular orientation from a specified range of data from the small steps. From the determined mean steady-state velocities, a tendency for EB-JPs to move/rotate faster when transported above the thin stripe compared to the wide stripe was observed. This is attributed to the stray fields of the thin stripe forming in a more confined area (xy-plane), thus, creating larger potential energy gradients for the particles. Furthermore, from the same results it was observed that EB-JPs have similar ferromagnetic thickness dependency for both translational and rotational steady-state velocities and with respect to the stripe type. From the obtained mobility trend and the qualitative analysis of individual and agglomerate EB-JPs motion with respect to t_F, a hypothesis of a phase diagram correlating the particles motion dynamics with the EB-JP cap's magnetic properties was inferred.

For the second main investigation, presented in Chapter 5, particle transport experiments above a checkerboard-like domain pattern were performed with the primary objective to analyze EB-JPs motion with respect to the position of magnetic domains, respectively domain walls (DWs), in the underlying patterned substrate. Hence, a magnetic domain map for the utilized substrate sample needed to be acquired prior to conducting EB-JP transport experiments. Therefore, the substrate was magnetically characterized by means of Kerr and magnetic force microscopy (MFM). From these analyses, the positions, sizes, and magnetization

directions of domains together with information about the magnetic charge distributions within present DWs were obtained. By establishing a reference point on the substrate and combining the magnetic domain map with the recorded particle transport videos as well as the corresponding tracking data, a systematic method was successfully developed to correlate particle trajectories, i.e., particle transport individual steps, with the underlying magnetic domain pattern. The hereby obtained map of EB-JP trajectories and magnetic domains was used to spatially estimate the positions of local potential energy minima for the EB-JPs within the magnetic field landscape (MFL) formed on top of the substrate in conjunction with the externally applied magnetic field configuration. Based on this, a qualitative understanding of observed particle trajectories in relation to the positions of differently configured DWs within the substrate was achieved. Additionally, a critical magnitude for the externally applied field was determined for inducing a transition between vertical and diagonal (in the xy-plane) trajectories of EB-JPs. From experiments where the amplitude of external magnetic field pulses in the lateral x-direction was varied, a critical transition amplitude of ca. 3.5 mT was found. It was additionally observed however, that not all investigated EB-JPs switch their motion direction at the same external field amplitude. The transition amplitude is rather distributed. This demonstrates the possibility of sorting particles transported above a 2D pattern with respect to their magnetic properties by directing them to different substrate areas.

Growing on the results of this thesis, different follow-up experiments are suggested. Regarding the 1D motion analysis, further insights on the magnetic properties of the EB-JP caps are desired. Therefore, first order reversal curve (FORC) measurements via vibrating sample magnetometry (VSM) could be the first step towards magnetically characterizing the EB-JPs hemispherical caps, as FORC measurements can resolve the magnetic behavior of individual entities within arrays of particles, e.g., remagnetization routes [Reg22]. Additionally, similar experiments on purely ferromagnetic capped JPs could help determine the veracity of the stated hypothesis if the increase in steady-state velocities of the JPs for t_F = 5 nm to 40 nm is linear rather than a peaked curve. On the other hand, magnetic simulations of the checkerboard-like pattern could be performed to calculate the potential energy landscape felt by the particles, in order to establish a connection between the energetically preferred positions and the spatially resolved positions obtained previously. As a side remark, it is strongly suggested to include

a reference point/structure in future design of patterns intended for use in particle transport experiments to facilitate the application of the developed method. The reference structure should preferably be located at the center of the sample area, have sharp edges and no symmetry points to avoid possible confusion when analyzing the sample with different characterization methods.

Appendix

A

A.1 Particle Self-Assembly Parameters

For the self-assembly of the particles, described in Section 3.1, different parameters were varied within the methodology of *Micheletto et al.* [MFO95] (see Table A.1). This parameter study was carried out to find the optimal parameters for the production of samples with a closed packed monolayer of 3 µm nominal diameter polystyrene particles over a large sample area. Large monolayers of closed packed particles facilitate the process of magnetic characterization of the particles [TRH21]. This is because having larger areas without particles considerably decreases the signal ratio of the Exchange-Bias Janus particles with respect to the planar thin film system. However, no set of parameters displayed both an optimal assembly and accurate reproducibility. Nonetheless, the parameters that led to the best self-assemblies are marked in magenta in the table.

Table A.1: Parameters tested for the self-assembly of polystyrene particles with 3 μm nominal diameter on glass substrates.

Particle concentration (c_p) [mg/mL]	1, 1.5, **2** with **0**, 1, 2.5, 5, 10, 15, 25 vol% ethanol
Droplet volume (V_d) [μL]	15, 20, 25, 35, 40, **50**, 70
Heating device temperature (T_{dp}) [°C]	25, **30**, 35
Drying process angle (θ_{dp})	5°, 9°, **15°**
Rotation of samples during drying process	0°, 90°, **180°/90°** every **2**, 5 min

A.2 1D Sample Stripe Size Determination

The width of the stripe domains in the sample used for the 1D transport of EB-JPs was determined from line profiles obtained from the image shown in Fig. A.2 (a). The line profiles were obtained by means of the free software Gwyddion (version 2.58). The width of the stripes was determined by taking the midpoint of the slopes between the valleys and ridges of the line profiles. Finally, the measurements were averaged according to the stripe-type leading to the estimated values of 6.3 µm and 3.7 µm for the wide and thin stripe, respectively.

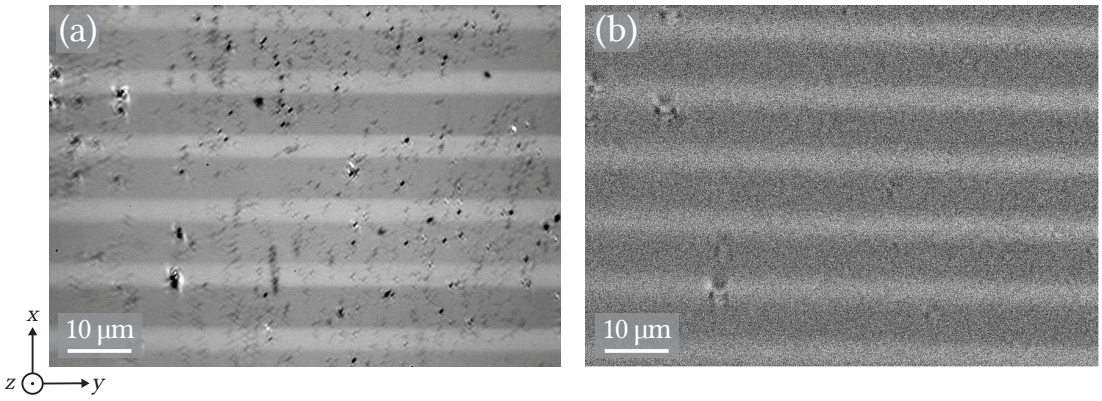

Figure A.1: Images of the magnetically stripe-patterned EB substrate used for the 1D transport experiments of EB-JPs. Both images were acquired via the Kerr microscope described in Section 3.2.2. (a) Microscope image. It is assumed that the stripe pattern is visible due to the residual resist on the sample surface from the lithographic process. (b) Kerr contrast image. Here, the opposing in-plane magnetization directions of the stripes along the x-axis allow for the visualization of the stripe pattern.

A.3 Alternative Approach for the Rotational Step Size Determination

The methodology presented in Section 4.1.3 used to determine the rotational step size consist of manually determining the step size by side to side comparing the translational and rotational steps. This method is time consuming and excludes the possibility of automating the evaluation process. Therefore, an alternative approach is proposed. Here, similarly to Fig. 4.4 (e) and (f), a translational step along with its corresponding rotational step are plotted as shown in Fig. A.2 (a) and (b), respectively. However, in addition, the absolute value of the derivative of the translational step (a) is calculated and its values are smoothed by means of a Savitzky-Golay filter with a window of 9 points and a polynomial of order 1. The resulting derivative is plotted below the steps, as shown in Fig. A.2 (c). Afterwards, the difference dy_i between the maximum value and the minimum value within the first 20% of the derivative (from $t = 0.0$ s to $t = 0.2$ s) is calculated. The value obtained for dy_i is then used to define a threshold to obtain the first initial cutting point of the corrected rotational step, so that the first data point (from $t = 0$ s to $t = 1$ s) in the derivative exceeding a predefined multiple of dy_i is marked with a red circle. The need to have a platou at the beginning of the transport-rotational steps to improve the visualization of the actual start of the rotational step is what led to initially crop the data for these steps as described in Section 4.1.1. The same methodology is followed to determine the final cutting point for the corrected rotational step, using in this case 50% of the derivative (from $t = 1.0$ s to $t = 0.5$ s) to calculate dy_f. The first cutting points obtained from the derivative are also shown in Fig. A.2 (a) and (b) for illustrative purposes. So far, the analysis led to a selected data area for the rotational step marked in yellow and green. However, it is also noted that sometimes, as in this case, when the step is started the tracking program takes a few milliseconds(here the first three data points) to correctly adjust the marker to the EB-JP cap. These data points should be excluded from the analysis, so the cutting points are adjusted as follows. If the line connecting the first initial cutting point (left red circle) to the first final cutting point (right red circle) in the rotational data has a positive slope, the minimum value within the yellow and green area is assigned as the new initial cutting point (left black diamond), and the maximum value as the new final cutting point (right black diamond). If the slope of the connecting line is negative,

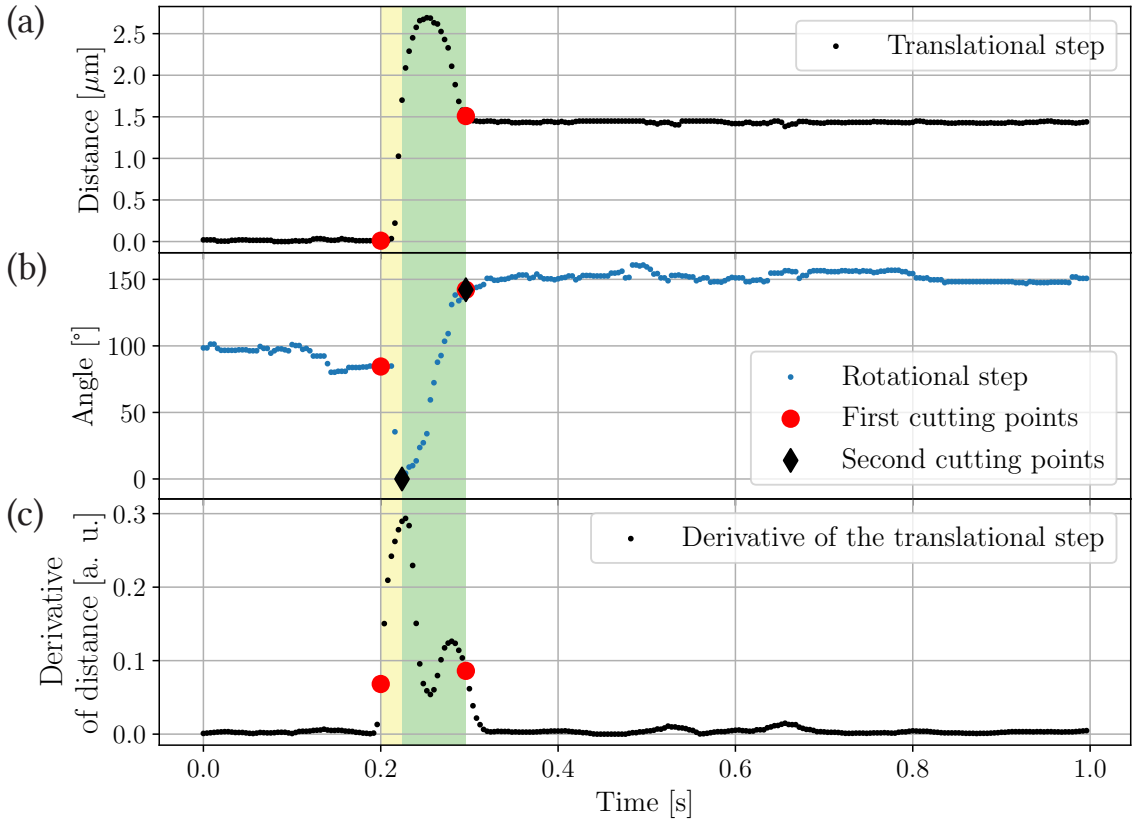

Figure A.2: Rotational step size determination for an example transport step. (a) Translational movement and (b) rotational movement of an EB-JP for the same transport step. (c) Absolute value of the derivative of (a). Big circular-shaped indicators mark the initially determined cutting points for the step size determination (area highlighted in yellow and green). Diamond-shaped indicators mark the final cutting points for the relevant data with its corresponding area marked in green.

the assignment of the cutting points is carried out inversely. Finally, the area of interest is defined from the black diamond on the left to the diamond on the right and highlighted in green.

This methodology, although simplistic, appears to correctly identify the time window of the rotational step. However, it requires less noisy tracking data, which could be obtained by recording the images of the transport experiments with higher resolution and more homogeneous illumination and/or by using other tracking methods. One proposed tracking software would be the Adaptable Particle Tracking software (AdaPT), which provides an intensity-based localization

technique to detect particles [DHK21]. Nonetheless, a more advanced version would be required to cover angular changes in a finer range (tenths of a degree) than what the current version provides (45° changes).

A.4 Scaling Factor Determination

To determine the scaling factor between two images taken with different experimental setups and magnification objectives, here, Kerr microscope and particle transport setup, the following image processing was employed. Each pair of cropped images (transport image and one rotated reduced Kerr image) obtained as explained in Section 5.2.1, which shown the same distinct reference point, were taken for comparison. For that, both images were first passed though a Gaussian filter to reduce image noise, which improves the sharpness of the reference point edges. Afterward, the filtered transport and Kerr images were normalized and passed through two additional filters, a median filter and a Sobel filter. The median filter further reduced the noise in the images and the Sobel filter applied to the x- and y-axes was used to detect the edges of the reference point. After the different filters, the transport and Kerr images were transformed into the images shown in Fig. A.3 (a) and (b), respectively. These edges were used to determine the correct scaling factor and rotation angle to be applied to the Kerr image by means of image subtraction, transport image Fig. A.3 (a) - Kerr image Fig. A.3 (b) (cf. Fig. A.3 (c)). For the subtraction of images, the method for drift correction described in Section 5.1.2 was used. Here, for a pair of transport and Kerr images, the Kerr image was shifted to test different alignments within a predefined shift interval. For each alignment, an error from the subtraction was calculated and assigned to the corresponding combination of alignment, scaling factor and angle. After iterating over different angles, scaling factors and alignments, a combination of settings with the minimum error was obtained and selected for use.

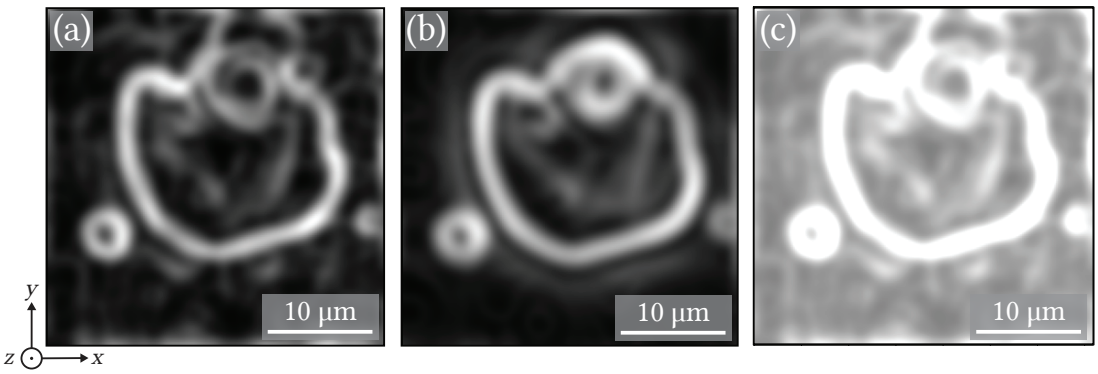

Figure A.3: Edge detection and image subtraction of reference point in 2D transport sample as complementary images for Fig. 5.4. (a) Filtered normalized transport image. (b) Filtered normalized Kerr image. Here, the image with the rotation angle, scaling and alignment leading to the minimum error is shown. (c) Subtracted image, (a)-(b).

Bibliography

[AHG05] Albrecht, M., G. Hu, I. L. Guhr, T. C. Ulbrich, J. Boneberg, P. Leiderer and G. Schatz. *Magnetic multilayers on nanospheres.* Nature Materials, 4(3), 203 (2005).

[APP16] Albisetti, E., D. Petti, M. Pancaldi, M. Madami, S. Tacchi, J. Curtis, W. P. King, A. Papp, G. Csaba, W. Porod, P. Vavassori, E. Riedo and R. Bertacco. *Nanopatterning reconfigurable magnetic landscapes via thermally assisted scanning probe lithography.* Nature Nanotechnology, 11(6), 545 (2016).

[BGK03] Butt, H., K. Graf and M. Kappl. *Physics and Chemistry of Interfaces.* Wiley (2003).

[Bra00] Bradski, G. *The OpenCV Library.* Dr. Dobb's Journal of Software Tools (2000).

[BSB05] Bergmann, L., Schaefer Clemens, S. Blügel and R. Kassing. *Lehrbuch der Experimentalphysik 6: Festkörper.* Walter de Gruyter, Berlin, 2. Auflage (2005).

[CBF98] Chappert, C., H. Bernas, J. Ferré, V. Kottler, J. P. Jamet, Y. Chen, E. Cambril, T. Devolder, F. Rousseaux, V. Mathet and H. Launois. *Planar patterned magnetic media obtained by ion irradiation.* Science, 280(5371), 1919 (1998).

[CBV13] Chen, A., T. Byvank, G. B. Vieira and R. Sooryakumar. *Magnetic microstructures for control of brownian motion and microparticle transport.* IEEE Transactions on Magnetics, 49(1), 300 (2013).

[CFR89] Casagrande, C., P. Fabre, E. Raphaël and M. Veyssié. *"Janus Beads": Realization and Behaviour at Water/Oil Interfaces.* Europhysics Letters, 9(3), 251 (1989).

[CG08] Cullity, B. D. and C. D. Graham. *Introduction to magnetic materials.* Wiley-IEEE Press, 2 Auflage (2008).

[CIS] CISMM at UNC-CH; supported by the NIH NIBIB (NIH 5-P41-RR02170). *Video Spot Tracker.*

[CKA99] Cowburn, R. P., D. K. Koltsov, A. O. Adeyeye, M. E. Welland and D. M. Tricker. *Single-Domain Circular Nanomagnets.* Phys. Rev. Lett., 83, 1042 (1999).

[CLS12] Chin, C. D., V. Linder and S. K. Sia. *Commercialization of microfluidic point-of-care diagnostic devices.* Lab on a Chip, 12(12), 2118 (2012).

[Coe10] Coey, J. M. D. *Magnetism and Magnetic Materials.* Cambridge University Press (2010).

[Deu16] Deumel, S. *Beeinflussung der Transporteigenschaften magnetischer Partikel durch künstliche Domänenstrukturen.* Bachelor thesis, Universität Kassel (2016).

[DHK21] Dingel, K., R. Huhnstock, A. Knie, A. Ehresmann and B. Sick. *AdaPT: Adaptable Particle Tracking for spherical microparticles in lab on chip systems.* Computer Physics Communications, 262, 107859 (2021).

[EES05] Engel, D., A. Ehresmann, J. Schmalhorst, M. Sacher, V. Höink and G. Reiss. *On the origin of ion bombardment induced exchange bias modifications in polycrystalline layers.* Journal of Physics D: Applied Physics, 38(6), 801 (2005)).

[Ehr04] Ehresmann, A. *He-ion bombardment induced exchange bias modifications: Fundamentals and applications.* Recent. Res. Devel. Applied Phys., 7, 401 (2004).

[EJE05] Ehresmann, A., D. Junk, D. Engel, A. Paetzold and K. Röll. *On the origin of ion bombardment induced exchange bias modifications in polycrystalline layers.* Journal of Physics D: Applied Physics, 38(6), 801 (2005).

[EKH15] Ehresmann, A., I. Koch and D. Holzinger. *Manipulation of superparamagnetic beads on patterned exchange-bias layer systems for biosensing applications* (2015).

[EKK04] Ehresmann, A., I. Krug, A. Kronenberger, A. Ehlers and D. Engel. *In-plane magnetic pattern separation in NiFe/NiO and Co/NiO exchange biased bilayers investigated by magnetic force microscopy.* Journal of Magnetism and Magnetic Materials, 280(2-3), 369 (2004).

[ELW11] Ehresmann, A., D. Lengemann, T. Weis, A. Albrecht, J. Langfahl-Klabes, F. Göllner and D. Engel. *Asymmetric magnetization reversal of stripe-patterned exchange bias layer systems for controlled magnetic particle transport.* Advanced Materials, 23(46), 5568 (2011).

[Get08] Getzlaff, M. *Fundamentals of Magnetism.* Springer, Berlin, Heidelberg, 1. Auflage (2008).

[GEU18] Gaul, A., D. Emmrich, T. Ueltzhöffer, H. Huckfeldt, H. Doğanay, J. Hackl, M. I. Khan, D. M. Gottlob, G. Hartmann, A. Beyer, D. Holzinger, S. Nemšák, C. M. Schneider, A. Gölzhäuser, G. Reiss and A. Ehresmann. *Size limits of magnetic-domain engineering in continuous in-plane exchange-bias prototype films.* Beilstein Journal of Nanotechnology, 9(1), 2968 (2018).

[GHH16] Gaul, A., S. Hankemeier, D. Holzinger, N. D. Müglich, P. Staeck, R. Frömter, H. P. Oepen and A. Ehresmann. *Engineered magnetic domain textures in exchange bias bilayer systems.* Journal of Applied Physics, 120(3), 033902 (2016).

[Gij04] Gijs, M. A. M. *Magnetic bead handling on-chip: New opportunities for analytical applications.* Microfluidics and Nanofluidics, 1(1), 22 (2004).

[Gö19] Gördes, J. *Two dimensional transport of superparamagnetic particles in periodic artificial magnetic stray field landscapes.* Master thesis, Universität Kassel (2019).

[Ham37] Hamaker, H. *The London—van der Waals attraction between spherical particles.* Physica, 4(10), 1058 (1937).

[HANL15] Hu, X., R. Abedini-Nassab, B. Lim, Y. Yang, M. Howdyshell, R. Sooryakumar, B. B. Yellen and C. G. Kim. *Dynamic trajectory analysis of superparamagnetic beads driven by on-chip micromagnets.* Journal of Applied Physics, 118(20), 203904 (2015).

[HKB15] Holzinger, D., I. Koch, S. Burgard and A. Ehresmann. *Directed Magnetic Particle Transport above Artificial Magnetic Domains Due to Dynamic Magnetic Potential Energy Landscape Transformation.* ACS Nano, 9(7), 7323 (2015).

[Hol15] Holzinger, D. *Transport magnetischer Partikel durch maßgeschneiderte magnetische Feldlandschaften zur Anwendung in mikrofluidischen Mischprozessen.* PhD thesis, Universität Kassel (2015).

[HRS22] Huhnstock, R., M. Reginka, C. Sonntag, M. Merkel, K. Dingel, B. Sick, M. Vogel and A. Ehresmann. *Three-dimensional close-to-substrate trajectories of magnetic microparticles in dynamically changing magnetic field landscapes.* Scientific Reports, 12 (2022).

[HRT21] Huhnstock, R., M. Reginka, A. Tomita, M. Merkel, K. Dingel, D. Holzinger, B. Sick, M. Vogel and A. Ehresmann. *Translatory and rotatory motion of exchange-bias capped Janus particles controlled by dynamic magnetic field landscapes.* Scientific Reports, 11(1), 21794 (2021).

[HS98] Hubert, A. and R. Schäfer. *Magnetic domains: The analysis of magnetic microstructures.* Springer, Berlin (1998).

[Huh22] Huhnstock, R. *Analysis of near-substrate magnetic particle transport for Lab-on-a-chip applications: stray field modulations, influence of particle properties and three-dimensional trajectories.* PhD thesis, Universität Kassel (2022).

[HWB05] Haken, H., H. C. Wolf and W. D. Brewer. *The Physics of Atoms and Quanta.* Springer Berlin Heidelberg, Berlin, Heidelberg (2005).

[HZK13] Holzinger, D., N. Zingsem, I. Koch, A. Gaul, M. Fohler, C. Schmidt and A. Ehresmann. *Tailored domain wall charges by individually set in-plane magnetic domains for magnetic field landscape design.* Journal of Applied Physics, 114(1), 013908 (2013).

[Isr11] Israelachvili, J. N. *Intermolecular and surface forces.* Academic Press, Burlington, 3. Auflage (2011).

[KBS20] Klingbeil, F., F. Block, U. Sajjad, R. B. Holländer, S. Deshpande and J. McCord. *Evaluating and forecasting movement patterns of magnetically driven microbeads in complex geometries.* Scientific Reports, 10(1), 1 (2020).

[KCJ04] Kim, S. W., S. D. Choi, D. H. Jin, K. A. Lee, S. S. Lee and D. G. Hwang. *Local magnetization reversal in exchange biased film by laser annealing.* Journal of Magnetism and Magnetic Materials, 272-276(I), 376 (2004).

[Ker77] Kerr, J. *XLIII. On rotation of the plane of polarization by reflection from the pole of a magnet.* The London, Edinburgh, and Dublin Philosophical Magazine and Journal of Science, 3(19), 321 (1877).

[Kni02] Knight, J. *Honey, I shrunk the lab.* Nature, 418(6897), 474 (2002).

[Kus11] Kuschel, T. *Magnetic anisotropy of transition metal based thin films investigated by magnetooptic Kerr effect.* PhD thesis, Universität Osnabrück (2011).

[LCFK19] Long, T. W., U. M. Córdova-Figueroa and I. Kretzschmar. *Measuring, Modeling, and Predicting the Magnetic Assembly Rate of 2D-Staggered Janus Particle Chai.* Langmuir, 35(5), 8121 (2019).

[LMS17] Lin, G., D. Makarov and O. G. Schmidt. *Magnetic sensing platform technologies for biomedical applications.* Lab Chip, 17(11), 1884 (2017).

[LTK17] Lim, B., S. R. Torati, K. W. Kim, X. Hu, V. Reddy and C. Kim. *Concentric manipulation and monitoring of protein-loaded superparamagnetic cargo using magnetophoretic spider web.* NPG Asia Materials, 9(3), e369 (2017).

[MB56] Meiklejohn, W. H. and C. P. Bean. *New magnetic anisotropy* (1956).

[MB57] Meiklejohn, W. H. and C. P. Bean. *New magnetic anisotropy.* Physical Review, 105(3), 904 (1957).

[Mei62] Meiklejohn, W. H. *Exchange Anisotropy—A Review.* Journal of Applied Physics, 33(3), 1328 (1962).

[Mer18] Merkel, M. A. *Einfluss von Depositions- und Feldkühlparametern auf durch Kathodenzerstäunung hergestellte polykristalline Exchange-Bias-Dünnschichtsysteme.* Master thesis, Universität Kassel (2018).

[Mer22] Merkel, M. A. *Validation of a generalized model for the description of polycrystalline exchange-biased magnetic thin films.* PhD thesis, Universität Kassel (2022).

[MFO95] Micheletto, R., H. Fukuda and M. Ohtsu. *A Simple Method for the Production of a Two-Dimensional, Ordered Array of Small Latex Particles.* Langmuir, 11(9), 3333 (1995).

[MGW90] Manz, A., N. Graber and H. M. Widmer. *Miniaturized total chemical analysis systems: A novel concept for chemical sensing.* Sensors and Actuators: B. Chemical, 1(1-6), 244 (1990).

[MHR20] Merkel, M., R. Huhnstock, M. Reginka, D. Holzinger, M. Vogel, A. Ehresmann, J. Zehner and K. Leistner. *Interrelation between polycrystalline structure and time-dependent magnetic anisotropies in exchange-biased bilayers.* Physical Review B, 102(14), 144421 (2020).

[MLF00] Mewes, T., R. Lopusnik, J. Fassbender, B. Hillebrands, M. Jung, D. Engel, A. Ehresmann and H. Schmoranzer. *Suppression of exchange bias by ion irradiation.* Applied Physics Letters, 76(8), 1057 (2000).

[MMJ01] Mougin, A., T. Mewes, M. Jung, D. Engel, A. Ehresmann, H. Schmoranzer, J. Fassbender and B. Hillebrands. *Local manipulation and reversal of the exchange bias field by ion irradiation in FeNi/FeMn double layers.* Physical Review B - Condensed Matter and Materials Physics, 63(6), 060409 (2001).

[MVP19] Moerland, C. P., L. J. Van IJzendoorn and M. W. Prins. *Rotating magnetic particles for lab-on-chip applications-a comprehensive review.* 19(6), 919 (2019).

[NS99] Nogués, J. and I. K. Schuller. *Exchange bias.* Journal of Magnetism and Magnetic Materials, 192(2), 203 (1999).

[Pae02] Paetzold, A. *Thermische Stabilität und Modifizierung der magnetischen Austauschanisotropie in Schichtsystemen.* PhD thesis, Universität Kassel (2002).

[Pam06] Pamme, N. *Magnetism and microfluidics.* Lab on a Chip, 6(1), 24 (2006).

[PCJ03] Pankhurst, Q. A., J. Connolly, S. K. Jones and J. Dobson. *Applications of magnetic nanoparticles in biomedicine.* Journal of Physics D: Applied Physics, 36(13), R167 (2003).

[Reg18] Reginka, M. *Physical Characterization and Motion Dynamics of Exchange-Biased Janus Particles.* Master thesis, Universität Kassel (2018).

[Reg22] Reginka, M. *Magnetic Textures and Magnetization Reversal Processes in Arrays of Ferromagnetic and Exchange-Biased Hollow Hemispheres.* PhD thesis, Universität Kassel (2022).

[RHE21] Reginka, M., H. Hoang, Ö. Efendi, M. Merkel, R. Huhnstock, D. Holzinger, K. Dingel, B. Sick, D. Bertinetti, F. W. Herberg and A. Ehresmann. *Transport Efficiency of Biofunctionalized Magnetic Particles Tailored by Surfactant Concentration.* Langmuir, 37(28), 8498 (2021).

[RLG21] Rampini, S., P. Li, D. Gandhi, M. Mutas, Y. F. Ran, M. Carr and G. U. Lee. *Design of micromagnetic arrays for on-chip separation of superparamagnetic bead aggregates and detection of a model protein and double-stranded DNA analytes.* Scientific Reports, 11(1), 5302 (2021).

[RMG90] Rugar, D., H. J. Mamin, P. Guethner, S. E. Lambert, J. E. Stern, I. McFadyen and T. Yogi. *Magnetic force microscopy: General principles and application to longitudinal recording media.* Journal of Applied Physics, 68(3), 1169 (1990).

[RRS12] Ren, B., A. Ruditskiy, J. H. K. Song and I. Kretzschmar. *Assembly Behavior of Iron Oxide-Capped Janus Particles in a Magnetic Field.* Langmuir, 28(2), 1149 (2012).

[SAKS09] Salazar-Alvarez, G., J. J. Kavich, J. Sort, A. Mugarza, S. Stepanow, A. Potenza, H. Marchetto, S. S. Dhesi, V. Baltz, B. Dieny, A. Weber, L. J. Heyderman, J. Nogués and P. Gambardella. *Direct evidence of imprinted vortex states in the antiferromagnet of exchange biased microdisks.* Applied Physics Letters, 95(1), 012510 (2009).

[Ses12] Seshan, K. *Handbook of thin film deposition: Techniques, processes, and technologies.* Elsevier, Amsterdam, 3. Auflage (2012).

[SFK16] Streubel, R., P. Fischer, F. Kronast, V. P. Kravchuk, D. D. Sheka, Y. Gaididei, O. G. Schmidt and D. Makarov. *Magnetism in curved geometries.* Journal of Physics D: Applied Physics, 49(36), 363001 (2016).

[SGM09] Smoukov, S. K., S. Gangwal, M. Marquez and O. D. Velev. *Reconfigurable responsive structures assembled from magnetic Janus particles.* Soft Matter, 5, 1285 (2009).

[SKR16] Streubel, R., F. Kronast, C. F. Reiche, T. Müuhl, A. U. Wolter, O. G. Schmidt and D. Makarov. *Vortex circulation and polarity patterns in closely packed cap arrays.* Applied Physics Letter, 108(4), 363001 (2016).

[SKS12] Streubel, R., V. P. Kravchuk, D. D. Sheka, D. Makarov, F. Kronast, O. G. Schmidt and Y. Gaididei. *Equilibrium magnetic states in individual hemispherical permalloy caps.* Applied Physics Letters, 101(13), 132419 (2012).

[SMK12] Streubel, R., D. Makarov, F. Kronast, V. Kravchuk, M. Albrecht and O. G. Schmidt. *Magnetic vortices on closely packed spherically curved surfaces.* Phys. Rev. B, 101(17), 174429 (2012).

[Ste12] Stefanita, C.-G. *Magnetism.* Springer Berlin Heidelberg, Berlin, Heidelberg (2012).

[TKW13] Tu, L., T. Klein, W. Wang, Y. Feng, Y. Wang and J. P. Wang. *Measurement of brownian and Néel relaxation of magnetic nanoparticles by a*

mixing-frequency method. IEEE Transactions on Magnetics, 49(1), 227 (2013).

[TL12] Tipler, P. and R. Llewellyn. *Modern Physics.* W. H. Freeman and Company, New York, 6. Auflage (2012).

[TRH21] Tomita, A., M. Reginka, R. Huhnstock, M. Merkel, D. Holzinger and A. Ehresmann. *Magnetic textures in hemispherical thin film caps with in-plane exchange bias.* Journal of Applied Physics, 129(1), 015305 (2021).

[TSJ09] Tierno, P., F. Sagués, T. H. Johansen and T. M. Fischer. *Colloidal transport on magnetic garnet films.* Physical Chemistry Chemical Physics, 11(42), 9615 (2009).

[UHE18] Urbaniak, M., D. Holzinger, A. Ehresmann and F. Stobiecki. *Magnetophoretic lensing by concentric topographic cylinders of perpendicular magnetic anisotropy multilayers.* Biomicrofluidics, 12, 044117 (2018).

[USK16] Ueltzhöffer, T., R. Streubel, I. Koch, D. Holzinger, D. Makarov, O. G. Schmidt and A. Ehresmann. *Magnetically Patterned Rolled-Up Exchange Bias Tubes: A Paternoster for Superparamagnetic Beads.* ACS Nano, 10, 8491 (2016).

[VGO20] Virtanen, P., R. Gommers, T. E. Oliphant, M. Haberland, T. Reddy, D. Cournapeau, E. Burovski, P. Peterson, W. Weckesser, J. Bright, S. J. van der Walt, M. Brett, J. Wilson, K. J. Millman, N. Mayorov, A. R. J. Nelson, E. Jones, R. Kern, E. Larson, C. J. Carey, İ. Polat, Y. Feng, E. W. Moore, J. VanderPlas, D. Laxalde, J. Perktold, R. Cimrman, I. Henriksen, E. A. Quintero, C. R. Harris, A. M. Archibald, A. H. Ribeiro, F. Pedregosa, P. van Mulbregt and SciPy 1.0 Contributors. *SciPy 1.0: Fundamental Algorithms for Scientific Computing in Python.* Nature Methods, 17, 261 (2020).

[WGP16] Wren, T., B. Gribkov, V. Petrashov and O. Kazakova. *Phase diagram of magnetic states in nickel submicron disks.* Journal of Applied Physics, 119, 179901 (2016).

[WRP19] Wurft, T., W. Raberg, K. Prügl, A. Satz, G. Reiss and H. Brückl. *Evolution of magnetic vortex formation in micron-sized disks.* Applied Physics Letters, 115(13), 132407 (2019).

[WSFX05] Wirix-Speetjens, R., W. Fyen, K. Xu, J. De Boeck and G. Borghs. *A force study of on-chip magnetic particle transport based on tapered conductors.* IEEE Transactions on Magnetics, 41(10), 4128 (2005).

[YAL13] Yetisen, A. K., M. S. Akram and C. R. Lowe. *Paper-based microfluidic point-of-care diagnostic devices.* Lab on a Chip, 13(12), 2210 (2013).

[YBB12] Yan, J., M. Bloom, S. C. Bae, E. Luijten and S. Granick. *Linking synchronization to self-assembly using magnetic Janus colloids.* Nature, 491, 578 (2012).

[YBG15] Yan, J., S. C. Bae and S. Granick. *Colloidal Superstructures Programmed into Magnetic Janus Particles.* Advanced Materials, 27(5), 874 (2015).

[YES07] Yellen, B. B., R. M. Erb, H. S. Son, R. Hewlin, H. Shang and G. U. Lee. *Traveling wave magnetophoresis for high resolution chip based separations.* Lab on a Chip, 7(12), 1681 (2007).

Acknowledgments

Finally, I would like to express my gratitude to everyone who supported me during the course of my master and contributed in one or the other way to the completion of this thesis.

First of all, I would like to express my gratitude to Prof. Dr. Arno Ehresmann for welcoming me into his working group, particularly, when I was not yet part of the university, and for giving me the opportunity to work on this project.

Secondly, I would like to thank Prof. Dr. Giesen taking on the role of second examiner of this work, and for always being a kind teacher.

A very heartfelt gratitude goes to my supervisors Dr. Rico Huhnstock and Dr. Meike Reginka and to Dr. Maximilian Merkel for all their guidance, patience and foremost support during the realization of this project, but above all for the treasured friendship that arose from this experience, without you this project would not have been possible.

Moreover, I would like to express my deepest gratitude to my beloved boyfriend Tobias Müller for his tireless support and motivation during this challenging time, without you I wouldn't be here.

In addition, I thank my family and friends for all their love and support, despite the thousands of kilometers that separate us, you are always with me.

A special mention goes to my dear friends Susy, Christina, Iris and Mory, and to my sister Ariadna for all your help. I will always be grateful.

Last but not least, I also thank all my colleagues of the AGE who were always welcoming, friendly and supportive, with a special mention to Catmarna, Caro, Dana, Hai and Nils.

Statement of Authorship

I hereby declare that this submitted master thesis is my own work. All supporting material and sources used are acknowledged as references. I assure that passages which were literally or analogously taken from published documents are marked with the corresponding citation within the text.

Kassel, 21st February 2023 _____

Claudia Itzel Jauregui Caballero